Linking global mantle dynamics with lithosphere dynamics using the geoid, plate velocities and lithosphere stress state as constraints

Dissertation
zur Erlangung des akademischen Grades
"doctor rerum naturalium"
(Dr. rer. nat.)
in der Wissenschaftsdisziplin Geophysik

eingereicht an der
Mathematisch-Naturwissenschaftlichen Fakultät
der Universität Potsdam

von
MSc. Ing. Anthony Osei Tutu

Am 13. November 2017

- Erstbetreuer:.....Prof. Dr. Michael Weber
- Zweitbetreuer:.....Dr. Bernhard Steinberger
- Mentoren::.....Dr. Irina Rogozhina
  Prof. Dr. Volker John
- Gutachter:.....Prof. Dr. Marta P. Gussinye
  Prof. Dr. Clinton P. Conrad

Published online at the
Institutional Repository of the University of Potsdam:
URN urn:nbn:de:kobv:517-opus4-407057
http://nbn-resolving.de/urn:nbn:de:kobv:517-opus4-407057

Declaration of Authorship

I, Anthony Osei Tutu , declare that this thesis titled, "Linking global mantle dynamics with lithosphere dynamics using the geoid, plate velocities and lithosphere stress state as constraints" and the work presented in it are my own. I confirm that:

- This work was done wholly or mainly while in candidature for a research degree at this University.
- Where any part of this thesis has previously been submitted for a degree or any other qualification at this University or any other institution, this has been clearly stated.
- Where I have consulted the published work of others, this is always clearly attributed.
- Where I have quoted from the work of others, the source is always given. With the exception of such quotations, this thesis is entirely my own work.
- I have acknowledged all main sources of help.
- Where the thesis is based on work done by myself jointly with others, I have made clear exactly what was done by others and what I have contributed myself.

Signed: MSc. Ing. Anthony Osei Tutu

Date: 21. 06. 2017

"We are part of this universe; we are in this universe, but perhaps more important than both of those facts, is that the universe is in us."

Neil deGrasse Tyson

Zusammenfassung

Lithosphärenplatten bewegen sich über die niederviskose Asthenosphäre, wobei mehrere Kräfte im Gleichgewicht stehen. Die antreibenden Kräfte umfassen eine basale Schubspannung, die durch Mantelkonvektion verursacht wird, und Plattengrenzkräfte, wie z.B. slab pull und ridge push, während die widerstehenden Kräfte die Reibung zwischen Platten, Widerstand an Tiefseegräben sowie an den kratonischen Wurzeln umfassen. Diese Kräfte erzeugen Plattenbewegungen, das lithosphärische Spannungsfeld und die dynamische Topographie, die mit verschiedenen geophysikalischen Methoden beobachtet werden. Die Orientierung und das tektonische Regime des beobachteten Krusten- und lithosphärischen Spannungsfeldes tragen weiter zu unserem Wissen über unterschiedliche Deformationsprozesse in der Erdkruste und Lithosphäre bei. Mit Hilfe von numerischen Modellen konnten frühere Studien die wichtigsten Kräfte identifizieren, die Spannungen in der Kruste und in der Lithosphäre erzeugen, und die auch zur Bildung von Topographie sowie zum Antrieb der lithosphärischen Platten beitragen. Sie zeigten, dass das Spannungsmuster erster Ordnung, das etwa 80 % des Spannungsfeldes erklärt, aus einem Gleichgewicht der Kräfte stammt, die an der Basis der sich bewegenden lithosphärischen Platten aufgrund der konvektiven Strömung in dem darunter liegenden Mantel wirken. Das verbleibende Spannungsmuster der zweiten Ordnung ist auf laterale Dichtevariationen in der Kruste und der Lithosphäre in Regionen mit ausgeprägter Topographie und hohem Gravitationspotential zurückzuführen, wie im Himalaya und an den Mittelozeanischen Rücken. Durch die Verknüpfung der globalen Lithosphären-Dynamik mit den tiefen Mantelströmungen versucht diese Studie, den Einfluss von flachen und tiefen Dichte-Heterogenitäten auf die Plattenbewegungen, das lithosphärische Spannungsfeld und die dynamische Topographie mit dem Geoid als einer wesentlichen Randbedingung für die Mantel-Rheologie zu untersuchen. Ich verwende das globale 3D-Lithosphären-Asthenosphären-Modell SLIM3D mit viskoelasto-plastischer Rheologie, gekoppelt in 300 km Tiefe an ein spektrales Modell der Mantelströmung. Die Komplexität der Lithosphären-Asthenosphären-Komponente ermöglicht die Simulation der Power-law-Rheologie mit Kriechparametern, die sowohl Diffusions-als auch Dislokationskriechen in den obersten 300 km einschließen.

Zuerst untersuche ich den Einfluss der Intra-Platten-Reibung und der asthenosphärischen Viskosität auf heutige Plattenbewegungen. Bisherige Modellierungsstudien haben vorgeschlagen, dass kleine Reibungskoeffizienten ($\mu < 0{,}1$,

Fließspannung ~ 100 MPa) zu Plattentektonik in Modellen der Mantelkonvektion führen können. Hier zeigen wir, dass der Reibungsparameter, um den heutigen Plattenbewegungen und der Netto-Rotation zu entsprechen, kleiner als 0,05 sein muss. Wir können eine gute Übereinstimmung mit der Größe und Orientierung der beobachteten Plattengeschwindigkeiten (NUVEL-1A) in einem No-Net-Rotation- (NNR) Bezug system mit μ < 0,04 und minimaler Asthenosphärenviskosität ~ $5{\cdot}10^{19}$ Pas bis 10^{20} Pas erreichen. Unsere Schätzungen der Netto-Rotation (NR) der Lithosphäre deuten darauf hin, dass Amplituden $\sim 0.1 - 0.2$ (°/Ma), ähnlich den meisten Beobachtungs-basierten Schätzungen, mit Asthenosphären-Viskositäts-Cutoff-Werten von ~ 10^{19} Pas bis $5 \cdot 10^{19}$ Pas und Reibungskoeffizient μ < 0,05 erreicht werden können.

Der zweite Teil der Studie untersucht weitere Einschränkungen auf flache und tiefe Mantelheterogenitäten, welche Plattenbewegungen verursachen, durch die Vorhersage des Lithosphärenspannungsfeldes und der Topographie und deren Validierung mit Beobachtungen. Lithosphärenspannungen und dynamische Topographie werden mit dem Modellaufbau und den rheologischen Parametern für vorgeschriebene Plattenbewegungen berechnet. Wir validieren unsere Ergebnisse mit der Weltspannungskarte 2016 (WSM2016) und der beobachteten Residualtopographie. Hier haben wir eine Anzahl von thermischen Dichte-Strukturen für den oberen Mantel getestet. Diejenige, die verwendet wurde, um Plattenbewegungen zu berechnen, wird als Referenz- thermische Dichte-Struktur betrachtet. Dieses Modell ist abgeleitet aus einem Wärmestrommodell, kombiniert mit einem Ozeanbodenalter-Modell. Darüber hinaus haben wir drei verschiedene thermische Dichtestrukturen abgeleitet aus globalen S-Wellengeschwindigkeits modellen verwendet, um den Einfluss von Heterogenitäten der lateralen Dichte in den oberen 300 km auf Modellvorhersagen zu zeigen. Ein großer Teil der gesamten dynamischen Kraft, die Spannungen in der Kruste / Lithosphäre erzeugt, hat ihren Ursprung im tiefen Mantel, während die Topographie weitgehend durch flache Heterogenitäten beeinflusst wird. Zum Beispiel gibt es kaum einen Unterschied zwischen den Spannungsorientierungsmustern, die mit und ohne Berücksichtigung der Heterogenitäten in der Dichtestruktur des oberen Mantels in Nordamerika, Australien und Nordafrika vorhergesagt wurden. Allerdings dominiert die Kruste in Gebieten von großer Höhe für die Spannungorientierung im Vergleich zu allen tiefen Mantelbeiträgen.

Diese Studieerforschen die Empfindlichkeit aller betrachteten Oberflächen-Observablen in Bezug auf Modellparameter und gibt Einblicke über den Einfluss der Asthenosphäre und Plattengrenzen-Rheologie auf Plattenbewegung, wobei wir verschiedene thermische Dichte Strukturen zur Vorhersage von Spannungen

und Topographie testen.

Abstract

Lithospheric plates move over the low viscosity asthenosphere balancing several forces. The driving forces include basal shear stress exerted by mantle convection and plate boundary forces such as slab pull and ridge push, whereas the resisting forces include inter-plate friction, trench resistance, and cratonic root resistance. These generate plate motions, the lithospheric stress field and dynamic topography which are observed with different geophysical methods. The orientation and tectonic regime of the observed crustal/lithospheric stress field further contribute to our knowledge of different deformation processes occurring within the Earth's crust and lithosphere. Using numerical models previous studies were able to identify major forces generating stresses in the crust and lithosphere which also contribute to the formation of topography as well as driving lithospheric plates. They showed that the first-order stress pattern explaining about 80 % of the stress field originates from a balance of forces acting at the base of the moving lithospheric plates due to convective flow in the underlying mantle. The remaining second-order stress pattern is due to lateral density variations in the crust and lithosphere in regions of pronounced topography and high gravitational potential, such as the Himalayas and mid-ocean ridges. By linking global lithosphere dynamics to deep mantle flow this study seeks to evaluate the influence of shallow and deep density heterogenities on plate motions, lithospheric stress field and dynamic topography using the geoid as a major constraint for mantle rheology. I used the global 3D lithosphere-asthenosphere model SLIM3D with visco-elasto-plastic rheology coupled at 300 km depth to a spectral model of mantle flow. The complexity of the lithosphere-asthenosphere component allows for the simulation of power-law rheology with creep parameters accounting for both diffusion and dislocation creep within the uppermost 300 km.

First I investigate the influence of intra-plate friction and asthenospheric viscosity on present-day plate motions. Previous modeling studies have suggested that small friction coefficients ($\mu < 0.1$, yield stress ~ 100 MPa) can lead to plate tectonics in models of mantle convection. Here I show that, in order to match present-day plate motions and net rotation, the frictional parameter must be less than 0.05. I am able to obtain a good fit with the magnitude and orientation of observed plate velocities (NUVEL-1A) in a no-net-rotation (NNR) reference frame with $\mu < 0.04$ and minimum asthenosphere viscosity $\sim 5{\cdot}10^{19}$ Pas to 10^{20} Pas. My estimates of net rotation (NR) of the lithosphere suggest that amplitudes $\sim 0.1 - 0.2$ (°/Ma), similar to most observation-based estimates, can be obtained

with asthenosphere viscosity cutoff values of ~ 10^{19} Pas to $5 \cdot 10^{19}$ Pas and friction coefficient $\mu < 0.05$.

The second part of the study investigates further constraints on shallow and deep mantle heterogeneities causing plate motion by predicting lithosphere stress field and topography and validating with observations. Lithosphere stresses and dynamic topography are computed using the modeling setup and rheological parameters for prescribed plate motions. I validate my results with the World Stress Map 2016 (WSM2016) and the observed residual topography. Here I test a number of upper mantle thermal-density structures. The one used to calculate plate motions is considered the reference thermal-density structure. This model is derived from a heat flow model combined with a sea floor age model. In addition I use three different thermal-density structures derived from global S-wave velocity models to show the influence of lateral density heterogeneities in the upper 300 km on model predictions. A large portion of the total dynamic force generating stresses in the crust/lithosphere has its origin in the deep mantle, while topography is largely influenced by shallow heterogeneities. For example, there is hardly any difference between the stress orientation patterns predicted with and without consideration of the heterogeneities in the upper mantle density structure across North America, Australia, and North Africa. However, the crust is dominant in areas of high altitude for the stress orientation compared to the all deep mantle contribution.

This study explores the sensitivity of all the considered surface observables with regards to model parameters providing insights into the influence of the asthenosphere and plate boundary rheology on plate motion as I test various thermal-density structures to predict stresses and topography.

Acknowledgements

My heartfelt gratitude goes to my mentors Bernhard Steinberger and Irina Rogozhina for their continued support and interest in my research and to Micheal Weber for his supervision. The numerous discussions I have had on both the work and writing has immensely helped me with the results presented in this thesis. The opportunity to take initiatives on the topic and attend conferences frequently allowed me to present my results to other people within the geodynamic community and get further ideas for my work.

I would also like to thank Stephan Sobolev and Anton Popov for their support with regards to the modeling method used for this study and for their contribution to this write-up.

Special thanks goes to the Section's secretary Till Bruens for his help on most of the administrative issues, especially when its involves the German language. He has been very helpful and kind at all times when I need him. Likewise, Uwe Lemgo, for all the assistance given with the Section's computing infrastructure.

This thesis would not have been possible without the funding of the GeoSim graduate school of the GeoX project. I would like to thank the board members of the GeoSim project and the various PIs for their support. I benefited greatly from the various career development programs organized by the Geosim graduate school with Helmholtz. These have helped inform my career path going forward.

I would also like to thank my fellowship group NLC-Berlin for their great support during this study. They have been friends and family with whom I have shared a lot of nice times together. To my flatmate Krystian Rosenbeiger, thank you for the friendship and always being helpful when I need assistance.

Finally, a special thanks to Olivia Rose Nyembe for her support and love for the time we have been together. The encouragement she has given me when things got tough was helpful to keep working hard. I thank my parents Mr. Bright Osei Tutu and Mrs. Comfort Brago for all their support throughout my pursuit of education. Lastly, thanks to all my siblings, Evans, Franklin, Asantewaa, Paul and Frank. To "Emmanuel" you are an angel.

Contents

List of Figures

List of Tables

Dedicated to Humanity

Chapter 1

Introduction

In this chapter, I discuss the findings of previous observational and numerical studies of global plate motion, lithosphere stress field and dynamic topography. This is done by reviewing the different methods adopted in these studies and the results obtained to compare to my current study. In particular the aim of this chapter is to summarize some of the open research questions pertaining to the coupling between the lithosphere and mantle and its influence on surface processes. A special attention has been given to the past modeling techniques that describe the influence of rheological parameters and density structures on global plate motion, dynamic topography, lithosphere stress field and the geoid.

1.1 Global Plate motions

1.1.1 Observational and numerical studies

Compared to the other planets in our solar system the uniqueness of the Earth is related to the presence of plate tectonics, which is also believed to have influenced the development of the only known habitable environment (Nesbitt and Young, 1982; Raymo and Ruddiman, 1992; Veevers, 1990). This in fact has enhanced a general interest in the concept of plate tectonics and has made it a focus of numerous studies in the past few decades (e.g., Davies, 1978; Davis and Solomon, 1985; Forsyth and Uyeda, 1975; Hager and O'Connell, 1981; Turcotte and Oxburgh, 1967; Zoback, 1992; Zoback, 1989). Previous studies have enabled a relatively good understanding of the factors that cause plates to move over the low-viscosity asthenosphere. Through geological observations (DeMets et al., 2010), combined with spectral analysis (Hager and O'Connell, 1981; Conrad and Lithgow-Bertelloni, 2002) and numerical modeling (Conrad and Lithgow-Bertelloni, 2002; Minster et al., 1974; Moresi et al., 2000; Zhong and Gurnis, 1995),

the knowledge about some of the major contributing factors such as the basal driving force acting on the lithosphere due to mantle convection (i.e. internal buoyancy force), plate boundary forces such as slab pull, ridge push, inter-plate friction and trench resistance, and cratonic root resistance was developed. Each of these forces is either a driving or a resisting force contributing to the total force balance of the global plate motion. While one branch of studies has used kinematic analysis to quantify the individual forces (Becker et al., 2015; Becker and O'Connell, 2001; Davies, 1978; Hager and O'Connell, 1979; Lithgow-Bertelloni and Richards, 1998; Torsvik et al., 2010) that come into play for the plates to move, other studies (Alisic et al., 2012; Becker, 2006; Lithgow-Bertelloni and Richards, 1995; Schellart, 2004; Stadler et al., 2010) have sought to explain the rheological implications of the moving plates for both the upper and lower mantle . Nonetheless, studies that have tried to identify and quantify these individual driving and resisting forces have also arrived at non-unique conclusions regarding some force contributions. For example, Lithgow-Bertelloni and Richards (1998) suggested that subducting slabs acting at the margin of a moving plate at shallow depths together with deep mantle slab-driven flow contribute more than 90 % of the total driving forces while the remaining driving forces, coming from the push due to thickening of oceanic plates at the mid-ocean ridges, contribute less than 10 %. In contrast, lower values of about 50 % to 70 % were reported in other studies (Becker and O'Connell, 2001; Conrad and Lithgow-Bertelloni, 2002) as the slab pull contribution to the total force balance of the global plate motion. However, such studies often ignored the influence of slab bending resistive force, which has been the focus of Wu et al. (2008) and the effect of non-convective forces due to topography in oceans and continents (Bercovici and Richards, 2000), both of which are taken into account in my numerical method including an upper boundary free surface and the effect of self gravitation.

Although it is generally acknowledged that subduction influences global plate velocities (Forsyth and Uyeda, 1975; Hager and O'Connell, 1981), the contribution of a subducting plate is also influenced by factors such as plate boundary friction, slab viscosity and the asthenosphere viscosity (Alisic et al., 2012; Davies, 1978; van Summeren et al., 2012; Tan et al., 2012), making a quantification of the slab pull contribution challenging. Geodynamic modelling studies of global plate motion often ignore the frictional resistance to the slab pull force at shallow depths (e.g., Conrad and Lithgow-Bertelloni, 2004; van Summeren et al., 2012) or quantify it with the aid of the slab bending force (e.g., Wu et al., 2008), and only few studies have explored the importance of friction or plastic stress yielding at plate boundaries (e.g., Crameri and Tackley, 2015; Stadler et al., 2010). The

stress distribution along the subducting plate due to slab pull and /or deep slab suction is influenced by the frictional force at shallow depths (Davies, 1978). The frictional resistance between subducting and overriding plates is of the order of tens of MPa (Lamb and Davis, 2003; Sobolev and Babeyko, 2005), giving rise to the crustal and /or lithospheric deformation.This is evident from surface expressions of different deformation processes around the globe, such as the ongoing crustal deformation processes forming of the Tibetan Plateau due to a continental collision of the Indian and Eurasian Plates (van Hinsbergen et al., 2011) and the rifting of the African Plate induced by its interaction with the Afar plume head (Ebinger and Sleep, 1998). Sobolev and Babeyko (2005) explored the effect of frictional strength on the subduction interface on surface topography at active margins. They concluded that forming such tectonic features as observed in nature requires low friction, with a coeffcient of static friction (μ) within the range of 0.01 to 0.1 (friction angle 1° to 15°) compared to a much higher value of $\mu \sim 0.6$ suggested by laboratory experiments (Byerlee, 1978). Previous numerical models (Crameri and Tackley, 2015; Moresi and Solomatov, 1998; Richards et al., 2001; Tackley, 2000) have shown as well that the use of smaller coefficients of friction $\mu < 0.1$ (yield stress 100 MPa) would lead to plate tectonics in models of mantle convection.

Furthermore, numerical modeling of subduction (Becker and Faccenna, 2009; Gurnis et al., 2004; Hall et al., 2003; Hassani et al., 1997; Kaus et al., 2008; Sobolev and Babeyko, 2005) has demonstrated that low coefficients of friction at the subduction interface are required to sustain subduction ($\mu < 0.1$). Although these numerical studies do not consider hydration and serpentinization, as opposed to the study of Tan et al. (2012), in either case the required coefficient of friction has been estimated to be much less than $\mu \sim 0.6$ (Byerlee, 1978) for the subduction motion. At shallow depths (~60 km), where brittle deformation occurs (Oleskevich et al., 1999; Schwartz and Rokosky, 2007), friction plays an important role at subducting margins. On the other hand, at greater depths where high temperatures exist in the upper mantle, viscosity becomes the important parameter controlling the plate motion (Bercovici and Richards, 2000). Using a 2D self-consistent dynamic model, the numerical studies of Crameri and Tackley (2015), has shown that treating plate boundaries with visco-elasto-plastic rheology subduction initiates in the model. I treat our plate boundaries in a similar fashion to explore the influence of the friction coefficient on the global plate motion. Such combined frictional and viscous treatment of plate boundaries is more realistic compared to previously suggested approaches using low-viscosity/weak zones (e.g., Becker, 2006) at plate boundaries.

Below the ductile layer, I have implemented a complex upper mantle rheology due to temperature increase with depth and the presence of cold slabs and cratons. To date, many numerical modeling studies have used an oversimplified treatment of the complex upper mantle rheology and its effects on the magnitudes and directions of plate velocities using either a simplified (i.e. layered/radial) viscosity structure of the upper mantle or a parameterization of the other rheological/force contributions to match the surface observables such as plate motion (e.g., Becker and O'Connell, 2001; Conrad and Lithgow-Bertelloni, 2002; Lithgow-Bertelloni and Silver, 1998a; Steinberger et al., 2001). In contrast, the nonlinear viscosity of the upper mantle arising from cold dense subducting plates (Burov, 2011; Faccenna et al., 2007), deep penetrating cratonic roots of continents (Karato, 2010), and a wide range of temperature regimes has been the focus of more advanced modeling studies of the global mantle convection in relation to plate motion (Becker, 2006; Ghosh and Holt, 2012; Stadler et al., 2010; van Summeren et al., 2012; Zhong et al., 2000; Zhong and Gurnis, 1996). For example, Stadler et al. (2010) have found that the slab pull force in the upper mantle is better transmitted to the subducting oceanic plate, if the non-linear rheology of the slabs is considered.

1.1.2 Origin of lithospheric net rotation

Furthermore, the total balance of the plate motion forces arising from subducting slabs, viscous shearing of the asthenosphere, plate boundary plastic yielding and/or strain-weakening and the presence of continental keels triggers net rotation (NR) of the lithospheric plates with respect to the deep lower mantle (Becker and Faccenna, 2009; O'Connell et al., 1991; Ricard et al., 1991; Zhong, 2001). The NR of the lithospheric plates originates from the toroidal flow due to the pertaining lateral viscosity variations (LVVs) in the mantle (Bercovici and Richards, 2000; O'Connell et al., 1991; Ricard et al., 1991). Previous numerical studies that used NR to constrain the mantle rheology (Becker, 2006; Zhong, 2001) have shown that the largest contribution to the lithospheric NR comes from the uppermost ~400 km of the mantle. For example, Zhong (2001) has shown that NR is mainly influenced by the continental keels (~80 %), the deepest of which are placed at a depth of ~400 km (e.g. Jordan, 1975). Also slab pull acting on the plate to which the slab is attached but not the overriding plate is based on is a form of LVV that could excite NR. A similar conclusion was obtained by Becker (2006) who explored relative contributions of different mantle rheologies at different depths to the lithosphere NR in global 3D mantle flow models with both free-slip and

prescribed dynamic upper mantle conditions. Note that a perfectly layered mantle viscosity structure (i.e. no LVVs) should excite no NR. Hence, I explore the influence of LVVs within the top 300 km of the upper mantle on the NR of the lithospheric plates with our numerical method and to further constrain olivine water content in the asthnosphere.

1.1.3 Influence of asthenospheric water content on creep viscosity

The motion of the rigid decoupled lithospheric plate over the weak asthenosphere is also believed to be a consequence of the presence of water (Hirth and Kohlstedt, 2004; Karato and Wu, 1993) giving rise to a weakening of the asthenosphere (Green et al., 2010). Becker (2006) showed the effect of water content in the olivine material on the upper mantle rheology using experimental data (Hirth and Kohlstedt, 2004) and compared the resulting average creep viscosity to a commonly assumed radially stratified viscosity. An inclusion of wet olivine parameters appears to reduce the mantle viscosity by a factor ~ 50 relative to the radial viscosity, making water content an important contributor to the low-viscosity asthenosphere. Presence of water has been documented by experimental studies using magma samples from mid-ocean ridges. They have shown that at spreading plate boundaries magma contains about 0.1-0.2 wt % of water (Michael, 1995; Sobolev and Chaussidon, 1996; Danyushevsky et al., 2000) that corresponds to the water content in the mantle of 0.01-0.03 wt %. At convergent boundaries the water content slightly exceeds 0.1 wt % (Sobolev and Chaussidon, 1996). Here I will further explore the effect of lateral wet versus dry asthenospheric creep lateral viscosity on plate motion, using olivine parameters inferred from laboratory experiments and our setup for the 3D thermal structure of the upper mantle.

1.2 Lithosphere stress field and topography

1.2.1 Observed and modeled lithosphere stress field

The driving forces that cause plate motion also generate stresses in the rigid outermost layer of the Earth, coming from both shallow and deep geological processes. The lithosphere dynamics are defined by a combination of the plastic, elastic and viscous flow properties of the lithospheric material (Burov, 2011; Tesauro et al., 2012), while the evolution of the sub-lithospheric mantle is predominantly driven by the viscous flow (Davies, 1977; Forte and Mitrovica, 2001; Steinberger

and Calderwood, 2006). It has been shown that shallow processes influence both the magnitude and orientation of the lithospheric stresses. Among such processes the most important are slab pull, ridge push, trench and continental collision (deformation) (Reynolds et al., 2002) as well as cratonic root resistance (Naliboff et al., 2012), as they drive the lithosphere plate. Similarly, gravitational effect due to lateral density heterogeneities in the lithosphere and tractions from the mantle flow at the base of the moving plates play an important role. A superposition of different tectonic forces creates dissimilar orientations and regimes of the lithospheric stress field in different regions, as shown by the World Stress Map project (Bird and Li, 1996; Heidbach and Höhne, 2007; Heidbach et al., 2008; Heidbach et al., 2016).

Furthermore, on a global scale, the intra-plate stress orientation follows a specific pattern at a longer wavelength due to a large force contribution from the convecting mantle (Steinberger et al., 2001; Lithgow-Bertelloni and Guynn, 2004). This first-order stress pattern (long wavelengths) is dynamically supported, as the controlling forces correlate well with the forces driving the plate motion in most continental areas as has been shown for North and South Americas and Europe (Solomon et al., 1980; Richardson, 1992; Zoback, 1992). Ghosh and Holt (2012) and Steinberger et al. (2001) used different approaches to show that the contribution of the crust (shallow density structures) to the overall lithospheric stress pattern is rather small compared to that of the mantle buoyancy forces, amounting to ~ 10 %, except for regions characterized by high altitudes, especially the Tibetan Plateau, where the contribution is larger. In their modeling studies, the effect of the crust was determined separately by computing the gravitational potential energy from a crust model (Ghosh et al., 2013), which was subsequently applied as a correction. The contribution of the crust with a shallow lithospheric density contrast generates the second-order pattern (mid-to-short wavelength) in the stress field, mostly coming from topography and the crust isostasy (Zoback, 1992; Zoback and Mooney, 2003; Bird et al., 2006). These forces generating stresses in the lithosphere can be transmitted elastically through the plate for great distances, making the stress field problem more complicated due to the integrated contributions of forces and gradients of forces across the globe.

Constraining the modeled lithospheric stress with observations is challenging due to poor spatial coverage by the World Stress Map data (Zoback, 1992; Lithgow-Bertelloni and Guynn, 2004; Heidbach et al., 2008). An alternative way documented in the literature is to compare the strain rate estimated from the modeled deviatoric stresses (Ghosh et al., 2008) with the Global Strain Rate Map (Kreemer et al., 2003). However, the lithospheric stress in plate interiors (i.e. far

from the plate boundaries) is not well constrained with the Global Strain Rate Map. Hence, a gradually increasing coverage by the observed global stress field data serves as a motivation for studies attempting a global comparison of the observed and modeled stress field patterns including our present study. To date, two distinct approaches have been adopted to study the origin of the lithospheric stress, and each has given a relatively good fit to the observed stress field and some open questions with regards to shallow and deep mantle influence which are discussed below. On the one hand, Bird et al. (2008) have estimated the lithospheric stress from a model that disregards the mantle flow contribution and used the fit to the observed plate velocities as a sole criterion. On the other hand, Ghosh et al. (2013), Ghosh and Holt (2012), Lithgow-Bertelloni and Guynn (2004), Steinberger et al. (2001) and Wang et al. (2015) have aimed at assessing the influence of the mantle flow on the lithospheric stress field and have shown that the bulk mantle flow explains about 80 % of the stress field accumulated in the lithosphere (Steinberger et al., 2001), in both magnitude and the most compressive horizontal direction.

1.2.2 Observed and modeled dynamic topography

At a longer wavelength, the vertical component of the stress field tensor originating from the thermal convection of the mantle rocks (Pekeris, 1935; Steinberger et al., 2001) contributes to the topographic signal. This generates a high dynamic topography in regions of upwelling over the African and Pacific Large Low Shear Velocity Provinces (LLSVP) and low topography above downwellings in the regions of subduction (Hager and O'Connell, 1981; Hager et al., 1985). On the other hand, at a mid-to-short wavelength, topographic features are influenced by processes such as plume-lithosphere interaction (Lithgow-Bertelloni and Silver, 1998b; Thoraval et al., 2006; Dannberg and Sobolev, 2015) and small-scale convection in the upper mantle (Marquart and Schmeling, 1989; King and Ritsema, 2000; Hoggard et al., 2016). However, the largest fraction of topography is caused by isostasy due to variations in crustal thickness and density, as well as density variations in the subcrustal lithosphere.

A number of studies (Čadek and Fleitout, 2003; Forte and Mitrovica, 2001; Garcia-Castellanos and Cloetingh, 2011; Ghosh and Holt, 2012; Steinberger et al., 2001) have presented numerical simulations of different geophysical processes and compared their model results with observations of the lithosphere stress field, dynamic geoid, plate motion velocity and dynamic topography to better understand what processes control these surface observables. For instance, the

modeled dynamic geoid typically gives a good correlation with observations, due to a large contribution of the lower mantle (Čadek and Fleitout, 2003; Hager et al., 1985; Richards and Hager, 1984), but is sensitive to the choice of the mantle viscosity (Thoraval and Richards, 1997). However, the correlation between the modeled dynamic and residual topography is typically found to be weak (Heine, 2008; Flament and Müllera, 2012; Steinberger and Calderwood, 2006; Steinberger, 2016; Hoggard et al., 2016). The residual topography is here defined as the observed topography corrected for the variations in crustal and lithospheric thickness and density variations and for subsidence of the sea floor with age. One of the reasons for dissimilarities between the modeled and observed topography is our insufficient knowledge of the petrological properties of the upper mantle (Cammarano et al., 2011), for example, in relation to the chemical depletion of cratons in continental regions. This is further amplified by the uncertainties in the complex rheological and density structure of the upper mantle due to a wide range of temperature regimes associated with cold subducting plates and cratons, hot plumes and small-scale convection cells (Ebinger and Sleep, 1998; Thoraval et al., 2006). Another reason is linked to the deficiencies of the state-of-the-art seismic tomography models that often fail to provide the necessary detail about the density/thermal heterogeneities in the upper mantle. Also, crustal models (e.g. Laske et al., 2013) used to compute the observed residual topography are not well constrained. This is particularly a problem in continental regions where the crust is thicker and the thickness is more variable, due to the more complicated history.

1.3 This study: research problem and motivation

Advances made by mantle convection studies have deepened our understanding of how the mantle flow influences surface processes. Nonetheless, there are still some open research questions concerning different dynamic processes occurring in the shallow and deep mantle, their interaction and the respective contribution to surface observables (e.g. dynamic geoid, plate motion, lithospheric stress field topography, etc). Among such questions

1. What are the contributions of the shallow and deep structures to the total plate driving force?

2. To which extent are the topography and lithosphere stress field, defined by contributions of the shallow versus deep mantle heterogeneties?

3. What is the influence of the plate boundary rheology on plate motion and net rotation of the lithosphere?

4. How does the viscous shearing of the asthenosphere counteract the deep mantle flow forces depending on water content considering in the asthenosphere and its influence on surface processes or geophysical observables?

This set of questions serves as a backdrop to constrain rhological parameters that influence the lithosphere and mantle dynamics and to predict plate motion, lithosphere stress field and topography in agreement with observations. Achieving a better fit between the model prediction and observations will open new horizons such as: (a) Predictions in regions where observations are scarce or absent and (b) Determining regions where model predictions are insufficiently accurate due to lack of model input and model specifications.

Guided by previous mantle flow studies, I first explore the influence of the brittle deformation at plate boundaries and asthenosphere viscosity on plate motion using the observed geoid and plate velocities as constraints. Although past numerical studies have analyzed the rheological implications of each driving or resisting force for the overall plate motion, they often simplified or even neglected some critical aspects of the upper or lower mantle rheology. To fully account for the forces governing plate motion a modeling approach must include a visco-elasto-plastic rheology of the upper mantle. This is because the shearing of a mechanically weak asthenospheric layer (Barrell, 1914) contributes a mantle/viscous drag force to the overriding plates (Forsyth and Uyeda, 1975; Froidevaux and Schubert, 1975) in the presence of subducting slabs and cold continental keels. In addition, the driving force that moves overriding lithospheric plates over the low-viscosity asthenosphere is balanced by a resistive force coming from the deeply penetrating cratonic roots (Conrad and Lithgow-Bertelloni, 2006). Here, I show that matching the observed plate motion requires the use of friction coefficients at plate boundaries that are much lower than suggested by the majority of mantle convection modeling studies, namely $\mu < 0.1$ (Crameri and Tackley, 2015; Moresi and Solomatov, 1998; Richards et al., 2001; Tackley, 2000). The rigidity of the lithospheric plate requires boundaries that can easily deform to obtain the relative motion as observed in nature. In numerical calculations simpler methods of assuming low viscous zones (Becker, 2006) in subduction zones and ridges have been used to dynamically modeled global plate motions instead of using the observed plate motions as top boundary conditions. Considering plastic deformation at plate boundaries with a dynamically self-consistent modeling will also allows to evaluate the different impact of deformations occurring in either subduction zones or ridges on the plate velocities. I also explore the influence of plate boundary friction on net rotation (NR) amplitude and Euler pole location to constrain the viscosity of the asthenosphere.

As I vary the values of the rheological parameters to achieve the best fit to the observed plate motions and the geoid, I apply these parameters to predict the lithospheric stress field and dynamic topography. This is done in an iterative way in order to refine modeling parameters in our quest and to fit all the surface observables. Here I separately study the contributions of the upper mantle above the transition zone and the lower mantle as well as the combined contribution to the lithosphere stress regimes and dynamic topography by testing different methods and data sets used to describe the thermal structure of the upper mantle. I validate the modeled dynamic topography with two different observed residual topography models. One is based on seismic surveys of the ocean floor and scattered observations from continents (Hoggard et al., 2016). The second model is taken from Steinberger (2016) and is based on the crustal thickness and density from the CRUST1.0 (Laske et al., 2013). To derive the stress model I have combined CRUST 1.0 model with the thickness and thermal structure of the lithosphere estimated by Artemieva (2006) in continents, and a half-space age-dependent cooling model of the ocean floor (Müller et al., 2008). This is an improvement compared to much simpler representations of the upper mantle structure in previous studies that commonly used a thin-sheet/shell approximation (Steinberger et al., 2001; Lithgow-Bertelloni and Guynn, 2004; Ghosh and Holt, 2012; Ghosh et al., 2013; Wang et al., 2015). The method used in this present study also accounts for the presence of slabs and their corresponding impacts on the upper mantle temperature following the approach of Steinberger (2000). Stresses induced by regional and global variations in the crustal and lithospheric structure are of the order of ~ 100 MPa in magnitude across strongly uplifted continental areas (Artyushkov, 1973). It is therefore clear that including a variable lithosphere and crustal thickness in calculations is preferable over the use of a thin-sheet/shell method (Steinberger et al., 2001; Bird et al., 2008; Ghosh and Holt, 2012). In addition, I have used a seismic velocity model to derive an alternative model of the lithosphere thickness and thermal density structure and thus counterpose our results from two simulations. While studying the impacts of the shallow (upper mantle) thermal and density anomalies and lateral variations in the rheological properties on the plate motion, present-day dynamic topography and lithospheric stress state, I will also attempt to quantify the uncertainties in the thermal structure of the upper mantle and their effects on the dynamic topography.

This study uses a numerical method (Sobolev et al., 2009) that allows for a separate treatment of the small-scale features in the upper mantle and large-scale dynamic patterns in the lower mantle in a single calculation, with the upper

boundary treated as a free surface. Deriving all force contributions from a single calculation resolves any inconsistency that might arise from treating individual force contributions to the surface observables separately e.g. the lithosphere stress field, as has been done in earlier studies (Bird et al., 2008; Steinberger et al., 2001; Lithgow-Bertelloni and Guynn, 2004; Ghosh et al., 2008; Naliboff et al., 2012; Ghosh et al., 2013; Wang et al., 2015). In this study, I use a global Earth model, where deformations in the upper 300 km are computed with the 3D finite-element numerical technique SLIM3D (Popov and Sobolev, 2008) with visco-elasto-plastic rheology, coupled to a mantle flow model (Hager and O'Connell, 1981) at 300 km depth

Chapter 2

Method

Here I provide a description of the modeling technique and the set of thermal-density models used in our calculations. This is discussed in light of the new features that set this approach apart from past numerical studies of the lithosphere and mantle coupling and its influence on surface observables. In particular I detailed the governing equations describing the upper mantle rheology and the upper thermal-density structures used in the present analysis.

2.1 Model description

In this section I give a brief description of the coupled numerical model of the lower mantle flow and the deformation within the crust and upper mantle. The upper mantle component is realized through the particle-in-cell, finite element, thermo-mechanical numerical code SLIM3D (3-dimensional lithosphere-asthenosphere code) of Popov and Sobolev (2008) that solves the momentum and energy equations 2.1 and 2.2 respectively, using a semi-Lagrangian Eulerian grid and Winkler boundary condition to allow for a free surface as an upper boundary.

$$\frac{\delta \sigma_{ij}}{\delta x_j} + \rho g \hat{z}_i = 0, \tag{2.1}$$

$$\frac{DU}{Dt} = \frac{\delta q_i}{\delta x_j} + r. \tag{2.2}$$

Hereby σ_{ij} denotes the Cauchy stress tensor, x_i the Cartesian coordinates with $i = 1, 2, 3$ and ρ, g, and $\hat{z}_i$ denotes material density, gravitational acceleration and the unit vector of a downward pointing vertical axis, respectively. Also the $\frac{DU}{Dt}$ is the material derivative of U the internal energy with respect to time, q the heat

flux and r the volumetric heat source. This code has been extensively benchmarked by Popov and Sobolev (2008) with respect to various deformational processes within the crust and lithospheric mantle and also has been used in other studies focusing on lithospheric deformation processes (Brune et al., 2012; Brune et al., 2014; Brune et al., 2016; Quinteros and Sobolev, 2013). For this study I use the extention of the SLIM3D code to a global (Sobolev et al., 2009). In that modeling technique the SLIM3D code is coupled to the spectral code of Hager and O'Connell (1981) at some prescribed depth, typically 300 - 400 km (Figure 2.1c). The bottom domain solves Navier-Stokes equations with expansion into spherical harmonic degree ($l_{max} = 63$) for incompressible flow. The top domain, SLIM3D has 3 different layers (phases) representing the crust, mantle lithosphere and sub-lithospheric mantle. In my simulations I assume the thickness of the upper domain to be 300 km. In this way, the upper domain consist of the crust, mantle lithosphere including all major cratonic roots, part of the sub-lithospheric mantle and at least the upper part of the subdcuting slabs. Thus, it operates within the depth range, where the consideration of nonlinear upper mantle rheology and the use of higher spatial resolution are most important.

The coupled model does not allow for material exchange between the two model components but requires continuity of tractions and velocities at the interface. For each calculation, tractions in the lower mantle are first computed using the spectral mantle convection model component with a 3D density structure inferred from the hybrid seismic tomography model of Becker and Boschi (2002) using the velocity-to-density conversion profile (Figure 2.1a) and the radial mantle viscosity profile from Steinberger and Calderwood (2006) (Figure 2.1b). Tractions computed by the spectral model are then passed to the lithosphere-asthenosphere model as a dynamic boundary condition following a Newton-Raphson iteration procedure. At each iteration step, I prescribe mantle flow-derived tractions as a lower boundary condition in SLIM3D, and compute the flow velocities in the upper (SLIM3D) domain. Computed flow velocities at the lower boundary of the upper domain are in turn passed back to the spectral model component as an upper boundary condition. The convergence is evaluated by comparing the velocity and traction norms of two successive iterations. I run the model forward in time for half a million years with a time step of $5{\cdot}10^4$ years. At each time step I calculate net rotation of the lithosphere and plate velocities in the no-net-rotation reference frame.

$$\dot{\varepsilon}_{ij} = \dot{\varepsilon}_{ij}^{vis} + \dot{\varepsilon}_{ij}^{el} + \cdot\varepsilon_{ij}^{pl} = \frac{1}{2\eta_{eff}}\tau_{ij} + \frac{1}{2G}\hat{\tau}_{ij} + \dot{\gamma}\frac{\partial Q}{\partial \tau_{ij}} \tag{2.3}$$

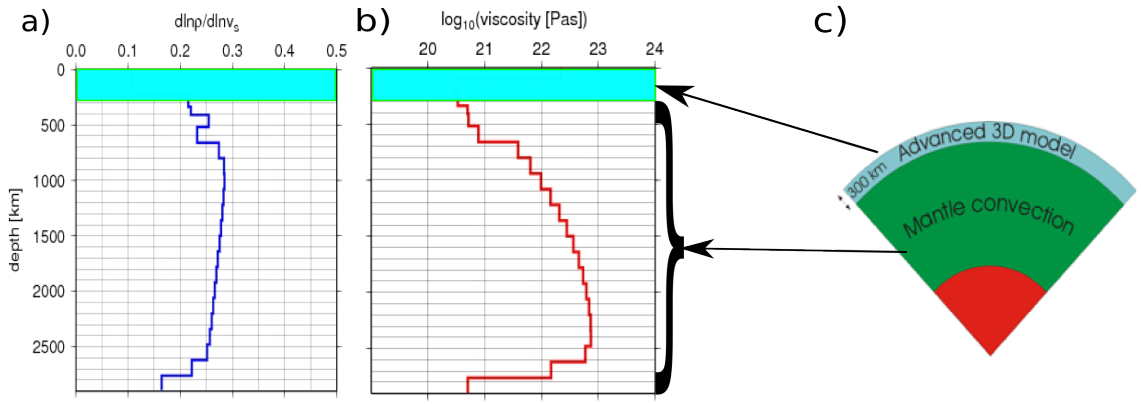

FIGURE 2.1: (a) Depth-dependent scaling profile of s-waves velocity to density; (b) radial mantle viscosity structure (Steinberger and Calderwood, 2006) and (c) a schematic diagram of the numerical method coupling the upper mantle 3D-lithosphere-asthenosphere code -SLIM3D- (Popov and Sobolev, 2008) to a lower mantle spectral flow code (Hager and O'Connell, 1981) at a depth of 300 km.

2.2 Rheology in the upper mantle

The coupling between the lithosphere and the mantle in our model allows for implementation of realistic rheological parameters for both model domains. In SLIM3D, stress-and temperature-dependent rheology is implemented according to an additive strain rate decomposition into the viscous, elastic and plastic components:

$$\dot{\varepsilon}_{ij} = \dot{\varepsilon}_{ij}^{vis} + \dot{\varepsilon}_{ij}^{el} + \cdot\varepsilon_{ij}^{pl} = \frac{1}{2\eta_{eff}}\tau_{ij} + \frac{1}{2G}\hat{\tau}_{ij} + \dot{\gamma}\frac{\partial Q}{\partial \tau_{ij}} \tag{2.4}$$

where G denotes the elastic shear modulus, $Q = \tau_{II}$ is the plastic potential function, $\hat{\tau}_{ij}$ is the objective stress rate and $\dot{\gamma}$ denotes the plastic multiplier, $\tau_{ij} = \sigma_{ij} - P\delta_{ij}$ is the Cauchy stress deviator, $P = -\sigma_{ij}/3$ is the pressure, $\tau_{II} = (\tau_{ij}\tau_{ij})^{1/2}$ stands for the effective deviatoric stress, and η_{eff} is effective creep viscosity derived by combining the diffusion and dislocation creep mechanisms, as follows:

$$\eta_{eff} = \frac{1}{2}\tau_{II}\left(\dot{\varepsilon}_{disl} + \dot{\varepsilon}_{diff}\right)^{-1} \tag{2.5}$$

The effective scalar creep strain rate are given by Kameyama et al. (1999):

$$\dot{\varepsilon}_{diff} = \mathrm{A}_{diff}(C_{H_2O})^{r_{diff}} \cdot \tau_{II} \cdot exp\left(\frac{E_{diff} + PV_{diff}}{RT}\right) \tag{2.6}$$

$$\dot{\varepsilon}_{disl} = \mathrm{A}_{disl} d^{-p} (C_{H_2O})^{r_{disl}} \cdot \tau_{II}^{n} \cdot exp\left(\frac{E_{disl} + PV_{disl}}{RT}\right) \tag{2.7}$$

where the symbols A, E and V denote the experimentally prescribed pre-exponential factor, the activation energy and the activation volume respectively.

Here and elsewhere in this paper I apply the Einstein summation convention over repeated indices. Moreover, R denotes the gas constant, T the temperature, P the pressure, n is the power law exponent, d is grain size, p is the grain size exponent, C_{H_20} is water content in ppm H/Si, and r_{diff} and r_{disl} are the water content exponents. I do not explore the varying of grain-size influence on surface observables for example, plat motion in our studies (Alisic et al., 2012).

Along plate boundaries I account for the brittle deformation, with yield stress (or plastic yielding) τ_{yield}, defined according to the Drucker-Prager criterion based on the dynamic pressure:

$$\tau_{yield} = c + \mu P \tag{2.8}$$

where c is the cohesion and μ is the coefficient of friction. Following Sobolev et al. (2009) I study the influence brittle deformation on plate motion by varying friction coefficient values at the predefined plate boundaries (Bird, 2003) treated as narrow zones in the crustal and lithospheric layer in the depth range 0-80 km and high friction coefficient (Table 3.1) in all lithospheric materials outside of the plate boundaries.

The upper mantle creep viscosity is calculated using olivine parameters from the axial compression experiments of Hirth and Kohlstedt (2004). Crustal rheology is taken from Wilks (1990). The entire rheological parameters used in this study, except for the water content which is varied in Section 3.1, are summarized in Table 3.1. For more details regarding the formulation of the physical model and numerical implementation the reader is referred to (Popov and Sobolev, 2008).

2.3 Thermal and density structure of the upper mantle

I assign densities in the topmost layers according to the CRUST1.0 crustal model (Laske et al., 2013). Underneath, I separately consider the layers below and above the interface between the two codes placed at a depth of 300 km to differentiate between the deep and shallow signals. Here the topographic signal induced by the layers below the 300 km is assumed to be due to convection in the viscous mantle although cold rigid subducting slabs (Zhong and Davies, 1999; Faccenna et al., 2007) and possibly also the deepest craton roots (Conrad and Lithgow-Bertelloni, 2006) extend deeper than 300 km. I test two different stratagies for the representation of the upper mantle thermal and density structure, namely TM1 (Figure 2.2) and TM2 (Figure 2.3). TM1 is based on a 3D thermal structure

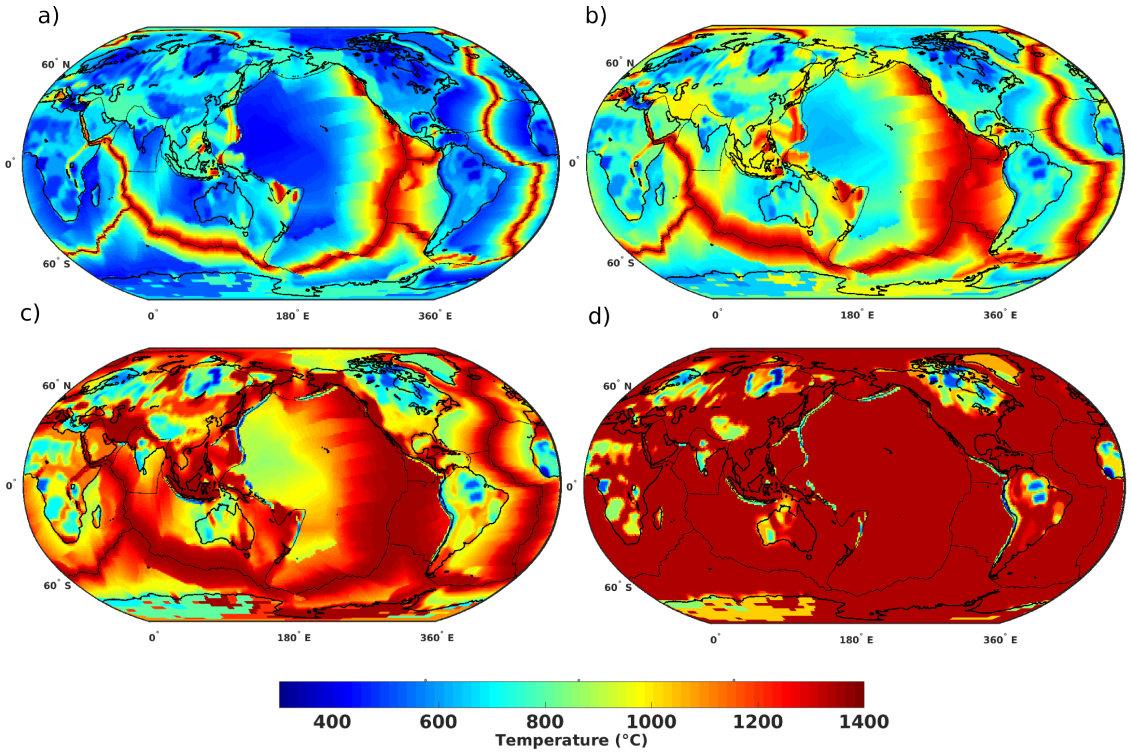

FIGURE 2.2: TM1 - 3D thermal structure at depths of a) 50 km, b) 100 km, c) 150 km and d) 280 km, showing (a) high temperature due to mid-ocean-ridges (b and c) cold cratonic roots in continents and d) cold subducting slabs along most convergent plate boundaries. Thermal structure is derived from heat flow-based thermal structure inferred from the TC1 model of Artemieva (2006) in the continents and the sea floor age model of Müller et al. (2008) in the oceanic areas.

inferred from sea floor age (Müller et al., 2008) for the mantle in oceanic regions. I use the half-space cooling model to infer temperature T_{ocean} as a function of age and depth according to:

$$\mathrm{T}_{ocean}(z,\tau) = \mathrm{T}_s + (\mathrm{T}_m - \mathrm{T}_s)\, erf\left(\frac{z}{2\sqrt{k\tau}}\right) \tag{2.9}$$

where $k = 8 \cdot 10^{-7}\mathrm{m}^2\mathrm{s}^{-1}$ is the thermal diffusivity, τ is the age of the oceanic lithosphere, T_s is the reference surface temperature, T_m is the reference mantle temperature, with z being the depth beneath the Earth's surface. This is combined with TC1 model for continents (Artemieva, 2006). To account for slabs in the upper mantle, I use slab locations and depths from Steinberger (2000) to infer a corresponding temperatures field. In figure 2.2, slices of the inferred thermal structure for the upper mantle at depths of 50, 100, 150 and 250 km, showing cratons and slabs as the coldest structures and ridges with the highest temperatures.

The second model of the upper mantle thermal structure (TM2) is inferred from the seismic tomography model SL2013sv (Schaeffer and Lebedev, 2013). I

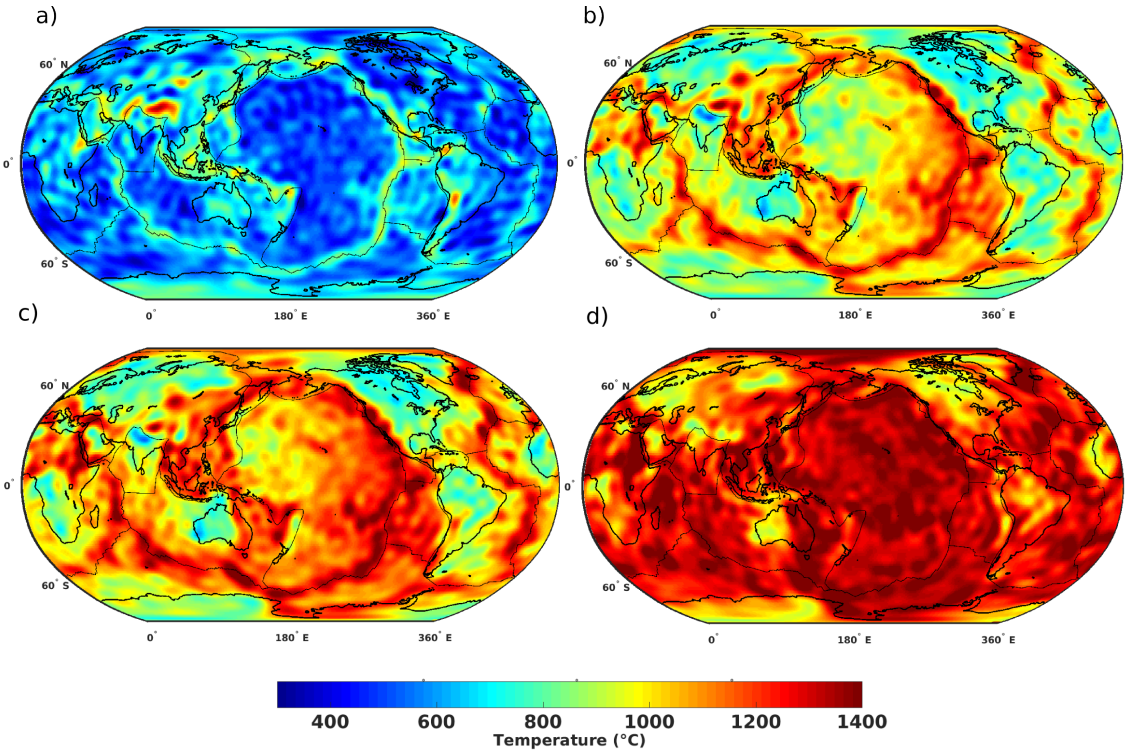

FIGURE 2.3: TM2 - second thermal structure at depths of a) 50 km, b) 100 km, c) 150 km and d) 280 km, derived from S-wave tomography-based thermal structure of the upper mantle inferred from the SL2013sv model of Schaeffer and Lebedev (2013).

have chosen this model because of its detailed representation of the upper mantle heterogeneities which has been shown by Steinberger (2016), though with layered mantle viscosity, to allow a better prediction of dynamic topography than previous models. This makes it a good candidate for comparison with the model results obtained using TM1, and for regional investigations of the upper mantle contribution to lithospheric stresses and topography. Here I convert the seismic velocity anomalies δV_s into thermal anomalies ΔT within the upper mantle according to the relation:

$$\Delta T = \frac{\left(\frac{\delta V_s}{V_s(z)}\right)}{\left(\frac{\partial ln V_s}{\partial T}\right)_P} \tag{2.10}$$

where the index P in the denominator stands for partial derivative at constant pressure (i.e. depth). As a first step, I do not correct for the effect of chemical depletion in cratons, so to evaluate its influence on the modeled lithospheric stress field and topography.

I adopt these two distinct upper mantle structures TM1 and TM2 to give insight into the performance of using the different imaging sources of TM1 and

TM2 to study the Earth's crustal and lithospheric structure. On one hand, surface wave seismic data (TM2) within the upper mantle translate all cold depleted cratons to very low temperatures and in turn low topography, which is not the case for heat flow data. Also the choice of age estimates based on magnetic lineations estimate lithosphere thickness in oceans (TM1) does not capture very well the small-scale crustal-lithospheric structure like seamounts or volcanic islands, compared to the TM2 model. Nonetheless, the choice of age-dependent lithosphere thickness based on magnetic anomalies combined with heat flow data for the TM1 model is shown to predict a better fit to the observed plate motions. Hence, I also show how that will translate to fitting the observed topography and lithosphere stress field. In addition, and for comparison purposes, we introduce two other thermal models based on two different seismic tomography models SAW24B16 (SAW) (Mégnin and Romanowicz, 2000) and S20RTS (S20) (Ritsema et al., 2011) to evaluate their performance relative to our reference seismic tomography model SL2013sv (Schaeffer and Lebedev, 2013) (Figure 2.3b). In the model setup, I define the reference crustal, lithospheric and asthenosphere densities (Table 3.1) and accounted for lateral density variations from our 3D thermal structures (either TM1, TM2, SAW or S20) using the relation:

$$\rho(\Delta T) = \rho_{ref}\left[1 - \alpha\Delta T + \frac{P}{K}\right] \tag{2.11}$$

where α is the thermal expansivity coefficient, chosen to be $3.10^{-5}\mathrm{K}^{-1}$ within the lithospheric and asthenospheric mantle, K value (Table 3.1) is the bulk modulus and ρ_{ref} the reference density at reference temperature $(20°C)$ and zero pressure. In the crustal layer, I use $\alpha = 2.7.10^{-5}K^{-1}$ with a thermal conductivity of 2.5 W/m/K and a heat production rate of 0.5 nW/kg. In the mantle, I used the value of 1.2 kJ/kg/K for the specific heat capacity and neglect the heat production since our calculation for a short time 0.5 Ma, is almost an instantaneous simulation.

Chapter 3

Results on mantle rheology and plate motion

This chapter presents the modeling setup detailing the variation of different parameters studied and the results obtained. Here I start by constraining lithosphere and mantle viscosity structure using the fit between the modeled geoid model and observed geoid. I have also tested the effects of different 3D density structures in the lower mantle on the geoid estimate. Further analysis is performed to show the influence of water content on the upper mantle rheology, which is further constrained by varying rheological parameters to calculate plate motions and lithosphere net rotation.

3.1 Constraining upper mantle creep viscosities and corresponding basal tractions

First I compute a global dynamic geoid model (Figure 3.1b) and a basal shear tractions at 300 km depth (Figure 3.5) to ascertain that the upper mantle lateral viscosity variations (LVVs) yield realistic results with the TM1 thermal structure. I compared the predicted geoid model to an estimate (Figure 3.1c) of Steinberger and Calderwood (2006) from a layered/radial viscosity (η_r) model and the observed geoid (Figure 3.1a). The corresponding spherical harmonic degree by degree ($l = 2 - 31$) amplitude spectrum of the observed and modeled geoid and the correlation between the observed and modeled geoid show high correlation and spectral density at lower degrees and a steady decrease as I move to higher spherical harmonic degrees (figure 3.1d). The introduction of LVVs in the top 300 km of the upper mantle does not significantly improve the fit to the observed geoid at high spherical harmonic degrees (red), but gives similar amplitude spectral to

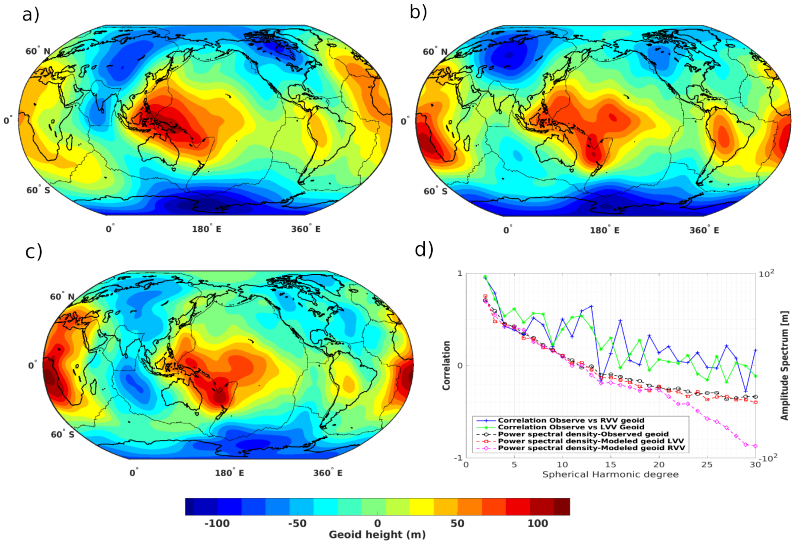

FIGURE 3.1: Comparing (a) the observed geoid from GRACE (with the effect of hydrostatic equilibrium removed) to the modeled geoid (b) using LVVs in the upper 300 km with only radial viscosity variation below and (c) with only radial viscosity variation (Steinberger and Calderwood, 2006) for all depths. The modeled geoid is estimated with the density distribution from TM1 in the top 300 km and from the Smean tomography model (Becker and Boschi, 2002) below 300 km. (d) Calculated spectral density amplitude of the observed and modeled geoid and correlation between them

the observed field compared to the geoid model with radial viscosity variation (magenta) at all depths.

The geoid model is also dependent on the density structure used for the mantle flow calculation. I have examined a number of published S and P - wave seismic tomography models to infer the lower mantle density structures causing mantle flow. For each density model derived from the respective seismic tomography model the dynamic geoid was calculated using the radial viscosity variations of Steinberger and Calderwood (2006) and compared to the observed geoid (Figure 3.2). I computed both global and regional correlations for spherical harmonic degrees $l = 2-31$ expanded into the spatial domain. Each geoid model was then compared to the observed geoid in two arbitrary regions, namely the areas marked by the Andes geoid high signal and India geoid low signal. This was done be taking an area of 40 x 40 degrees around the Indian geoid low and the Andes geoid high in spatial domain for the model and the observed geoid. I used the correlation coefficient equation:

$$r = \frac{(n\Sigma N_{obs} \cdot N_{mod} - (\Sigma N_{obs}) \cdot (\Sigma N_{mod}))}{\sqrt{([n\Sigma N_{obs}^2 - (\Sigma N_{obs})^2] \cdot [n\Sigma N_{mod}^2 - (\Sigma N_{mod})^2])}} \tag{3.1}$$

Were N_{obs} and N_{mod} are observed and modeled geoid models and n is the number of data point in the spatial domain. I also tried composite models where

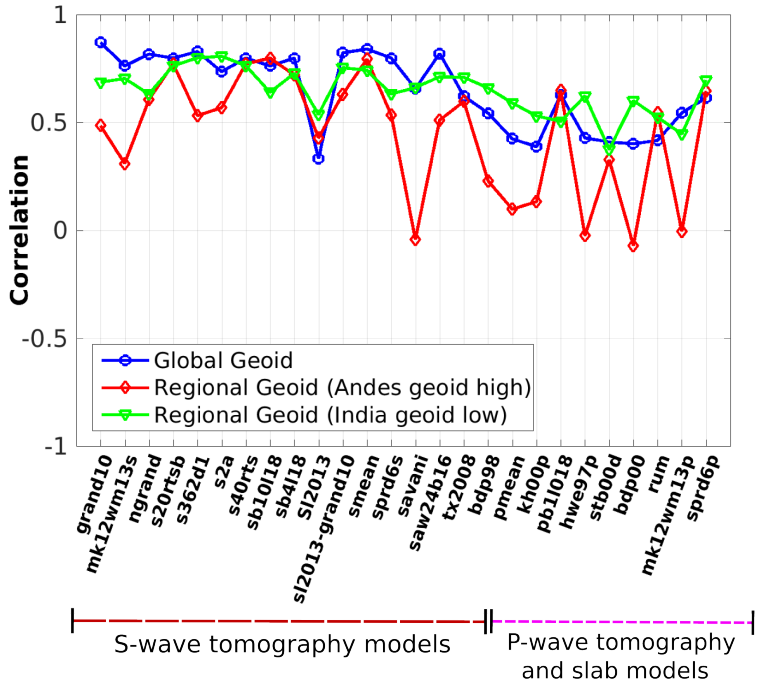

FIGURE 3.2: Testing different P-wave and S-wave tomography models against each other for mantle density distribution below 300 km with a constant lithosphere thickness (100 km) by estimating the correlation between the respective modeled and observed geoid

different seismic models were combined at a chosen depth based on whether the model performs best in capturing upper or lower mantle structures. From the analysis, the Smean seismic tomography model (Becker and Boschi, 2002) gave a rather good fit to the observed geoid with a global correlation of 0.84. When I introduced LVVs it gave a global correlation of 0.852 and similar high value for the Andes (0.86) but lower for India (0.75).

In Figure 3.4(b), I show profiles of the resulting creep effective viscosity for continents and oceans within the top 300 km. The upper mantle creep viscosity is calculated using olivine parameters from the axial compression experiments of Hirth and Kohlstedt (2004), shown in Table 3.1 with the reference 3D upper mantle thermal structure TM1 (Figure 2.2). I experimented with dry and wet olivine parameters (Table 3.1) with different water content in the asthenosphere for the dislocation and diffusion creep equations, to estimate the influence of weak asthenospheric viscosity on plate motion. The corresponding diffusion and dislocation creep estimates are shown in Figure 3.4(a).

Figure 3.4(b), shows how the average asthenospheric viscosity decreases with water content (Green et al., 2010; Karato, 2010) and a vertical profile through the upper mantle resulting LVVs (300 km) is shown in Figure 3.3. In general,

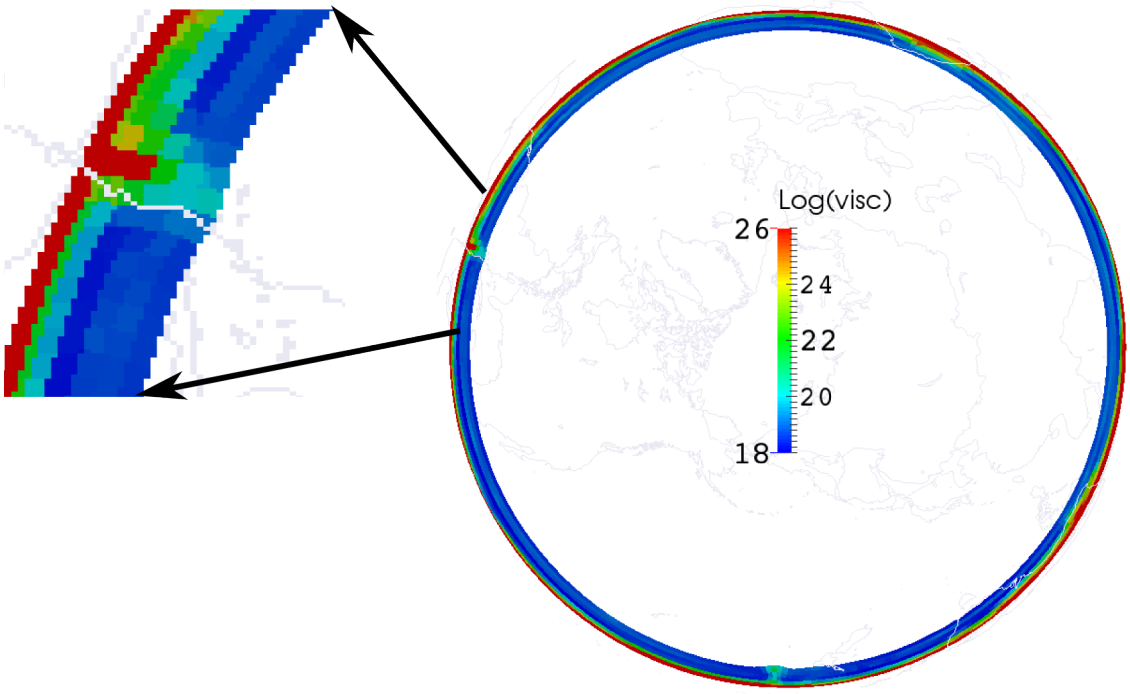

FIGURE 3.3: A slice of resulting viscosity (LVVs) using TM1 model at latitude 25° South through the Nazca subduction plate. Background lines shows North pole.

TABLE 3.1: Parameters for the thermo-mechanical modelling of the upper mantle modified after Hirth and Kohlstedt (2004). Olivine water content used for our viscosity profile is 100, 200, 500, 800, 1000 H/10^6Si in the weak mantle (asthenosphere) with dry lithospheric parameters, which is included in the pre-exponential factor for olivine. The creep parameters for the crust are given by (Wilks, 1990)

Parameter	Unit	Crust	Lithosphere (strong mantle)	Asthenosphere (weak mantle)
Bulk modulus K	GPa	6.3	12.2	12.2
Shear modulus G	GPa	4.0	7.40	7.40
Density ρ	gcm^{-3}	2.85	3.27	3.30
Cohesion c	MPa	5.0	5.0	5.0
Friction coefficient μ	-	0.6	0.6	0.6
Diffusion creep parameters (p =3, d=10 mm, r = 1)				
A_{diff}	$Pa^{-1}s^{-1}$	-	$10^{-8.65}$	$10^{-8.82}$
Activation Energy E_{diff}	KJ/mol	-	375	335
Activation Volume V_{diff}	cm^{-3}/mol	-	6.0	4.0
Dislocation creep parameters Dislocation (p = 0, r = 1.2)				
A_{diff}	$Pa^{-n}s^{-1}$	$10^{-21.05}$	$10^{-15.19}$	$10^{-14.67}$
Activation Energy E_{diff}	KJ/mol	445	530	480
Activation Volume V_{diff}	cm^{-3}/mol	10.0	17.0	14.0
Power law exponent n	-	4.2	3.5	3.5

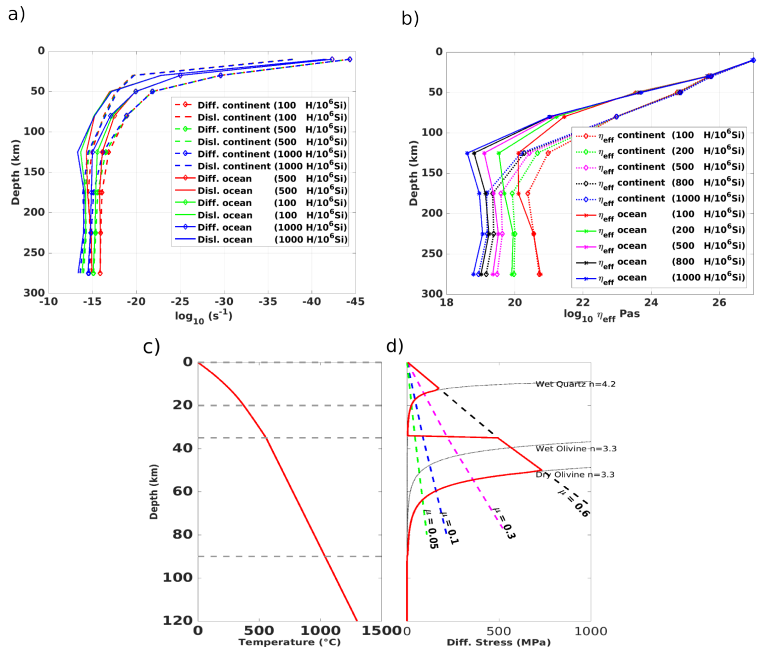

FIGURE 3.4: a) Calculated average strain rate versus depth for diffusion and dislocation creep across continents and oceans. b) The corresponding average creep viscosity versus depth in the upper mantle with olivine parameters c)Temperature and d) Yield strength profiles showing the prescribed frictional coefficient $\mu \sim 0.6$ from laboratory experiments (Byerlee, 1978) and frictional coefficient $\mu \sim 0.1$ suggested by numerical simulation(Moresi and Solomatov, 1998) used as an upper limit for plate boundaries.

all oceanic average viscosity profiles have magnitudes lower than their respective continental average effective viscosity (η_{eff}), within the 100 ± 60 km depth range, which is broadly consistent with the mean depth of the oceanic asthenosphere. This depth range of low oceanic viscosity (Figure 3.4b) corresponds to seismic wave velocity drop (~ 5-10 %) in most recent seismological studies showing the transition between lithosphere and asthenosphere (e.g. Fischer et al., 2010; Kawakatsu et al., 2009; Rychert et al., 2005; Schaeffer and Lebedev, 2013). The difference between the averaged ocean and continent viscosity profiles in the depth range 100 ± 60 km is ~ 1 order of magnitude. I obtained the lowest average viscosity of $\sim 5 \cdot 10^{18}$ Pas, for 1000 H/10^6Si wet olivine beneath oceans. Figure 3.5 shows the basal tractions causing plate motions for some representative cases. In Figure 3.5 (a) and (c) only radial viscosity variation (Steinberger and Calderwood, 2006) are considered, whereas in Figure 3.5 (b) and (d) creep parameters corresponding to the effective viscosity profile in Figure 3.4 (b, blue profile) are used, with yield stress adjusted with coefficient of friction $\mu = 0.03$ (Figure 3.4d) within the crust and lithospheric layer for all plate boundaries. The influence of the frictional parameter at plate boundaries will be discussed in the following sections with regards to global plate motions.

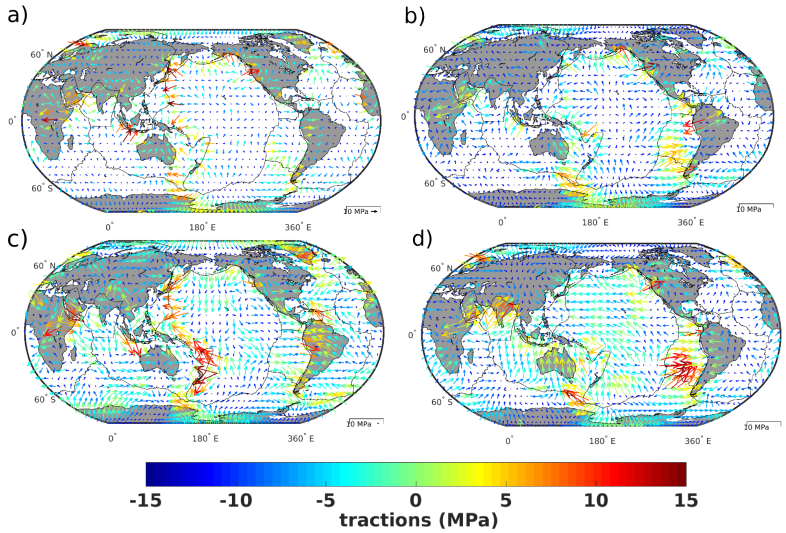

FIGURE 3.5: Predicted basal tractions at a 300-km depth with a) layered viscosity structure (Steinberger and Calderwood, 2006) and b) Olivine parameters for pink profile average creep viscosity (500 H/10^6Si, in figure 3.4b) with $\mu = 0.03$. c) and d) with one order of magnitude lower viscosity in the asthenosphere, with $\mu = 0.03$ at ocean-continent subducting regions and $\mu = 0.1$ at the remaining plate boundaries. The predicted geoid models with a) and b) are shown in figure 3.1(b-c)

3.2 Plate motions

I first used the coupled model to predict a set of global plate motions (Figure 3.6), following upper mantle creep parameters derived with dynamic geoid and lithospheric basal tractions (Figure 3.4) and a free surface as the upper boundary. I seek to understand how plate boundary frictional deformation and asthenosphere viscosity influence global plate velocities. To compute global plate motions in no net rotation reference (NNR) frame, I have explored both layered/radial viscosity and LVVs for the upper mantle. For LVVs I first used olivine parameters (Table 3.1) corresponding to the blue average creep viscosity profile (1000 H/10^6Si in Figure 3.4b). I used a fixed maximum and variable minimum cutoff in the top 300 km (see Table 3.2) and yield stress with parameterized coefficient of friction (Figure 3.4d) at plate boundaries. The predicted global plate motions (Figure 3.6) are compared with the observed plate motion model NUVEL-1A (DeMets et al., 2010) in a No-Net-Rotation (NNR) reference frame. I estimated and compared the global root mean square (rms) velocity (Figure 3.7a and 3.7b) and the angular misfits (Figure 3.7c and 3.7d) between the modeled and observed plate velocities for the different values of plate boundary friction coefficient due to plastic yielding and asthenospheric cutoff viscosity. Here I used a variable

TABLE 3.2: Summary of the upper mantle parameters for different calculations

Upper Mantle	Lateral Viscosity Variations (Pas)	Layered Viscosity Variations (Pas)
1. **Lithosphere layer** a. variable thickness b. uniform thickness $(60, 80, 100\, and\, 150km)$	 η_{eff} max cutoff = 10^{24} η_{eff} max cutoff = 10^{24}	10^{24}
2. **Asthenospheric layer**	η_{eff} min cutoffs = 10^{18} - 10^{21}	$\eta(z)$ = 10^{18} - 10^{21}

lithosphere thickness (Table 3.2) with the stress and strain-rate dependent viscosity using a 3D temperature structure for the upper mantle (Figure 2.2) to predict my first set of plate velocities. The second set of predicted plate motions, is based on Newtonian/layered viscosity structure (Steinberger and Calderwood, 2006) at all depths. The calculation with layered/radial viscosity for the upper mantle is similar to previous geodynamic modeling studies of the plate motion (Lithgow-Bertelloni and Richards, 1998; Becker and O'Connell, 2001), but I have imposed plastic yielding at the plate boundaries for the dynamically self-consistent generation of plate motion, in contrast to either imposing the observed surface plate velocity (Becker, 2006; Becker and O'Connell, 2001) or using weak zones with viscosity drop (Becker, 2006; Conrad and Lithgow-Bertelloni, 2006) at the plate boundaries.

3.2.1 Influence of plate boundary friction on plate velocities

Contributions of the slab pull (Conrad and Lithgow-Bertelloni, 2002; Conrad and Lithgow-Bertelloni, 2004; Forsyth and Uyeda, 1975; Harper, 1975; van Summeren et al., 2012) from the upper mantle slabs attached to surface plates and of the deeper slab suction to global plate motion are broadly evident in all subducting surface plates, when I use a very low plate boundary friction $\mu < 0.04$ (Figure 3.6) and a relatively low asthenosphere viscosity. The Pacific plate, Nazca plate, Indo-Australian plate and Cocos plate are all moving with a maximum speed ~20 cm/yr. On the other hand, with the same low coefficient of friction μ <0.04 at plate boundaries and asthenospheric viscosity, the non-subducting oceanic plates are moving with relatively low velocity ~5 cm/yr, which are mainly driven by forces coming from either ridge push or gravitational sliding of the oceanic plate (Artyushkov, 1973; Conrad and Lithgow-Bertelloni, 2002; Harper, 1975; McKenzie, 1972) or slab suction from below 300 km. When I increase the resistive force due to friction by increasing the coefficient of friction at plate boundaries while keeping the same asthenospheric viscosity, I observe a corresponding decrease in

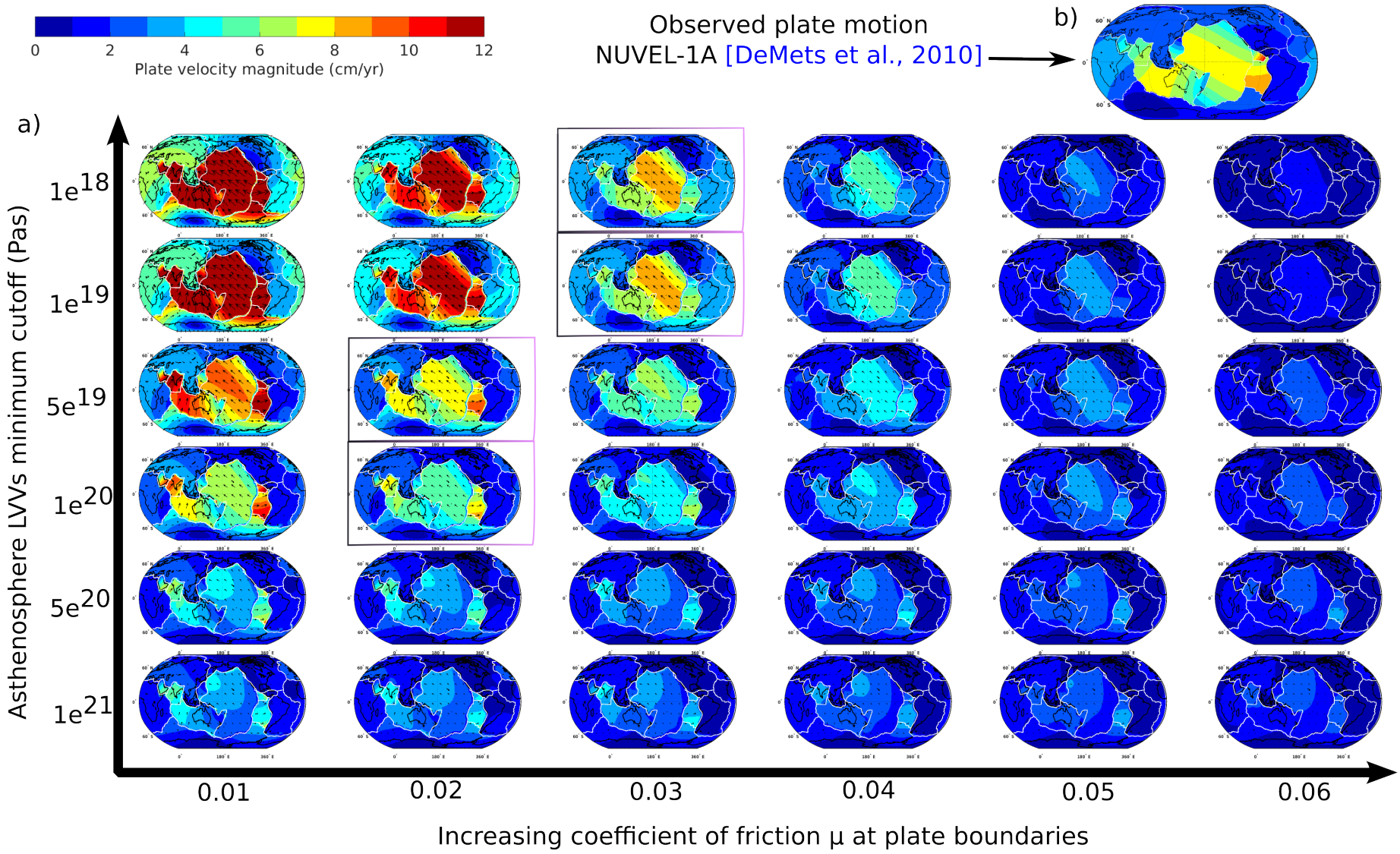

FIGURE 3.6: (a)Predicted plate motions with increasing coefficient of friction (plastic yielding) at the plate boundaries for different minimum viscosity cutoff values of the asthenospheric LVVs with Olivine parameters corresponding which gives the blue creep profile in Figure 3.4. I show here plate motions derived with coefficient of friction upto 0.06. The rectangular boxes show possible best fit to the observed field shown in (b) (DeMets et al., 2010).

lithospheric plate speed, for all plate, which is more pronounced in subducting plates. For example, with a minimum asthenosphere viscosity cutoff (10^{18} Pas) rms plate velocity decrease by about 2 cm/yr with an increase of the coefficient of friction (yield stress) by 0.01 (Figure 3.6). This brings lithospheric plates to an almost stagnant lid regime as I move towards higher coefficients of friction ~0.1 (Crameri and Tackley, 2015; Crameri and Tackley, 2014), thereby resisting almost the total driving force due to slabs and basal traction. With the highest coefficient of friction ~0.1 tested in this study, the yield stress at plate boundaries is mostly not reached, even with the lowest asthenospheric viscosity 10^{18} Pas. This corresponds to a general decrease in the rms predicted global plate velocities (Figure 3.7a) as I increase the coefficient of friction from 0.01 (friction angle ~1°) to 0.1 (friction angle ~15°) for all minimum viscosity cutoffs. A similar gradual decrease in global plate velocities (rms) is obtained with layered viscosity models (Figure 3.7b).

Previous studies (e.g. Wu et al., 2008) have considered slab bending force at subductions zones, and have arrived at similar conclusions on the effect of resistive forces between subducting and overriding plates. The older is the subducting plate, the thicker and more stronger the slab pull force. Hence at intermediate coefficients of friction (e.g. 0.02, 0.03, and 0.04 for cutoff 10^{18} Pas, (Figure 3.6)) young, thin subducting plates (e.g. Nazca and Cocos) move much slower, since the smaller slab pull does not mostly cause plastic yield. In contrast, it is easier for older, thicker plates (such as the Pacific) to achieve yielding and thus to move relatively fast. On the other hand, older plates become comparatively slower as we increase the asthenospheric viscosity while keeping the same friction coefficient (see section 3.2.2).

This study finding that a low friction coefficient $\mu < 0.05$ (low friction angle < 8°) is required at plate boundaries for correctly predicting global plate motions is consistent with previous studies (Crameri and Tackley, 2015; Faccenda et al., 2009; Hall et al., 2003; Hassani et al., 1997; Sobolev and Babeyko, 2005; Tan et al., 2012) that have considered the influence of the frictional parameter on the subduction interface and numerical studies of the global plate motion with plastic yielding at plate boundaries (Stadler et al., 2010; Crameri and Tackley, 2014). In contrast, the coefficient of friction $\mu \sim 0.02$ at plate boundaries from my preferred model is much lower than the value of ~ 0.1 suggested by previous numerical studies of the mantle convection (Moresi and Solomatov, 1998; Richards et al., 2001; Tackley, 2000) or the value of $\mu \sim 0.25$ inferred by studies of seismicity and oceanic

lithospheric flexure by Zhong and Watts (2013). Also the preferred friction coefficient value is much lower than that derived from laboratory experiments (Byerlee, 1978) that suggest a value of ~ 0.6. However the estimated friction coefficients are close to the values (0.01-0.05) derived in the models of subduction orogeny in Andes (Sobolev and Babeyko, 2005).

3.2.2 Influence of the asthenosphere viscosity on plate velocities

The second quantity that is varied in the simulation (Figure 3.6), is the viscosity contrast between the lithosphere and the asthenosphere, with the minimum asthenosphere viscosity cutoff values for the LVVs, ranging from 10^{18} Pas to a much high value of 10^{21} Pas. The use of higher cutoff values leads to a gradual decrease in the modeled plate velocities. At low cutoffs <10^{20} Pas and low plate boundary friction (μ <0.04), both subducting and non-subducting plates move with a relatively high speed, with an estimated global rms often greater than 7cm/yr (Figure 3.7a), exceeding the observed rms of ~3.7 cm/yr for the global plate motion NNR-NUVEL-1A (DeMets et al., 2010). For the lowest viscosity cutoffs 10^{18} Pas and 10^{19} Pas and μ = 0.01, plates move on average with more than twice the observed plate speed, giving estimates of root mean square error (RMSE) $\sim 140 - 160$ % (Figure 3.7c, red and green lines), due to the weak mechanical coupling between the lithosphere and the asthenosphere (i.e. viscous drag). This reduces the influence mantle drag force on the overriding and subducting plates, making plates move with relatively high velocities, even in continental regions with higher resistive forces due to continental keels. Noticeably, a combination of weak viscous drag at the base of oceanic plates and strong driving force due to slab pull and mantle suction (Conrad and Lithgow-Bertelloni, 2004; Forsyth and Uyeda, 1975; Harper, 1975; Stoddard and Abbott, 1996) results in a rapid motion of the Pacific, Indo-Australia, Nazca, Cocos plates, with the predicted speed more than ~15 cm/yr.

For low asthenosphere viscosity cutoffs of <10^{20} Pas and low μ <0.04, the predicted directions of plate motion are rather similar to the observed directions from NNR-NUVEL-1A (DeMets et al., 2010), with angular misfit < ~15 % (Figure 3.7e). However, as I increase the plate boundary friction coefficient, μ >0.04 while maintaining the same low asthenosphere viscosity cutoffs of <10^{20} Pas, the angular misfit increase and the corresponding rms decreases to ~1 cm/yr or less, as the resistance at plate plates boundaries increases and become plates slower.

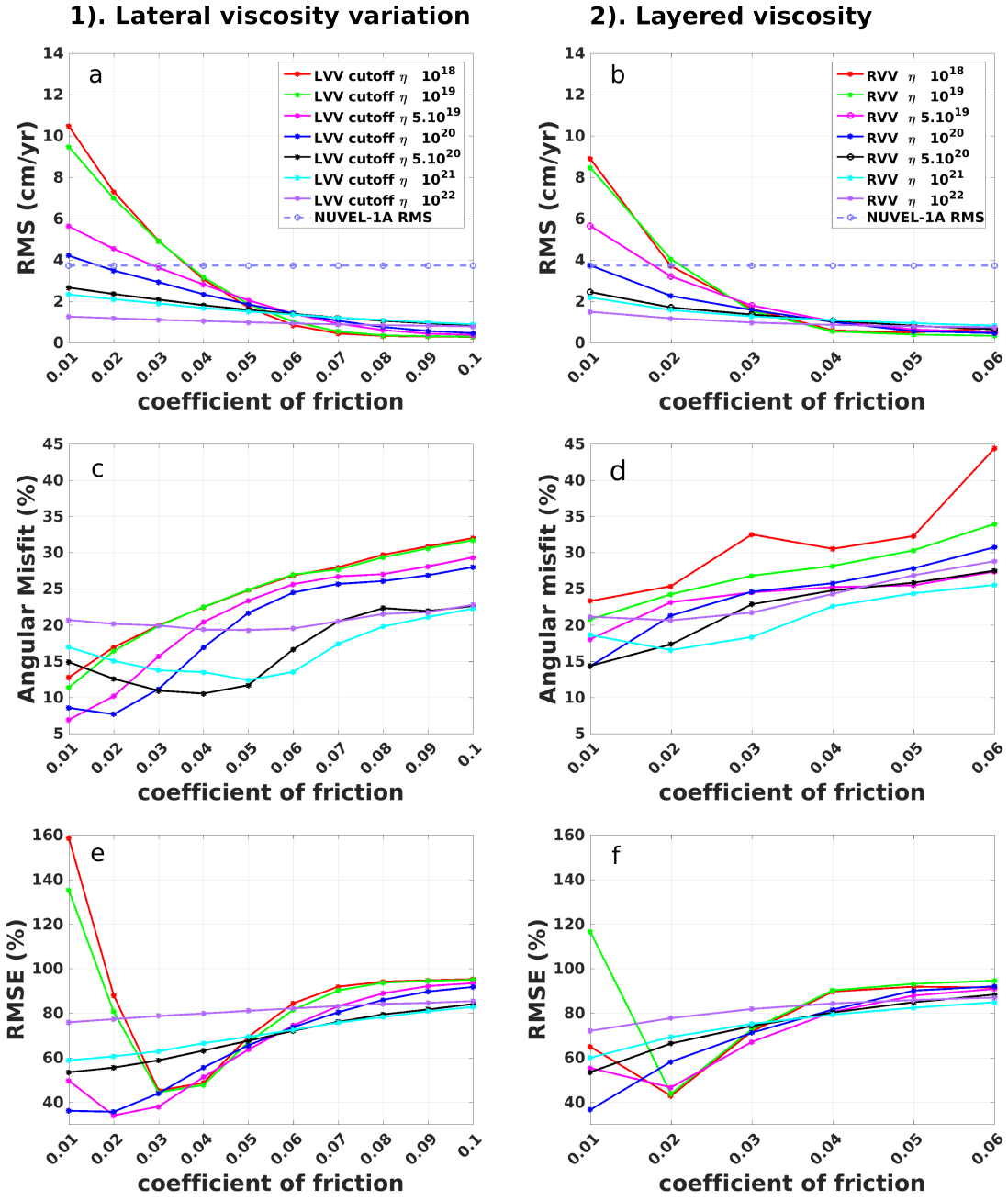

FIGURE 3.7: Estimates of global root mean square (RMS) of predicted plate motion with a) LVVs and b) layered viscosity in the upper mantle for different coefficients of friction compared to the observed rms of NNR-NUVEL-1A (DeMets et al., 2010) c) and d) depict their respective global angular misfits. e) and f) show the root mean square error (RMSE) for the velocity magnitude in percentage.

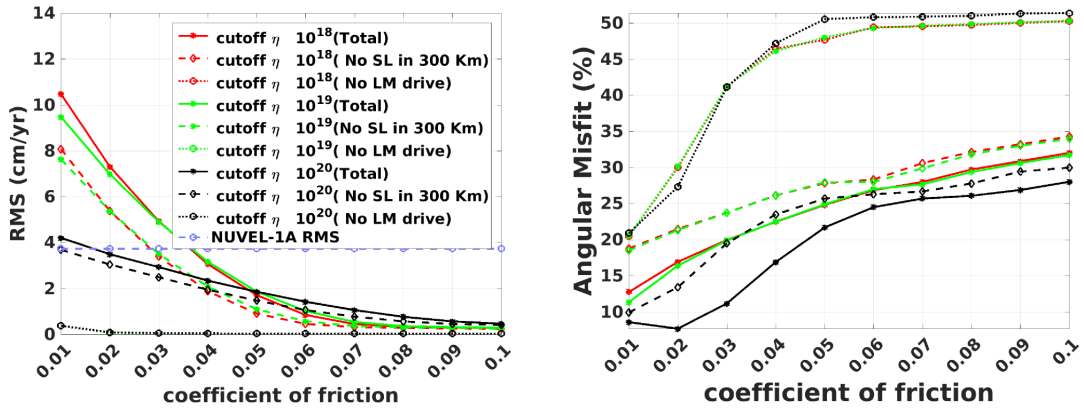

FIGURE 3.8: a) Estimated global rms velocity and b) angular misfit for modelled plate motion based on total upper and lower mantle (Total), no slabs in the upper 300 km (No SL in 300 km), and no lower mantle drive below 300 km (No LM drive)

Also increasing the minimum asthenosphere viscosity cutoffs >10^{20} Pas, deteriorates the fit between model and observation in terms of both direction (angular misfit) and magnitude (RMS) of plate motion (blue, cyan and purple profiles (Figure 3.7e), regardless of the coefficients of friction used at plate boundaries and whether or not the LVVs are accounted for.

I have quantified the contribution of slabs in the top 300 km of the upper mantle, by removing the slabs, and have found a decrease in the rms by ~20 % (Figure 3.8a) as well as and increase in the angular misfit (Figure 3.8b). The largest contribution comes from the mantle buoyancy below the coupling depth of 300 km providing about 70 % of the driving force. The angular misfit is lowest if the contributions from the upper and lower mantle are considered ((Figure 3.8)b). In particular, the angular misfit can reach 50 (°), when I set the mantle buoyancy force to zero.

My preferred model was obtained with the minimum asthenosphere viscosity cutoff of 10^{20} Pas and μ = 0.02 giving the global rms of 3.58 cm/yr and angular misfit of ~ 8 (°) (Figures 3.7a and 3.7c). I have qualitatively compared my results to the observation-based NUVEL-1A plate motion model (DeMets et al., 2010) (Figure 3.9) in a no-net-rotation reference frame. There is a generally good fit in terms of both magnitude and orientation, but an almost ~30° deviation is found in Australia and more than 40° in parts of North America (Figure 3.9)c). To achieve a better fit between model and observations in these regions I experimented with different coefficient of friction for subducting boundaries, transforms and divergent boundaries. In figure 3.9(d) I have used the minimum asthenosphere viscosity cutoff of 10^{20} Pas and μ = 0.0135 for subducting plate boundaries with half of the cohesion value and μ = 0.0219 for all other plate

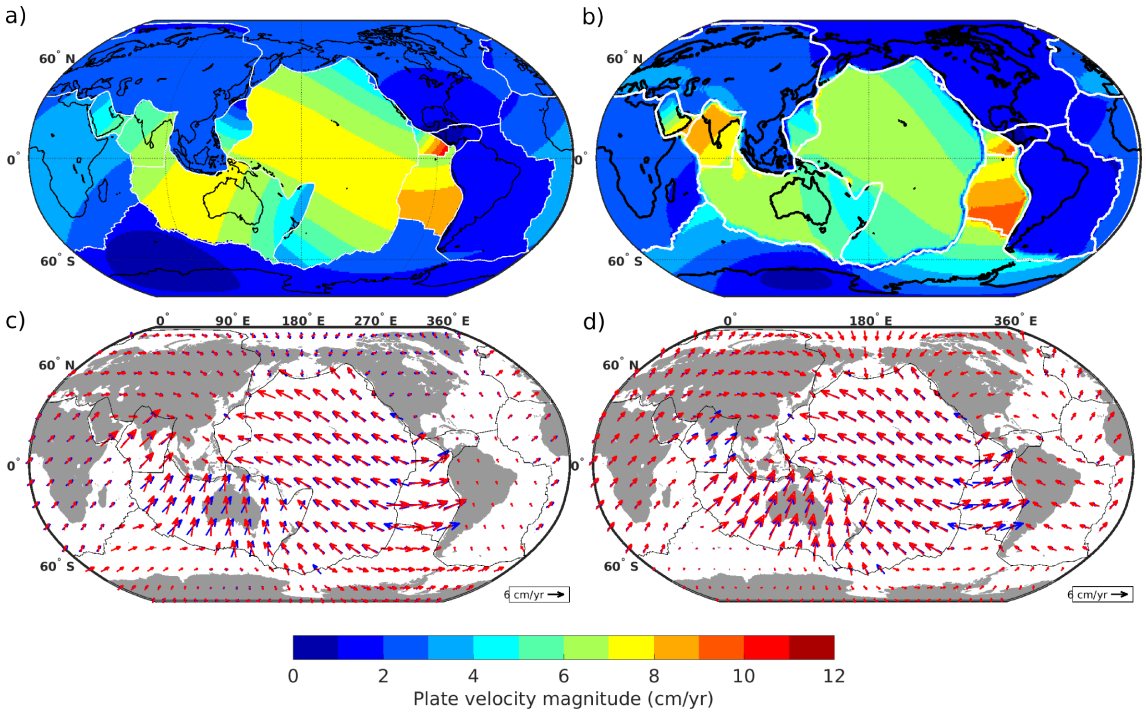

FIGURE 3.9: a). The observed plate motion NUVEL-1A in a no-net-rotation (NNR) frame (DeMets et al., 2010), b). The preferred modelled plate motions (Figure 2. min cutoff =10^{20} Pas and friction μ =0.02) c). Direction of NUVEL-1A (blue arrows) and the preferred (red) plate motion with μ = 0.02 and d). Direction of NUVEL-1A (blue arrows) plotted on the preferred (red) plate motion but with μ = 0.0121 (cohesion c= 3 MPa) for subducting plate boundaries and μ= 0.0219 for all remaining plate boundaries.

boundaries. This has resulted in an improved fit to the observed plate motion in almost all regions for both magnitude and orientation. However, using different friction coefficients for subducting plate boundaries and other plate boundaries has resulted in a westward motion of North and South America at a higher speed of ~ 5 cm/yr and also the fit deterioration in the Nazca plate.

On average, the predicted plate motion is faster (Figure 3.7)a) with the LVVs and a given asthenosphere viscosity cutoff than with the layered/radial viscosity ((Figure 3.7)b). This is due to relatively faster lateral asthenospheric viscosity flow that develops under oceanic plates (Becker, 2006), as a results of from the stress and strain-rate dependent viscosity implemented together with 3D thermal structure of the upper mantle. The corresponding low viscosity channel was in Figure 3.4b and discussed in section 3.2. Plate motions prediction with either LVVs or layered viscosity fit the observed plate velocities best with an asthenosphere with viscosity range of ~ 5.10^{19} - 10^{20} Pas underlying a lithosphere of variable thickness. This viscosity range is consistent with the estimted by values from post-glacial rebound and geoid studies to constrain the upper mantle

viscosity structure (Mitrovica, 1996; Mitrovica and Forte, 1997).

3.2.3 Impact of lithospheric thickness on plate velocities

Here, I further test the modeling setup with different values of uniform lithospheric thickness (table 3.2), similar to previous numerical modeling studies for global plate motion prediction (Becker and O'Connell, 2001; Conrad and Lithgow-Bertelloni, 2002; Lithgow-Bertelloni and Richards, 1995) but with LVVs in the asthenosphere (NB. Similar exercise were conducted with lateral constant temperature in asthenosphere to evaluate the influence on lithosphere NR, Figure 3.11 and 3.14). Because of these LVV beneath the nominal depth of the lithosphere base, there are still effectively cratonic roots in regions of high viscosity. The pattern of predicted plate motions with the different uniform thickness is quite similar to the pattern with variable lithospheric thickness in most regions since the basal tractions due mantle flow are not significantly changed by those LVVs that are due to the variable thickness lithosphere (Conrad and Lithgow-Bertelloni, 2006). This is especially evident when I compare the angular misfit with variable lithosphere thickness (Figure 3.7c) to the misfit with uniform thickness (Figure 3.10(1-4b). However, thin lithospheric plates (60 km and 80 km) are moving relatively fast with the largest rms ~13cm/yr and ~11cm/yr respectively, compared to thicker lithosphere (100 km and 150 km) with global rms of ~9 cm/yr and ~8 cm/yr respectively. As I increase the strength at plate boundaries for uniform lithosphere thickness, all rms estimates of predicted plate motion decrease monotonically to ~1 cm/yr or less, as in the case of the variable lithosphere model.

On average with thickness 60 km and 80 km I obtained faster plate motions than for variable lithosphere thickness, whereas 100 km and 150 km leads to rather slower speed making. This significantly higher plate velocities for young lithosphere plates (60 km and 80 km thickness) are due to the correspondingly thicker asthenosphere, which decreases the internal mantle traction by almost a third (Conrad and Lithgow-Bertelloni, 2006; Stoddard and Abbott, 1996) resulting in less resistance from viscous/mantle drag to the slab pull force or mantle drive. On the other hand, the plate velocities with thicker lithosphere are slower, because of the larger internal mantle drag force through the thin asthenospheric layer at the base of the lithosphere is much stronger (Conrad and Lithgow-Bertelloni, 2006; van Summeren et al., 2012) providing more resistance to the driving force. The thinner the asthenospheric layer, the stronger driving force is required to match observations. van Summeren et al. (2012) showed that, with no asthenosphere, 100 % slab pull is required to match observation. Among the four uniform

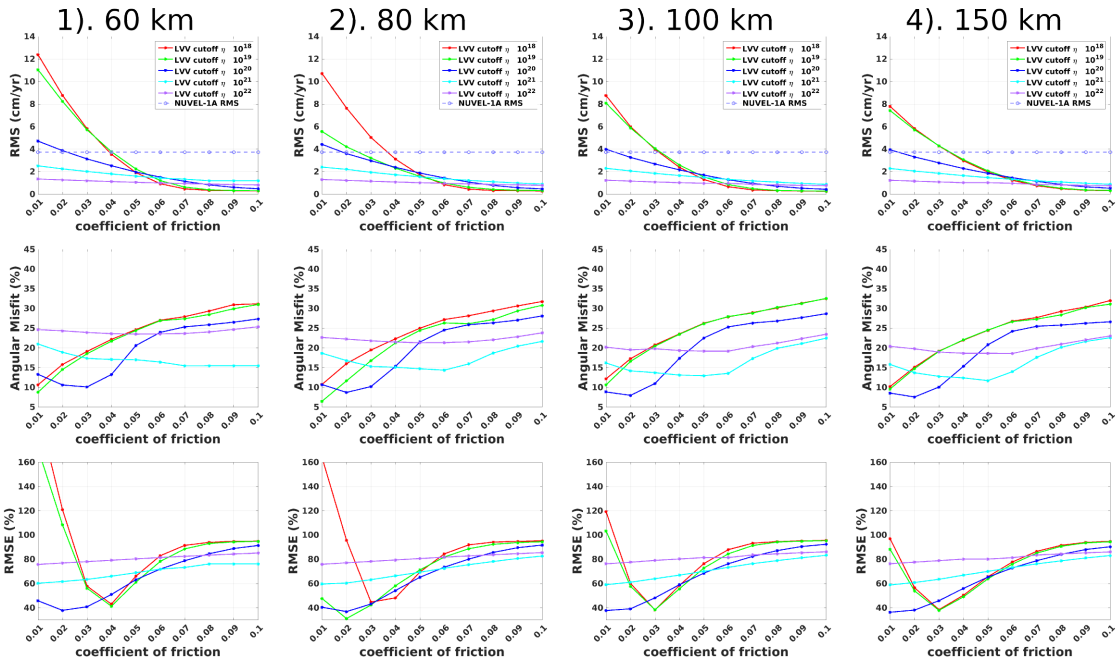

FIGURE 3.10: Modeled global plate motion rms, angular misfits and rms errors for the models using uniform lithosphere thickness of 60, 80, 100 and 150 km, with plate boundary friction ranging from 0.01 to 0.1 and LVVs for the upper mantle.

lithospheric thickness values used, 100 km yields results most comparable with the variable lithospheric thickness. Both were able to approximately match the observed plate motion NUVEL-1A, with similar asthenosphere viscosity cutoff and plate boundary friction.

3.3 Resulting net rotation

3.3.1 Net rotation amplitude - Variable lithosphere thickness

Here, I estimate the excitation of net rotation (NR) of the lithosphere by the LVVs, which is also to some degree influenced by the effect of plastic yielding at the plate boundaries. I do this for different coefficients of friction at the plate boundaries and for different asthenospheric viscosity cutoff as in the previous sections. In Figures 3.12 and 3.13, I plot the amplitudes of NR and Euler pole locations for different asthenospheric viscosity cutoff values against increasing the strength at plate boundaries varied through the of coefficient of friction, for variable and uniform lithospheric thickness. I have also tested whether the NR is generated by layered viscosity when only the influence of the friction coefficient at plate boundaries is taken into account (Steinberger and Calderwood, 2006) (Figure 3.12b and 3.12d). Theoretically, the layered viscosity structure should not

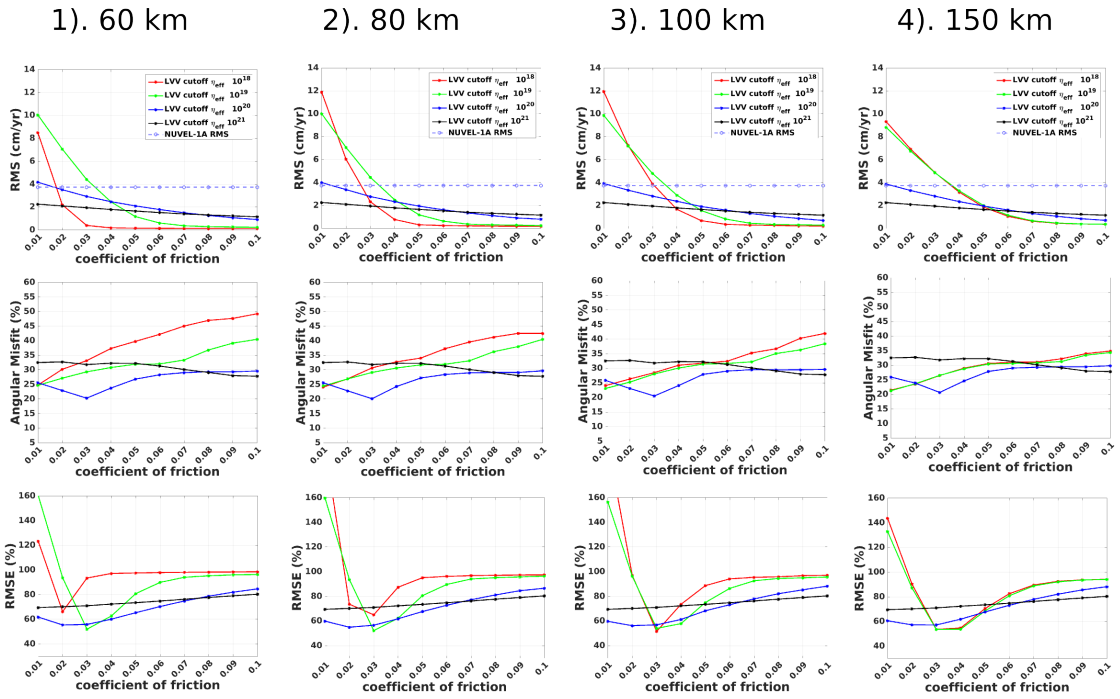

FIGURE 3.11: Modeled global plate motion rms, angular misfits and rms errors for the models using uniform lithosphere thickness of 60, 80, 100 and 150 km, with plate boundary friction ranging from 0.01 to 0.1 and and constant temperature in the asthenosphere.

excite any significant NR, and most numerical studies have shown it to be less than 0.1 % ($\omega°$/Ma) of the observed. With the introduction of plastic yielding at plate boundaries, I have obtained relatively low amplitudes of NRs, which are mostly < 0.1°/Ma.

Net rotation is close to zero for the asthenosphere viscosity larger than 10^{20} Pas. The corresponding Euler pole locations (Figure 3.12c) with coefficients of friction $\mu < 0.03$ are in the Indian Oceans rather close to most of the observation-based Euler poles, but as we increase the friction at the plate boundaries, the pole location moves further away, similar to the findings of Becker (2006) who used strain-rate dependent rheology. Plastic yielding at the plate boundaries combined with the layered viscosity structure tends to yield Euler poles further away from the observation-based poles locations. Taken together with the low NR amplitudes, this shows the importance of the LVVs in generating NR previously suggested in numerical studies (e.g., Alisic et al., 2012; Becker and Faccenna, 2009; O'Connell et al., 1991; Ricard et al., 1991; Stadler et al., 2010; Zhong, 2001). Figure 3.12(a) shows that simulation with variable lithosphere thickness, stress and strain-rate dependent viscosity and a 3D thermal structure of the upper mantle are able to realistically reproduce the NR comparable to observations in a hotspot reference frame only for a low asthenosphere viscosity with cutoff of < 10^{20} Pas

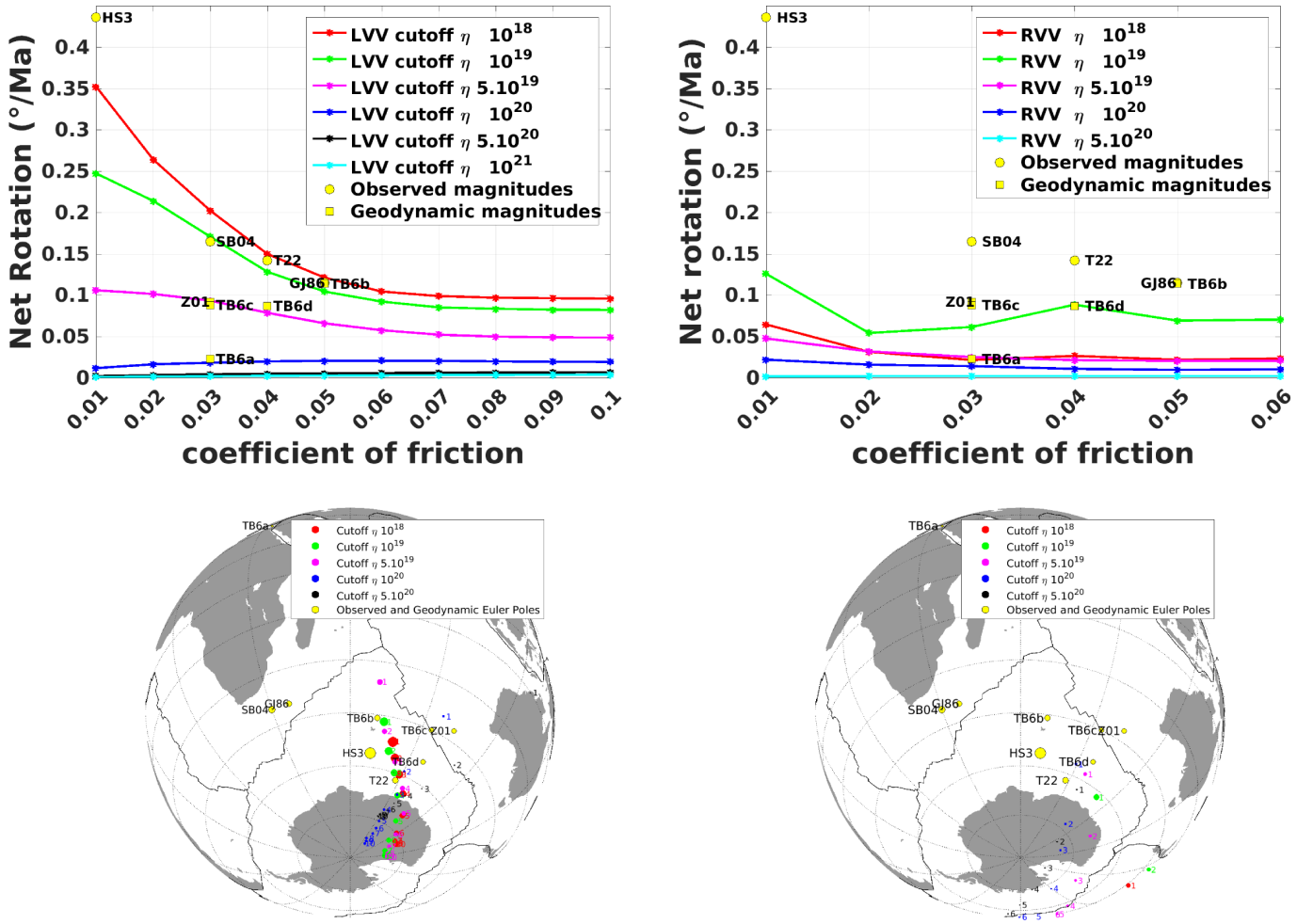

FIGURE 3.12: Net rotation amplitudes and Euler pole locations of the lithospheric plates with respect to the lower mantle for the LVVs(a and c) and layered viscosity variation(b and d). Published NR amplitudes and corresponding Euler pole locations from observations and previous geodynamic studies are plotted as yellow circles and squares respectively, with size (in planes c and d) corresponding to the amplitude(Gordon and Jurdy, 1986; Gripp and Gordon, 2002; Steinberger et al., 2004; Wang and Wang, 2001; Becker, 2006; Stadler et al., 2010; Zhong, 2001). Location of both the observed and previous geodynamic NR magnitude are only considered in y-direction with x-direction arbitrary take at μ values close to our results, which are mainly less than 0.06.

(Gordon and Jurdy, 1986; Steinberger et al., 2004; Torsvik et al., 2010; Wang and Wang, 2001). Most of these observation-based estimates - with the exception of HS3 (Gripp and Gordon, 2002)- fall within in the range of 0.1 - 0.2 °/Ma. Similar large of NR amplitudes were also reported by Alisic et al. (2012), who used a self-consistent global mantle flow model, which also accounted for the nonlinear slab rheology and plastic yielding at the plate boundaries.

On the other hand other, earlier 3D numerical studies of the global mantle flow (Becker, 2006; Zhong, 2001), with weak zones at the plate boundaries and a free-slip upper boundary condition estimated smaller NR magnitudes between 0.023 to 0.092 °/Ma. This wide spread among different numerical predictions of the NR amplitudes and significant deviations from observations (Čadek and Fleitout, 2003; Wen and Anderson, 1997; Zhang and Christensen, 1993), are due to different rheological models in the upper mantle structure, and the choice of the plate boundary deformation mechanism. With larger lithosphere-asthenosphere viscosity contrast, for example with a minimum cutoff of 10^{18} Pas or 10^{19} Pas for the asthenosphere viscosity and $\mu < 0.03$ I obtain NR amplitudes that are larger than most observation-based estimates. For cutoffs values below 10^{20} Pas, there is a monotonic decrease in the NR amplitudes when I increase the coefficient of friction from 0.01 to 0.1. For example, the NR amplitude from 0.365°/Ma to 0.143°/Ma if the asthenosphere viscosity cutoff of 10^{18} Pas and variable lithosphere thickness are used. A viscosity cutoff of $5{\cdot}10^{19}$ Pas combined with low plate boundary friction $\mu{\sim}\,0.03$ or less gives net rotations which is similar to but with somewhat lower amplitude than most of the observation-based values, and also similar to the results of Becker (2006) with temperature and strain rate dependent rheology. However, if I reduce the lithosphere-asthenosphere viscosity contrast by assigning cutoff values of 10^{20} Pas or greater, the predicted average NR amplitudes fall below 0.03 °/Ma which is similar to NR with the layered viscosity models (Figure 3.12b) and the prediction of Becker (2006) with only strain-rate dependent rheology. A Similar conclusion also follows from theoretical results (Conrad and Behn, 2010; O'Connell et al., 1991; Ricard et al., 1991) that showed that a viscosity variation by at least one order of magnitude is needed to excites observed-like net rotation.

A gradual decline in the NR amplitudes with increasing plate boundary friction and asthenosphere viscosity cutoff < 10^{20} Pas supports the idea that a significant weakening at the plate boundaries is required to excite lithospheric net rotation (Bercovici and Richards, 2000; Zhong et al., 1998). However, the largest effect is induced by the upper mantle viscosity. This is in accordance with the notion that NR of the lithosphere is largely controlled by the LVVs resulting

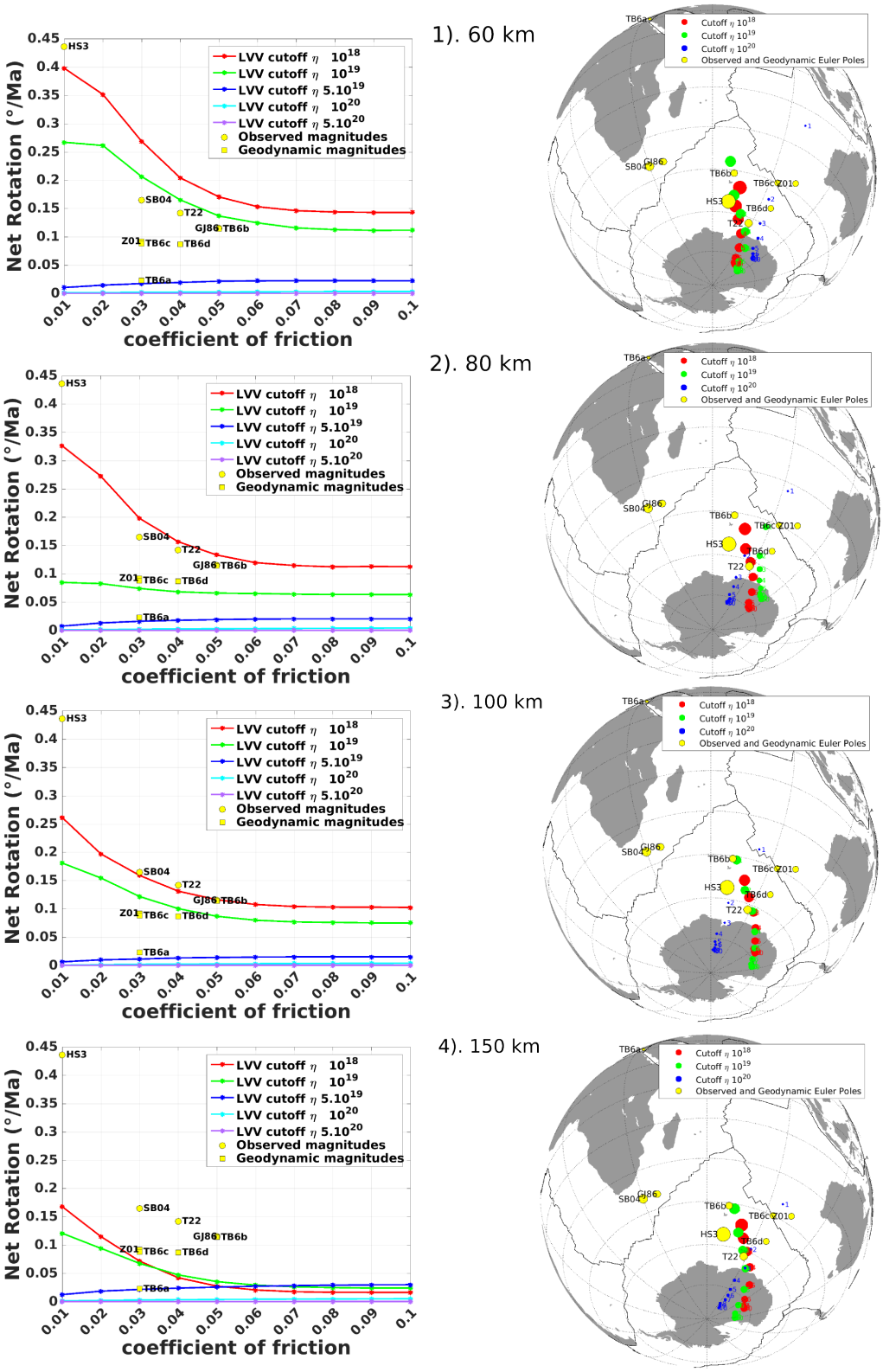

FIGURE 3.13: Net rotation amplitudes and Euler pole locations from simulations with uniform lithosphere thickness of 60, 80, 100 and 150 km.

from the sub-continental and sub-oceanic structures, mainly continental keels (Zhong, 2001), which was also supported by Becker (2006) who used a model with strain-rate and temperature-dependent LVVs, and Gérault et al. (2012) using low-viscosity plate boundaries. Becker (2006) showed that models with strain-rate and temperature-dependent rheology yield NR amplitudes close to observations in a hotspot reference frame, while the use of a strain-rate dependent rheology resutls in an amplitude under estimations.

The resulting predicted Euler pole locations (Figure 3.12c) are mainly confined in and around the Indian Ocean, with the location moving southward towards the Antarctic continent as I increase the plate boundary friction to 0.1. This result is robust for almost all asthenospheric viscosity cutoff values, even those that generate smaller NR amplitudes. With friction coefficients $\mu < 0.04$ and asthenosphere viscosity cutoff of $< 10^{20}$ Pas, I am able to predict Euler pole locations in the vicinity of the observed present-day NR Euler pole locations (Gordon and Jurdy, 1986; Gripp and Gordon, 2002; Steinberger et al., 2004; Wang and Wang, 2001), and those obtained from previous numerical studies (Becker, 2006; Stadler et al., 2010; Zhong, 2001).

3.3.2 Net rotation amplitude and Euler Pole location - Constant lithosphere thickness

Next I test how the choice of the lithospheric thickness influence the predicted net rotation by considering different uniform lithospheric thickness. The thinnest lithosphere (60 km) excites the largest NR amplitude, while the thickest (150 km) excites the least for asthenosphere viscosity cutoff $< 10^{20}$ Pas. For the different uniform lithospheric thickness, the corresponding asthenosphere with LVVs still contains density and viscosity variations due to slabs and cratons. Hence the 60 km thick lithosphere is associated with an asthenosphere up to 240 km thick, but in regions of high viscosity, the nominal asthenosphere will still accommodate deep cratonic roots. Accordingly, combining a 60 km thick lithosphere with $\mu = 0.01$ excites the largest NR amplitude of 0.410 °/Ma. Similarly, Zhong (2001) finds a contribution of the continental keels to the lithospheric NR of about ~80 %. As an important component in the LVVs of the mantle structure continental keels are know to generate lithospheric NR (Becker, 2006; van Summeren et al., 2012; Zhong, 2001). Among the computed NR with uniform lithosphere thickness, those generated by simulations with a 100 km thickness are most similar to the results of models with variable lithosphere thickness. When I consider uniform temperature in the asthenosphere, almost all NR estimate goes below

0.05 % (ω°/Ma) for $\mu > 0.02$ Figure 3.14. This confirms the importance of sub-continental and sub-oceanic structures, (Zhong, 2001) with regards to lithosphere net rotation. LVV seem to be the cause for the net rotation hence anything that causes LVV to be reduced/minimized should diminish the NR. High friction coefficient or larger asthenosphere viscosity both tend to strengthen the weakest points of the lithosphere/asthenosphere, making them closer in strength to the rest of the lithosphere/asthenosphere.

3.3.3 Water content in the asthenosphere

Lastly, I study how a weak asthenosphere flow due to high olivine water content (see section 3.1 (Figure 3.4b) influences the lithospheric net rotation. Here I do not apply an asthenosphere viscosity cutoff. Modeled plate velocities with 1000 H/10^6Si in the asthenosphere exceeds ~20 cm/yr leading to the largest net rotation amplitude of up to ~ 0.8349°/Ma (Figure 3.15(a) red profile) and also giving global rms > 14 cm/yr for $\mu = 0.01$ (Figure 3.16). A two fold decrease in the olivine water content (i.e. 500 H/10^6Si) in the asthenosphere, results in lower net rotations, similar to most of the observation-based estimates of around 0.1-0.2°/Ma, even for low coefficients of plate boundary friction $\mu = 0.03$ or less. When I increase the plastic yielding at a plate boundary, I observe a monotonic decrease in the NR amplitudes similar to the previous calculations. The Euler pole locations (Figure 3.15b) for different olivine water contents in asthenosphere do not deviate significantly from each other, but all show a similar southward drift for higher values of the plate boundary friction.

3.4 Concluding Remarks

In this part of the study, I have quantified the effect of plastic yielding/friction at plate boundaries and the presence of creep viscosity on present-day global plate velocities. Results presented here show that frictional deformation at plate boundaries controls both the magnitude and orientation of plate velocities. Compared to values μ~0.1 proposed in other studies, I find that the friction coefficient value must be much lower in order to match observations. The better fit with rather smaller friction coefficient in subduction zones could be due to additional lubrication from sediments and water between the subducting and overriding plates as observed in nature (Lamb and Davis, 2003; Huene and Ranero, 2003). Also, the asthenosphere viscosity structure influences both the plate velocity magnitude and net rotation as proposed by previous studies. Introducing

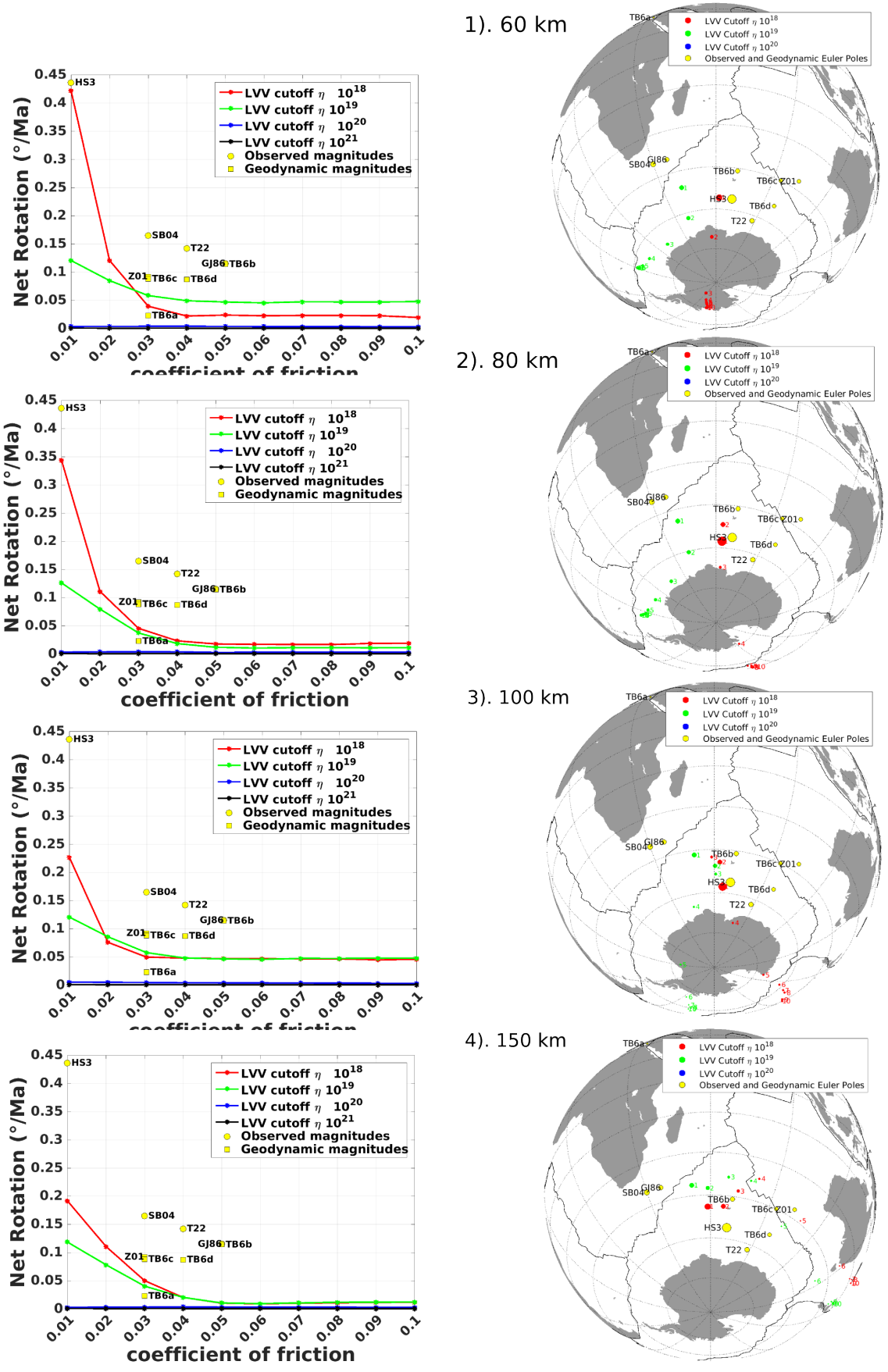

FIGURE 3.14: Net rotation amplitudes and Euler pole locations from simulations with uniform lithosphere thickness of 60, 80, 100 and 150 km, and constant temperature in the asthenosphere

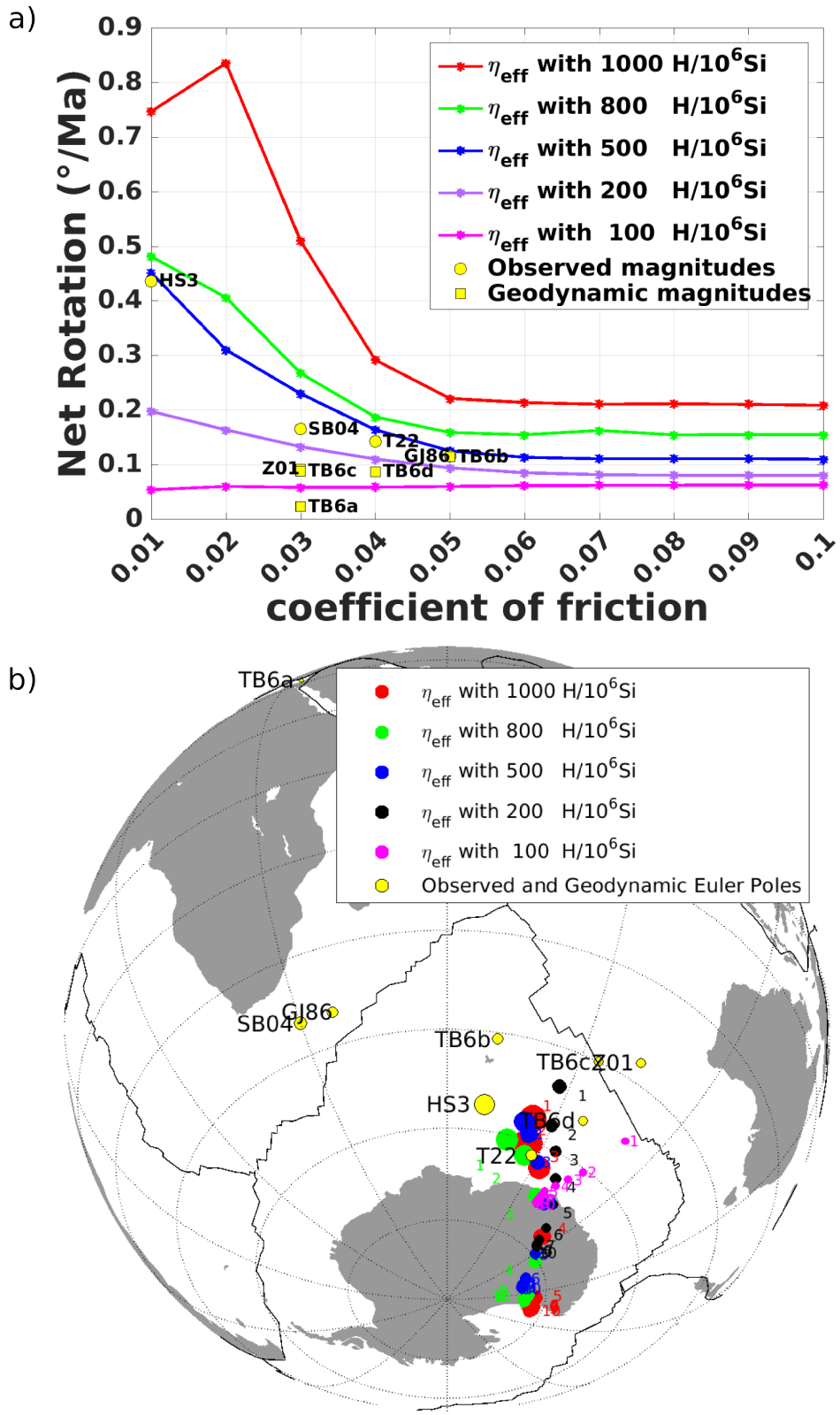

FIGURE 3.15: a) Predicted net rotation (NR) for a varied water content in the asthenosphere compared with observation-based estimates and previous numerical predictions (as in Figure 3.12) and b) corresponding Euler pole locations with an increasing plate boundary yield stress.

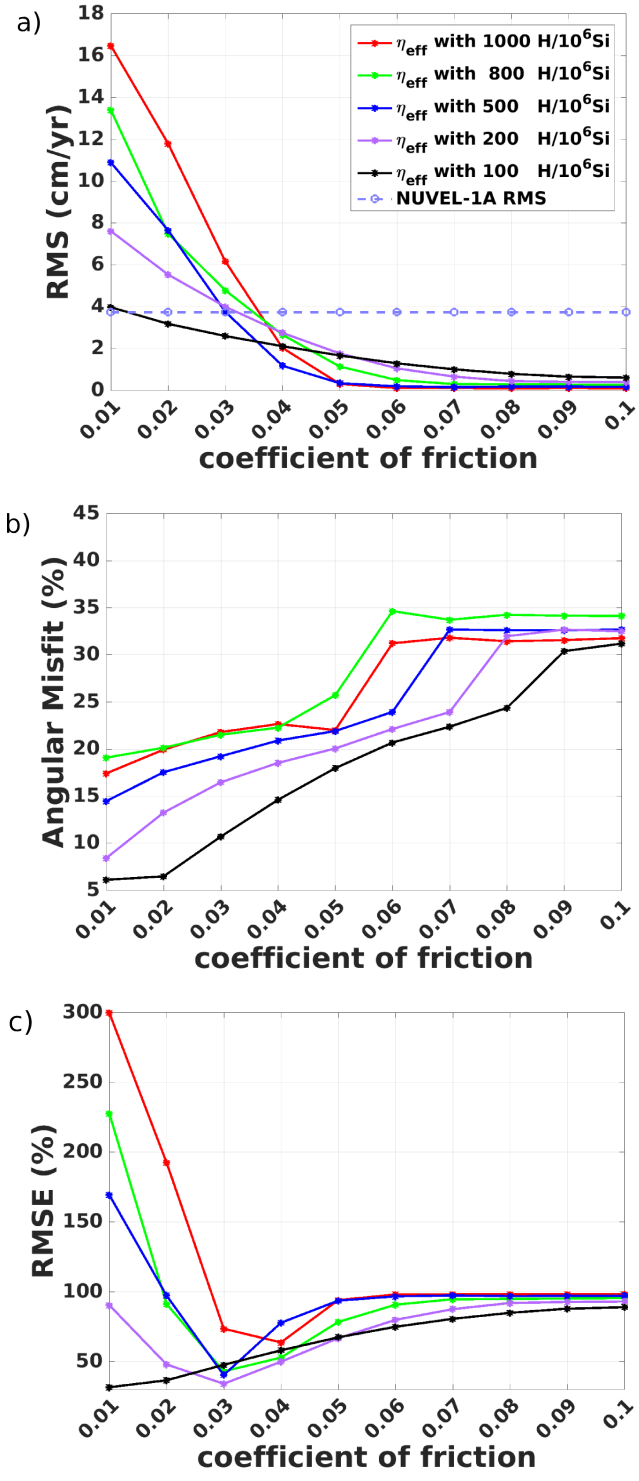

FIGURE 3.16: Estimates of a) global root mean square (RMS) of predicted plate motion with LVVs for varying water content in the asthenosphere for different coefficients of friction compared to the observed rms of NNR-NUVEL-1A (DeMets et al., 2010) b) global angular misfits. c) Show the root mean square error (RMSE) for the velocity magnitude in percentage.

high water content in the asthenosphere is found to decrease the viscosity and in turn causes lithospheric plates to move faster, which also gives larger amplitudes of lithosphere net rotation. This finding on the nature of the lithospheric plate showing dual behavior of strong interior and weak boundaries confirms previous studies for example Moresi and Solomatov (1998), who showed the rheological properties of the Earth that are necessary for plate tectonics to initiate, that is the presence of a weakening mechanism of the lithosphere is required a for breaking it. This weakening is suggested here to continue, even after breaking, to sustain the continuous relative motion of the individual plates. For example, the aseismic creep behavior of the San Andreas Fault due to the weak lithospheric rock as sampled from the seismogenic zone (Carpenter et al., 2011) compared to surrounding rocks away further in the plate interior also explains the horizontal maximum compressive stress in northeast direction, which is perpendicular to the Fault zone (Zoback et al., 1987).

Chapter 4

Results on lithosphere stress field and topography

In this chapter, I present the second part of the results. The refined lithosphere and mantle rheological parameters from the estimates of plate motion are used to predict lithospheric stress field and dynamic topography that are compared with observations. This is in attempt to also constrain the thermal and density structures of the upper mantle. I do this by experimenting with different thermal and density structures of the upper mantle to achieve a good fit with observations.

4.1 Contributions to crustal stress from above and below 300 km

I start by examining the separate contributions of the mantle flow above 300 km (Shallow Earth setup) and below (i.e. deeper forces) to the global lithospheric stress field and topography. To calculate the contribution of the lower domain, I use a constant lithosphere thickness (100 km) and density (3.27 kg/m^3), radial viscosity distribution and a seismic velocity-to-density scaling (Figure 2.1a-b) below a 300 km depth according to (Steinberger and Calderwood, 2006) and 3D density structure below 300 km depth derived from the seismic tomography model Smean (Becker and Boschi, 2002) as used in the case of plate motion estimates. The resulting maximum horizontal magnitude (SH_{max}) and direction of the lithospheric stress field are shown in Figure 4.1(a) and the the corresponding dynamic topography in Figure 4.1(c). I obtained compressional regimes in regions of past and present subduction. On the North and South American continents, beneath which the ancient Farallon and Nazca plates respectively were subducted, compressive stress magnitudes reach about 40 MPa. In the far east, downwelling

flows stretching north to south from the northwestern Pacific through Australia towards Antarctica, correspond to a compressional stress regime with magnitudes ranging between ~50 and 80 MPa. These opposite compressional regions are connected through the Arctic and the Antarctic and engulf two distinct regions with extensional stress regimes centered on the Pacific and African superswell regions. The predicted SH_{max} directions in Figure 4.1(a) generally follow the first-order lithospheric stress pattern (Zoback 1992), similar to previous mantle flow predictions of the lithospheric stresses (Steinberger et al., 2001; Lithgow-Bertelloni and Guynn, 2004; Ghosh and Holt, 2012). In the largest extensional regions such as found in the Pacific (superswell) and above deep upwellings across southeastern Africa, stresses reach magnitudes around 30 MPa. With the maximum compressional stress along the western Pacific subduction region around 65 MPa.

To investigate the contribution of the upper domain (300 km) on the stress field, I calculate the SH_{max} magnitude and direction using thermal density heterogeneity model TM1 (Figure 2.2a) combined with the CRUST 1.0 model and disregard mantle density variations below 300 km. Comparison of the lithosphere stress (SH_{max}) predictions due to mantle flow driven by density anomalies below 300km (Figure 4.1a) to that due to structure in the upper 300 km (Figure 4.1b), reveals notable differences in the model-based stress regimes, magnitudes and directions in continental regions. If stresses are generated by the upper domain only, then almost all continental regions are are characterized by extensional regime, with the largest stress magnitudes found in areas of high topography and orogenic belts, such as the Tibet and Andes highlands. These mostly blue continents in Figure 4.1(b) shows that the stress field observed in nature in continental regions have their origin probably beyond the depths of the crust and the lithosphere. Our stress predictions from the shallow Earth setup with laterally varying crustal and lithospheric densities in Figure 4.1(b) show stress magnitudes and pattern similar to Naliboff et al. (2012). However, as opposed to the results of Naliboff et al. (2012) we predict high compressional magnitude at continental margins, which may in part originate from the finer treatment of the crust and the temperature-dependent creep viscosity. Also the high compressional stresses along the subduction margins in Figure 4.1(b) are likely induced by slabs models included in our setup.

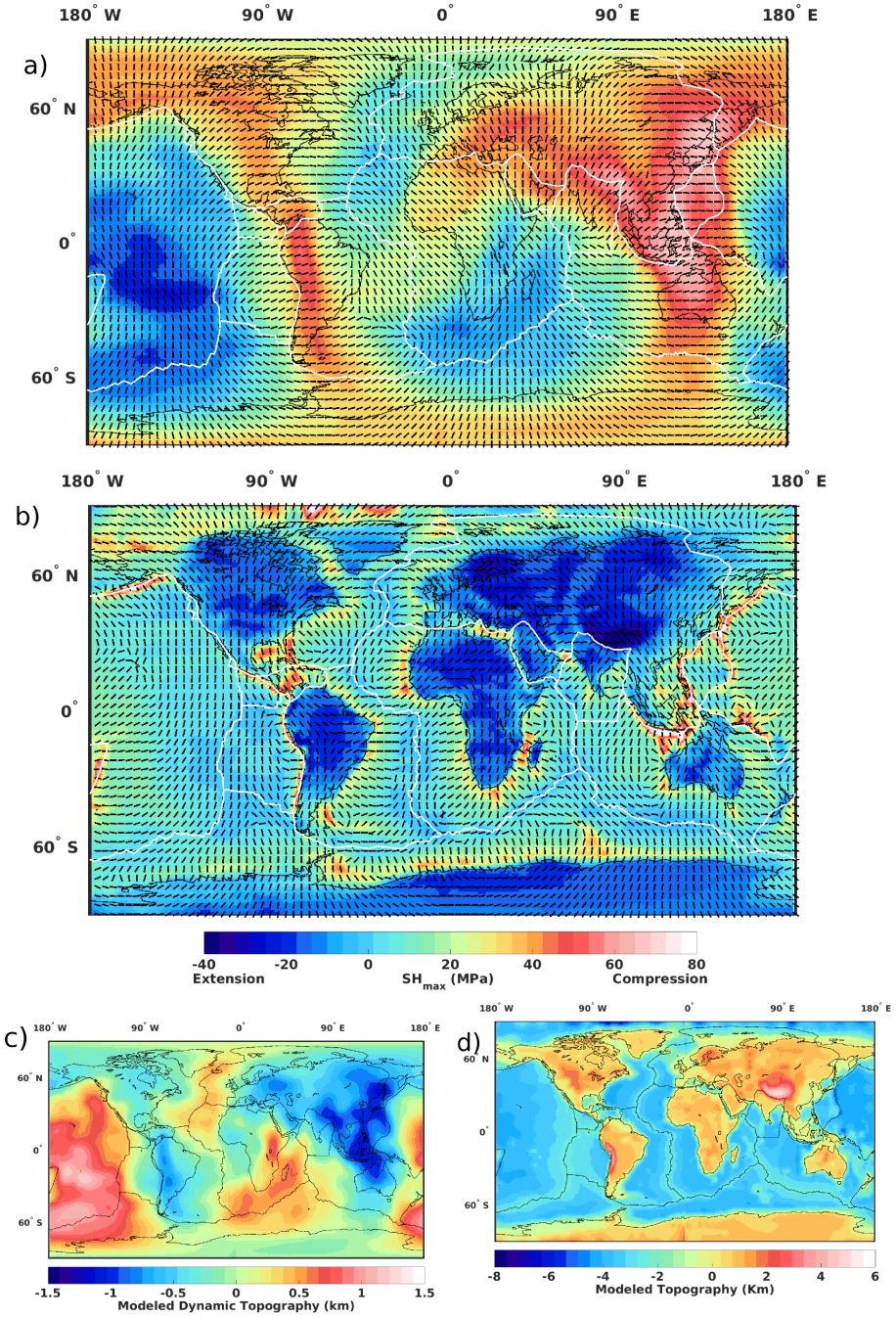

FIGURE 4.1: (a) Model-based maximum horizontal stress magnitude and most compressive stress directions [SH_{max}] following the convention with compression being positive originating from the mantle flow driven by density anomalies below 300 km.This is due to the tractions in Figure 3.5, inducing stresses in the assumed lithosphere thickness of 100 km, which get smoothed out over large distances. (b) Similarly, model-bases stresses based on the structure of the top integrated and hence 300 km of the upper mantle, computed with the CRUST 1.0 model and TM1. (c) and (d) depict the corresponding modelled topography beneath air (free surface). Excluding the contribution of the deep mantle seems to give a world mostly extensional in all continents different from what is observed.

4.2 Total lithospheric stresses and topography

Next I compute the combined effect of both the lower mantle buoyancy and the upper mantle heterogeneities on the global SH_{max} magnitude and direction for comparison with the separate contributions discussed above and with observations. Note that this is not a linear superposition of the separate contributions, because changing the properties of the upper 300 km also changes the topography and stress caused by density anomalies below 300 km depth. The resulting SH_{max} direction and magnitude (Figure 4.2a) due to the combined contributions of the upper and lower mantle show a compressional regimes in areas similar to Figure 4.2(a), muting almost all the strong extensional stresses predicted in continents shown in Figure 4.1(b). Also, the predicted SH_{max} orientation generally follows the first-order lithospheric stress pattern (Zoback, 1992), similar to predictions based on only density anomalies below 300 km depth (Figure 4.1a), with some regional deviations. The dominance of the contribution from below 300 km to the lithospheric stress field orientation can be seen from the similarities in the SH_{max} direction between Figure 4.1(a) and Figure 4.2(a), and the dissimilarities with Figure 4.1(b), especially in continents. Nevertheless, the contribution from the upper 300 km to the predicted stress magnitude is evident in areas with large crustal thickness in continents, such as Tibet and the Andes. The regions where an extensional regime is predicted with only the contribution from below 300 km (Figure 4.1a) correspond very well with extensional stress regions in the combined model (Figure 4.2a).

The result is not very different, when instead I use the thermal density model TM2 for the total lithospheric stress field prediction. Both the predicted SH_{max} magnitude and direction with TM1 (Figure 4.2a) and TM2 (Figure 4.1b) show notable similarities in oceans and continents, owing to the strong contributions from below 300 km which are similar for both models. They show relatively high compressional stress magnitudes in subduction or convergence regions such as the Mediterranean, south of the Tibetan Plateau, south of Alaska, and the northwest Pacific extending through the Sumatra subduction zone and underneath the Australia and Antarctic plates. However, the SH_{max} compressional signal underneath North America in Figure 4.2(a) is muted and that of the South American region is turned into an extensional regime along the Andes (Figure 4.2) with the inclusion of the mantle above heterogeneities 300 km and the crust. Similar to the Figure 4.1(a) both predictions with TM1 and TM2 (Figure 4.2a and Figure 4.2b) show SH_{max} extensional regimes corresponding to regions of upwellings and/or volcanism. However, the model with TM2 generates a much higher extensional

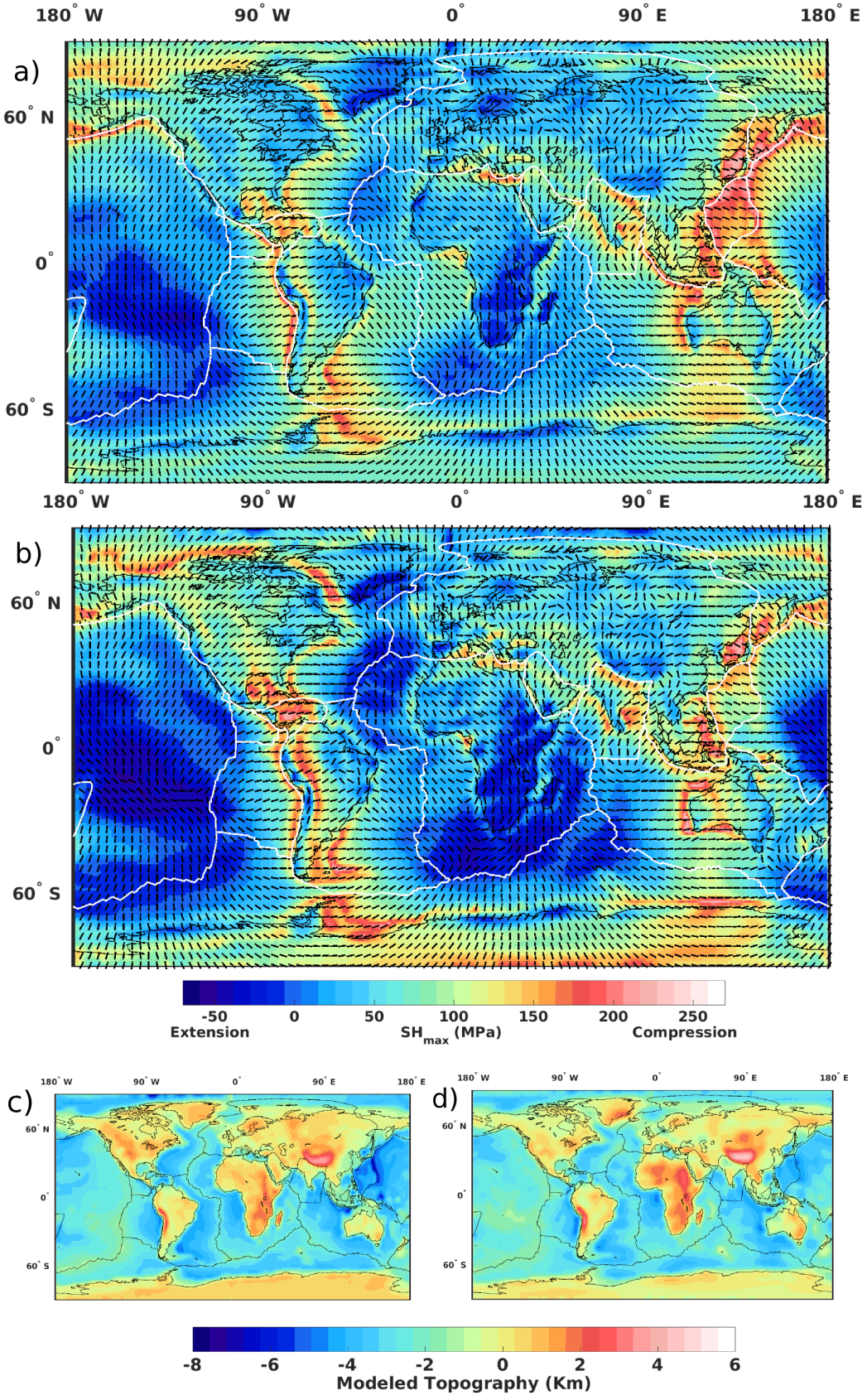

FIGURE 4.2: SH_{max} magnitude and direction predictions from combined contributions due to lower mantle flow and upper mantle from a) TM1 with crust model and b) TM2 with crust model. Corresponding model topography is shown in c) and d) respectively.

magnitude ~ 60 MPa in the North Atlantic region around Iceland, and around the Azores and Canary hotspots, compared to TM1. Stress magnitudes are more alike in the Southern Pacific Rise and around southern Africa. Differences are in part due to the detailed and well resolved upper mantle structures in the S-wave model used to derived TM2 (Schaeffer and Lebedev, 2013), whereas in TM1 the upper mantle structure is based on sea floor age in oceanic regions (Müller et al., 2008) and the slab temperatures based on (Steinberger, 2000). In regions where the coverage of heat flow data is sparse (e.g. in South America and Antarctica) (Artemieva, 2006; Pollack et al., 1993), TM2 (Figure 4.1b) may give better results. In South America TM2 predicts the compressional signal along the subducting Nazca plate and under Antarctica where the compressional stresses are induced by the downwelling flow computed with TM2. In these regions there is barely any heat flow data.

4.3 Lithospheric stress and topography without crustal effect

Following above prediction of lithospheric stress field and topography (section 4.1.2), I repeated the two simulations, but this time without crustal thickness variations to compute the SH_{max} and topography (Figure 4.3). The resulting stress magnitude and orientation from TM1 (Figure 4.3c) and TM2 (Figure 4.3d) without the crustal contribution are quite similar to the respective previous results shown in Figure 4.2 that include crustal contribution. Here, the resulting topography with TM1 (Figure 4.3a) and TM2 (Figure 4.3b) show similar amplitude due to the sea floor cooling and thickening along the ridges in the Atlantic, Indian and Pacific Ocean peaking above ~1.5 km. With TM1, which explicitly contains subducted slabs, narrow, deep trenches are computed above subduction zones, such as in the northwestern Pacific and at the west coast of South America. Also the negative topography in the Sumatra plate boundary is reproduced well with TM1 model reaching a value ~1.8 km. Based on tomography (model TM2) the computed topographic lows are wider and less prominent.

Predicted topography with TM2 is higher in Eastern African (2 to 2.5 km), and highly elevated regions are more extended. Figure 4.3(a) with TM1 (based on sea floor age) shows relatively low topography amplitude in the northwest of the Pacific plate around Hawaii and towards the Mariana trench compared to Figure 4.3(b) with TM2 (based on s-wave model SL2013sv) corresponding to a mean regional temperature difference about ~ 200°C between TM1 and TM2

(Figure **??**a-b). The topography with TM2 almost predicts all island chains associated with hotspots in and around the Africa plate, in the Pacific and along the Atlantic opening. In the North Atlantic, the positive topography (Icelandic swell) due to the Iceland plume-lithosphere interaction (Rogozhina et al., 2016; Schiffer and Nielsen, 2016) is more pronounced in Figure 4.3(b) with TM2 based on Schaeffer and Lebedev (2013) tomography with heights exceeding 2 km compared to Figure 4.3(a) with TM1 based on Müller et al. (2008) ocean floor ages, showing a bit less than ~2 km. The high topographic amplitude along the mid-ocean ridges (MORs) as a result of high temperatures beneath these spreading centers where new sea floor is created, is generally more pronounced in the TM2 model topography than with TM1. Despite the striking differences in topographic amplitude between Figure 4.3(a) and Figure 4.3(b) in oceans along the MORs, modelled stress orientations (Figure 4.3c-d) are very similar in these regions.

Also, the predicted strong negative topography (Figure 4.3a-b) in continental regions such as North America, Eurasia, Western Africa, South American, and western Australia are mostly due to the old depleted mantle lithosphere in cratons (King, 2005). This results from, the low temperatures in thermal model TM2 (Figure 4.3b), due to the conversion from seismic models to temperature and density, under the assumption that all seismic velocity anomalies are due to thermal variations only. This produces unrealistically strong density anomalies and, hence large negative topography at cratons (Forte and Perry, 2000), if correction due to the chemical depletion in the mantle lithosphere is not considered. Cammarano et al. (2011) showed that correction for the depletion of the lithosphere increases temperature of cratonic root by about 100 K but decreases density by about 0.1 gcm^{-3} and fits observations well compared to models assuming pyrolitic composition. Hence I adopt two thermal structures from different seismic tomography models SAW24B16 (Mégnin and Romanowicz, 2000) and S20RTS (Ritsema et al., 2011) with corrections applied to the depleted mantle to estimate lithosphere stress field and topography (Figure 4.4b-c) and compare to stress field and topography from TM2 with 100 K additional temperature converted to density in crations to account for chemical deplection. I give detail description on the resulting dynamic topography (SAW, S20 and TM2+100 K) in section 4.5. Also the large negative topography amplitude in cratons observed in topography with TM2 compared to TM1 does not readily translate to similar large variations in the respective predicted SH_{max} orientation (Figure 4.3c-d), showing that cratonic roots have less influence on the lithospheric stress field (Naliboff et al., 2012).

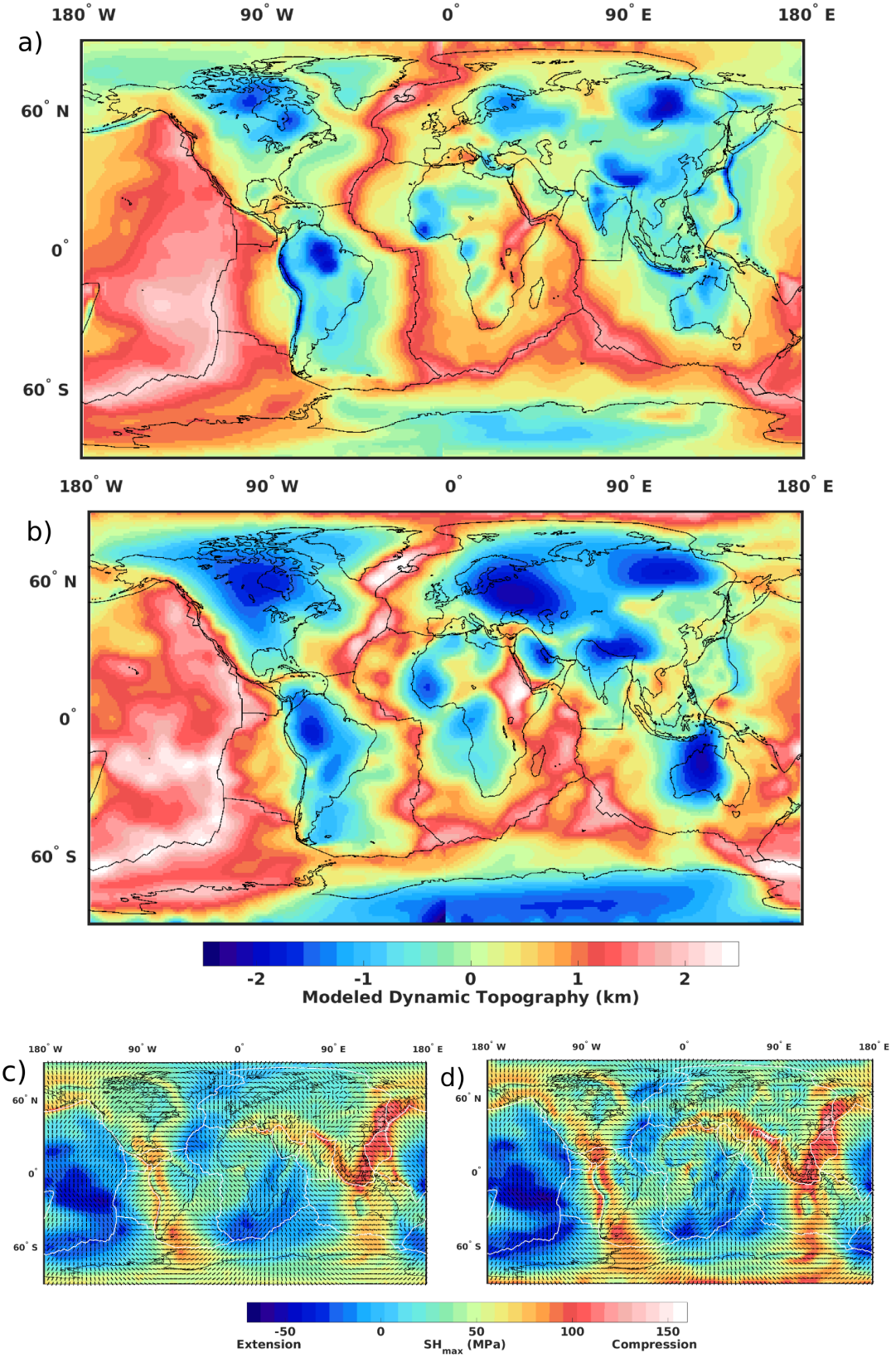

FIGURE 4.3: (a) Modelled topography using upper mantle structure TM1 and (b) modelled topography using TM2 and corresponding SH_{max} prediction with (c) TM1 and (d) TM2. In contrast to Figure 4.2, the effect of the crust is not included here.

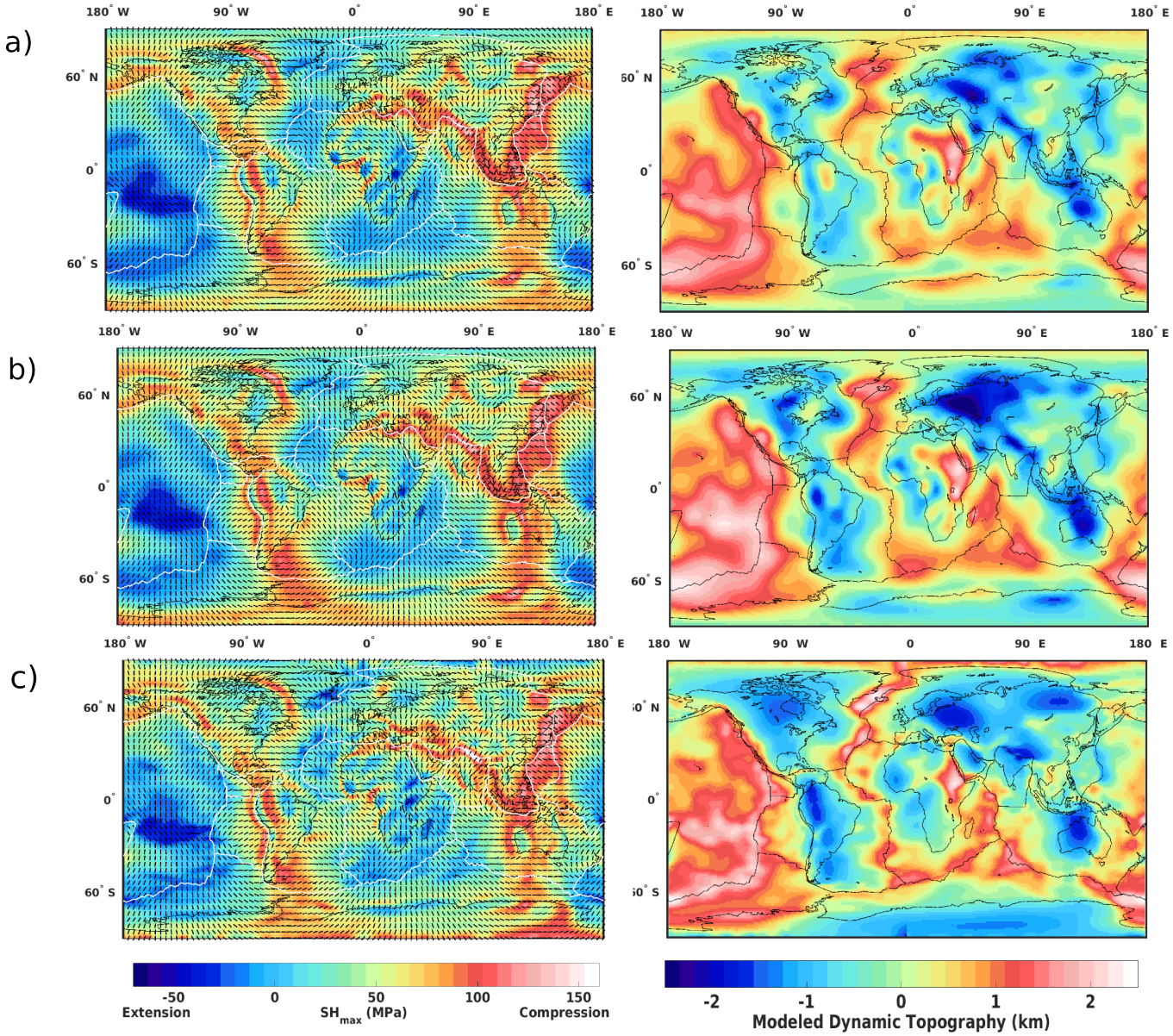

FIGURE 4.4: (left column) modelled lithospheric stress field without the effect of crustal thickness variations and (right column) corresponding topography for (a) TM2 (100 K additional temperature converted to density in crations to account for chemical deplection), (b) SAW24B16 with realistic treatment of cratons using $Perple_X$ after Cammarano et al. (2011) and same with (c) S20RTS for the upper mantle thermal and density structures.

4.4 modelled versus observed lithospheric stress field

I compare the predicted SH_{max} orientation to the current observed stress data. Following the stress interpolation method presented by Müller et al. (2003), I use their Fixed Search Radius (FSR) method which uses a global weighting defined by a fixed Eucludian distance for the stress data interpolation and stress quality. The smoothed stress field orientation at a grid point is based on the dominant stress data orientation within the selected radius. For a detailed explanation on the FSR method see Müller et al. (2003). Stress data with quality A, B, and C with unknown stress regime were considered. Since I do not consider the respective regime in the quantitative analysis, I also included the stress data with unknown style having quality A and B in our smoothing procedure to make our smooth field more robust. I smooth the observed SH_{max} orientation of the World Stress Map 2016 (Heidbach et al., 2016), with a search radius of 270 km (Figure 4.5a-b) on a grid interval of 2.5°x2.5°. The background dot colors in the smoothed map represent the stress data regimes with red denoting normal fault, blue as thrust fault, green as strike-slip fault and black as unknown regime. For the interpolation I only took into account the orientation pattern of the stress data. I limit the comparison with modelled lithospheric stress orientation to areas with enough data for the interpolation. The new WSM2016 has relatively good coverage in some regions that were not well covered in the previous version (Heidbach et al., 2008) like Brazil, parts of North America, Eastern Russia, and Central Africa. I regard it as appropriate to compare the modelled stress orientation with the smoothed observed stress data and regard deviations of actual stress from smoothed stresses as second-order pattern.

In figure 8(c) I superimposed the total modelled stress fields with TM1 in thin bars plotted on TM2 in thick bars, showing the different regimes. There is fairly good agreement in the predicted stress orientation and regime at long wavelength between TM1 and TM2. The regional variations shown in the stress pattern and regime in Figure 4.5(c) are mainly due to density contrasts in the lithosphere or just below, which are nearly isostatically compensated or cause lithosphere flexure, and due to topography (Zoback, 1992; Zoback and Mooney, 2003; Bird et al., 2006). Compared to the observed SH_{max} pattern and regime (Figure 4.5a and Figure 4.5b) I predict similar style in regions such as Eastern African and Tibet with normal faulting comparable to earlier works, which considered the effect of the whole mantle with a lithosphere and crustal model (Lithgow-Bertelloni and Guynn, 2004; Ghosh and Holt, 2012; Ghosh et al., 2013; Wang et al., 2015). I predict normal faulting mostly in regions above upwellings (mostly extensional

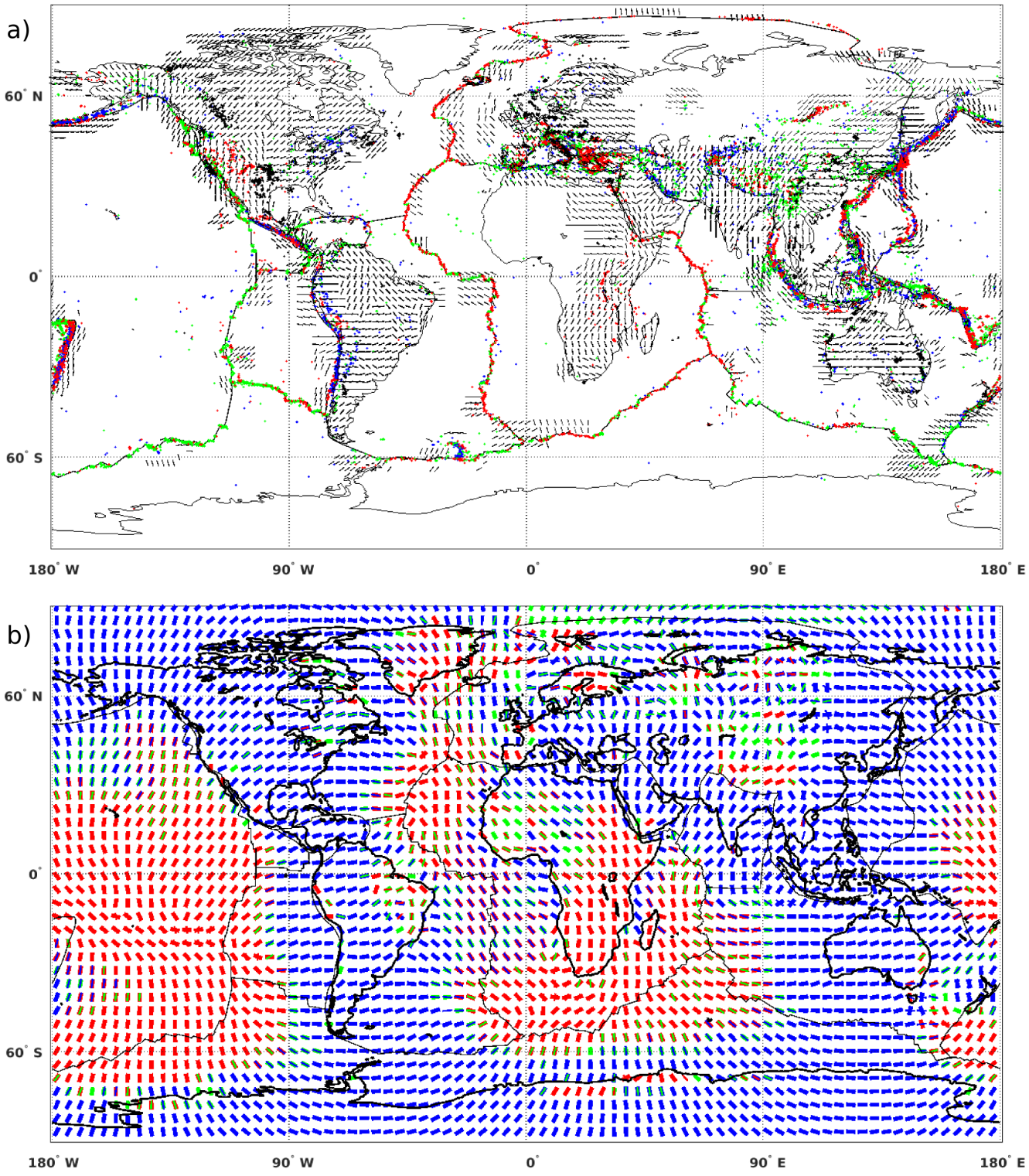

FIGURE 4.5: (a) interpolated World Stress Map World stress map 2016 (Heidbach et al., 2016) data on a grid of 2.5°x2.5°, using only stress orientation with a constant search radius 270 km, and (c) predicted SH_{max} orientation and regime from total stress contribution with TM1 (plotted in thin bars) over TM2 (thick bars) upper mantle thermal structure. Colors of dots in (a) and bars in (b) indicate observed or predicted stress regime with red for normal faults or tensile stress, blue for thrust faults or compressive stress, and green for strike-slip faults or intermediate stress (one principal horizontal stress positive, one negative

regions) such as the Icelandic swell, Eastern Africa rift, or along divergent plate boundaries while thrust faults are mainly predicted in compressional regions like subductions zones and tectonically active regions in continents. In continental areas, few regional variations are shown in South America, West Africa and on the Eurasian cratons. In oceans I see variations in the North Atlantic around the Icelandic swell, at the east Pacific Rise and around the southern African plate region.

4.4.1 Misfit between WSM2016 and modelled lithosphere stress

To further evaluate the influence of each thermal structure I performed quantitative comparison between modelled and smoothed observed stress orientations. The estimated angular misfit (Figure 4.6) is a measure of the minimum angle between the modelled lithospheric stress orientation (Figure 4.5c for TM1 and TM2) and smoothed observed stress orientation (Figure 4.5a), which ranges between 0° to 90°. Here, angular misfit lower than 22.5° is regarded as a good agreement between modelled and observed WSM2016 data, with values above 67.5° regarded as poor fit. The general SSW to NNE stress orientation observed over the North American plate matches the model predictions with either of the two thermal structures TM1 and TM2. The angular misfit map over North America from both thermal structures show a poor fit over Yellowstone and Rocky Mountains extending to the Great Plains (Ghosh et al., 2013). The observed localized NW to SE stress direction deviates (Figure 4.5a) from the predicted long-wavelength stress pattern (Ghosh et al., 2013; Humphreys and Coblentz, 2007). Even though the thermal model TM2 has high-density cratonic roots, compared to TM1, their respective estimate of angular misfit shows that the North America cratonic root has limited influence on the stress field. The two density structures TM1 and TM2 yielded a mean value of 22.2° (std = 19.6°) and 22.9° (std = 20.7°) respectively. Similar angular misfits over the North America continent (Figure 4.9a-c) are obtained even with correction applied to the depleted mantle. As the upper mantle thermal structure TM1 for the South American continent is not well-constrained, due to lack of heat flow data in continental Brazil, the predicted stress field gives a relatively poor fit, with mean misfit 37.73° (std =20.24°). However, TM2 did not perform much better with a mean misfit 33.79° (std = 21.9°). Both stress field models failed to match the observed stress field in the Andes, due to the dominant localized N-S orientation predicted, caused mainly by high topography and large crustal thickness (compare to Figure 4.3c-d). In the Africa continent, predicted N-S stress orientations along the Eastern Africa Rift from either model

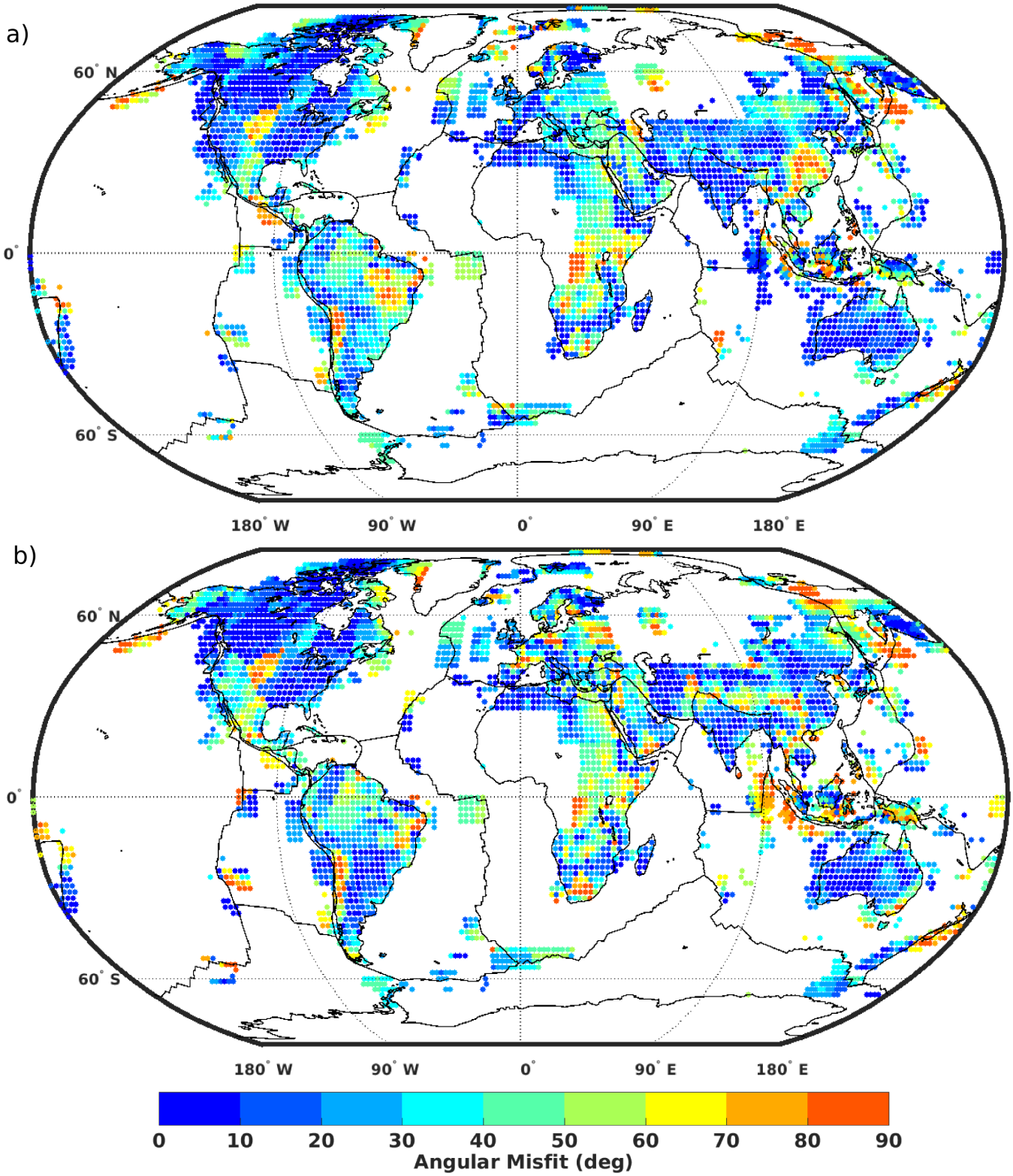

FIGURE 4.6: Angular misfit between the observed (WSM 2016) and total modelled stress direction with (a) TM1 and (b) TM2 upper mantle thermal and density structures.

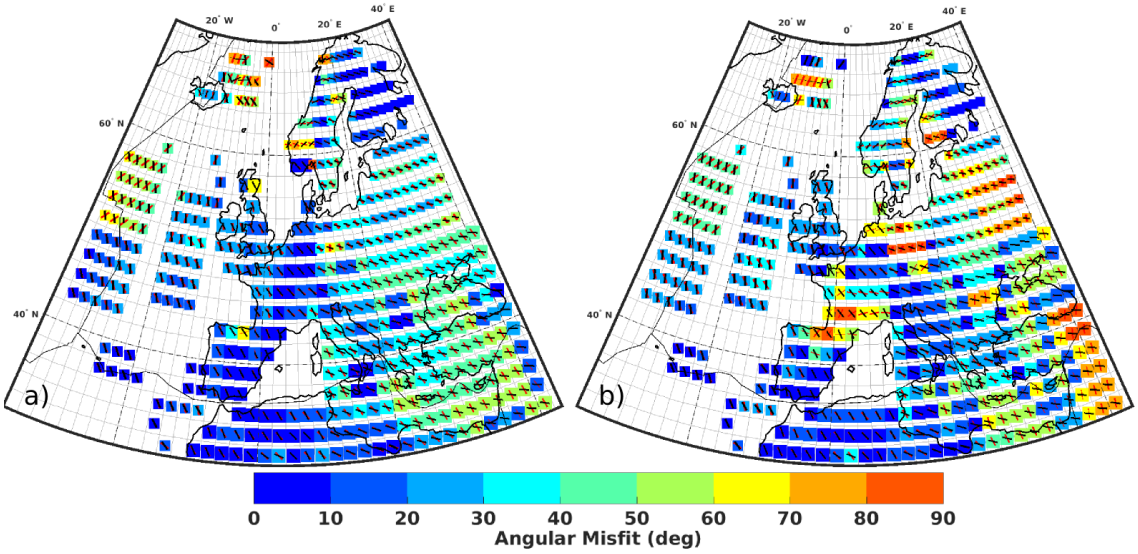

FIGURE 4.7: Angular misfit in Europe between the observed stress and modelled total stress with (a) TM1 and (b) TM2. Red bars denote modelled orientations and black bars the smoothed observed stress field (WSM2016).

match the observed stress quite well with TM1 fitting much better compared to TM2, but both fail over the Congo craton and South African plateau.

4.4.2 Western Europe

Contributions to the stress field in Western Europe come from the North Atlantic ridge (NAR) push in the west and possibly the far-field slab pull from the north-western Pacific subduction zones. In the south, forces come from the convergence of the Africa and Eurasia plates, with Africa subducting under Eurasia in the Mediterranean (Zoback, 1992; Müller et al., 1992; Gólke, 1996; Heidbach and Höhne, 2007; Schiffer and Nielsen, 2016). These plate boundary forces combined with the anomalous mantle pressure (Schiffer and Nielsen, 2016) underneath the North Atlantic lithosphere generate the dominant first-order NW-SE stress pattern. I almost match the NW-SE stress orientation with TM1 (Figure 4.7a), while TM2 (Figure 4.7b) shows deviations from this NW-SE pattern. It gives a second-order stress pattern in some regions, such as in Poland, Hungary, Romania, Turkey, Russia and France.

These regional pattern deviations are mainly due to the upper mantle density structure and topography (Heidbach and Höhne, 2007) (compare to Figure 4.1a). The large volume of heat flow data (Pollack et al., 1993; Artemieva, 2006) in continental Western Europe (TM1) improves the fit to the observed stress field compared to the s-wave based thermal structure (TM2) yielding mean misfit values of 18.30° (std = 22.67°) and 19.9° (std = 22.64°) respectively. None of our models, was

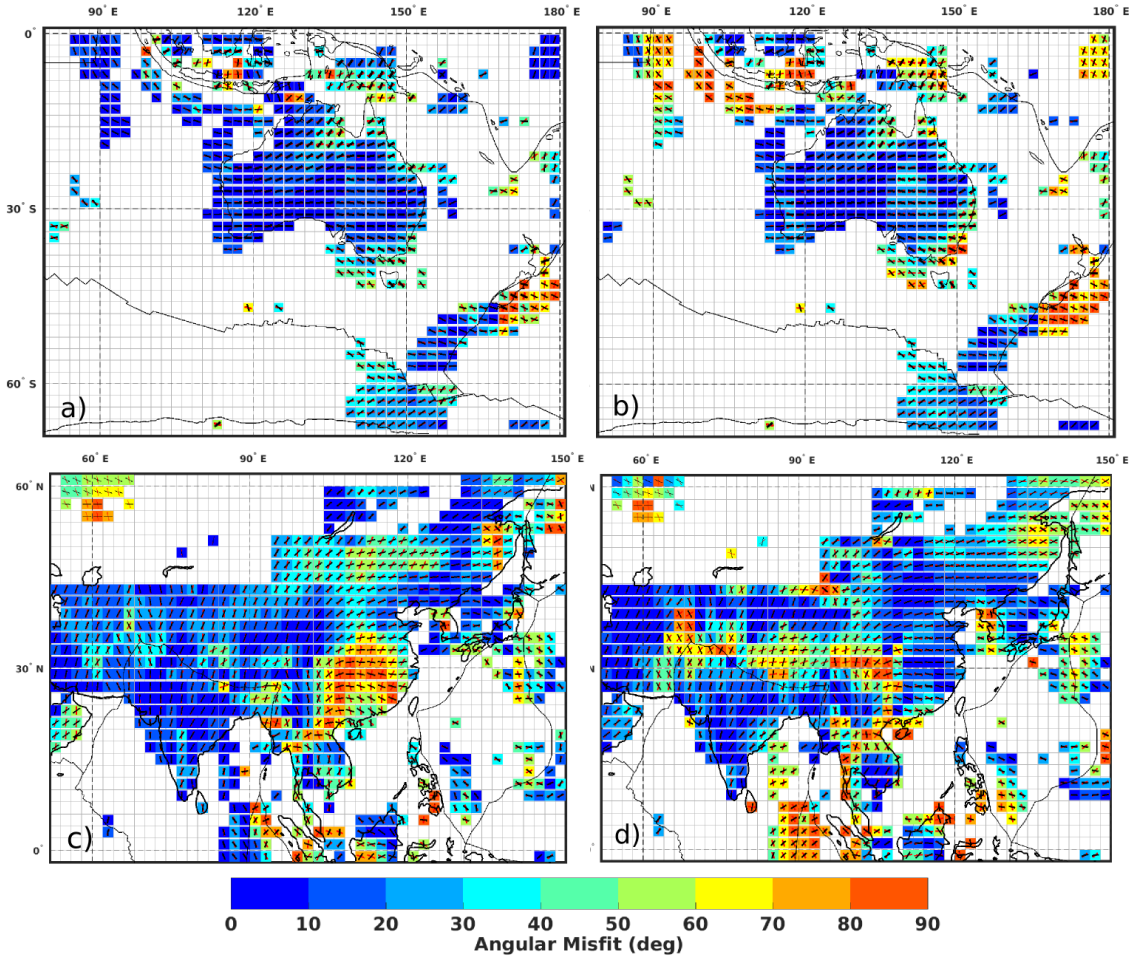

FIGURE 4.8: Angular misfit in Australia (a and b) and in and around Tibet (c and d) between observed stress and modelled total stress with (a and c) TM1 and (b and d) TM2 upper mantle structure. Red bars denote modelled orientations and black the observed stress field (WSM2016)

TABLE 4.1: Regional estimates of Mean Angular Misfit and Standard Deviation for modelled and observed stress field WSM2016 (Heidbach et al., 2016).

Continents	Mean Angular Misfits TM1	Standard Deviation	Mean Angular Misfits TM2	Standard Deviation
North America	22.20	19.60	22.90	20.70
South America	37.73	20.24	33.79	21.90
Europe	18.30	22.67	19.90	22.64
Africa	26.56	21.78	28.90	22.70
Australia	23.07	19.40	32.70	24.22
Tibet-China	28.00	23.00	29.10	24.87

able to predict the E-W stress orientation in the Aegean-Anatolian region coming from the ongoing subduction slab rollback (Heidbach and Höhne, 2007; Heidbach, 2003), giving angular misfit greater than 40° (Figure 4.7a and (Figure 4.3b). Table 4.1 shows summary of the estimates of angular misfit and standard deviations between modelled and observed stresses for the different regions.

4.4.3 Tibet and surrounding regions and Australia

The Australian continent has a similarly large amount of heat flow data. Hence the predicted intra-plate stress pattern with TM1 results in a somewhat lower angular misfit (Figure 4.8a) with mean value 23.07° (std = 19.4°) than with TM2 (Figure 4.8b) (mean = 32.7° and std = 24.22/$circ$). It has been argued that the stress pattern in Australia is mainly due to plate boundary forces (Reynolds et al., 2002), but I show here that crustal and sub-lithospheric heterogeneities have a certain degree of influence based on the lithospheric and crustal structure used. Nonetheless the W-E stress direction in the western provinces and NE-SW direction in the northern fits either model quite well. The remaining similarities between the predicted lithospheric stress fields (TM1 and TM2) rather go to support earlier findings that Australian interplate stresses has about 80 % contribution from plate boundary forces. The orientation of the stress pattern deviates from the absolute plate velocity direction at almost 90° in the entire plate. The collision of India and Eurasia forming the Himalayas results in complex crustal and lithospheric deformation (van Hinsbergen et al., 2011; Gaina et al., 2015) giving a NE-SW compressional stress parallel to the direction of Indian plate velocity. The SH_{max} predictions with TM1 (Figure 4.8c) fit the stress pattern better over the Tibet Plateau with mean value of 28° (std = 23°) compared to TM2, where a predicted E-W direction results in misfit ~50° misfit (Figure 4.8d). Both models performed relatively badly in part of China, when compared to the observed stress field.

4.5 Comparing dynamic topography with TM1 and TM2 to observed residual topography.

Here, I compare the modelled dynamic topography to two independent observation-based residual topography fields (Hoggard et al., 2016; Steinberger, 2016). Residual topography gives a convenient way to constrain both isostatic and non-isostatic contributions to the modelled dynamic topography (Crough, 1978; Gurnis et al.,

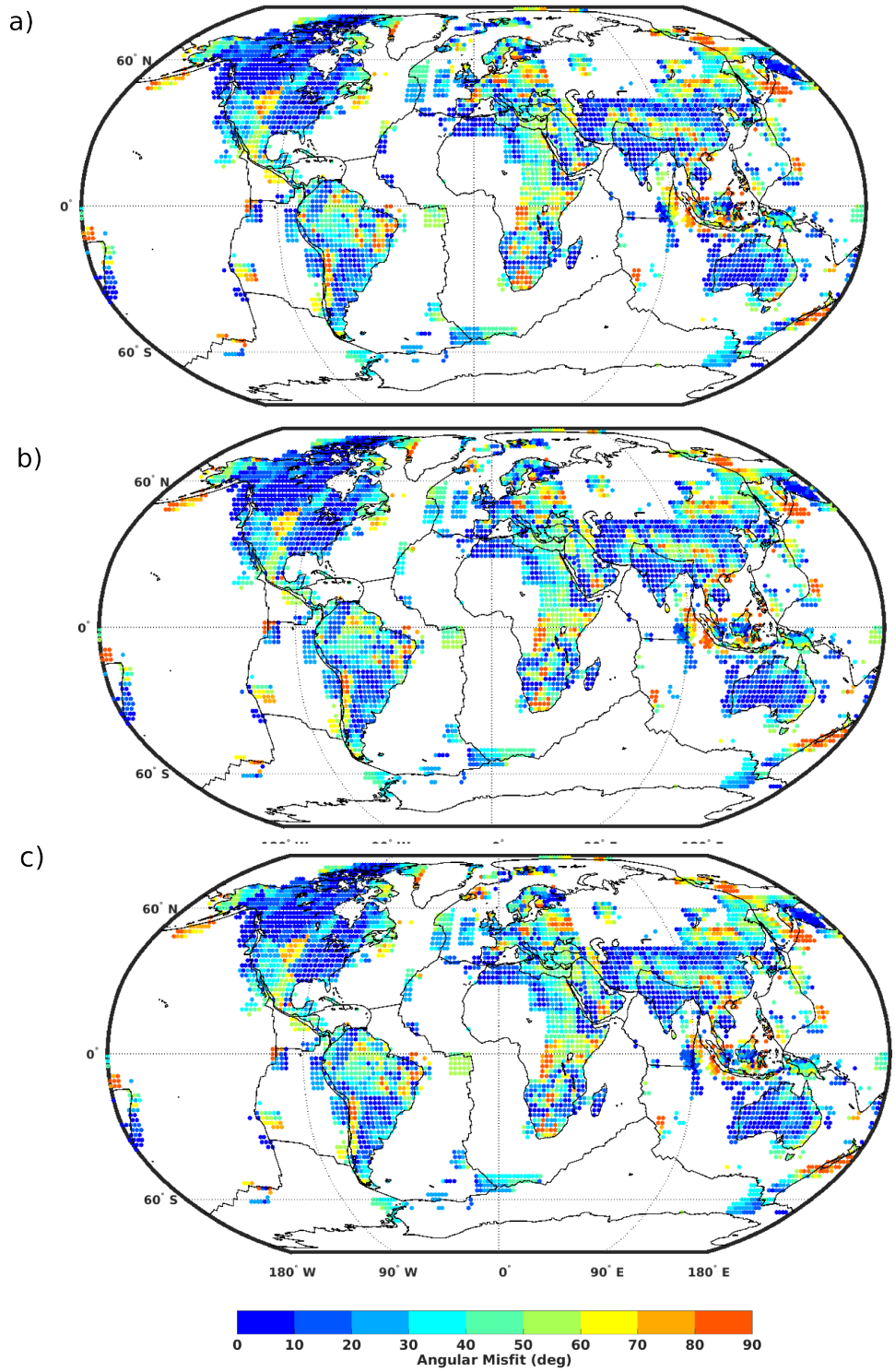

FIGURE 4.9: Angular misfit between the observed (WSM 2016) and total modelled stress direction with (a) TM2 with cratonic regions having added constant temperature of 100 K and (b) SAW24B16 with realistic treatment of cratonS using Perple$_X$ after Cammarano et al. (2011) and same with (c) S20RTS for the upper mantle thermal and density structures.

2000; Wheeler and White, 2000; Becker et al., 2014; Heidbach et al., 2016; Steinberger, 2016). This is done with the assumption that if topography is perfectly compensated isostaically within the upper mantle at depths of range 100 - 150 km, the integral of density with depth, as a function of crustal thickness and density to Moho depth and of sea flooor age will be same everywhere for the chosen depth. The observed model by Hoggard et al. (2016) is based on ocean seismic survey (in-situ) in oceanic regions and free-air gravity anomaly data in continents (Figure 4.10a), while the Steinberger (2016) residual topography model (Figure 4.10b) is derived with the CRUST 1.0 model (Laske et al., 2013). These two models are comparable in most oceanic regions, but give large mismatches in continents, which may be due to the different continental density structures used for either model. For example, subducting the plate under South America leads to a negative anomaly in Figure 4.10(b) but in the same region there is a positive anomaly in Figure 4.10(a) due to the free-air gravity data used on continents. Hence, I perform a regional quantitative comparison for oceans and continents separately. To compare the modelled dynamic topography using TM1 and TM2 (Figure 4.3a and 4.3b) to the observed fields (Figure 4.10a and 4.10b), I first remove the height due to ocean floor cooling. This is done by subtracting from the modelled dynamic topography the heights estimate from sea floor age (Müller et al., 2008), using the relation $H_{topo} = 3300m \cdot (1 - \sqrt{\frac{age}{100Ma}})$. Here I assumed half-space cooling for the sea floor with age. For a smooth transition of topographic height from ocean to continent, avoiding large jumps I nominally assumed 200 Ma lithosphere age for continents following the approach of Steinberger (2016). The resulting modelled dynamic topography fields (Figure 4.10c and 4.10d) with the effect of sea floor cooling with age removed, with locations of active hotspots volcanism plotted as green-black dots, shows how either model is able to predict the positive topographic amplitude due to (upwellings) plume heads pushing the lithospheric base.

Qualitative comparison of the two observed residual topography fields to the modelled topography shows some features are well reproduced with both TM1 and TM2 models. Among them are, the Pacific Swell, Hawaiian plume track, while the Canary Island plume, and heights around South Eastern Africa are much better reproduced with the TM2 dynamic topography. Removing height due to ocean floor age resulted in zero to negative topographic amplitudes along MORs in the Atlantic and Indian Oceans for the TM1 dynamic topography (Figure 4.10c) giving a correlation of 0.323 and 0.198 (Table 4.2) in oceans to Steinberger (2016) (S2016) and Steinberger (2016) (H2016) respectively. This model uses thermal density structure derived from ocean floor age,in the upper 300 km

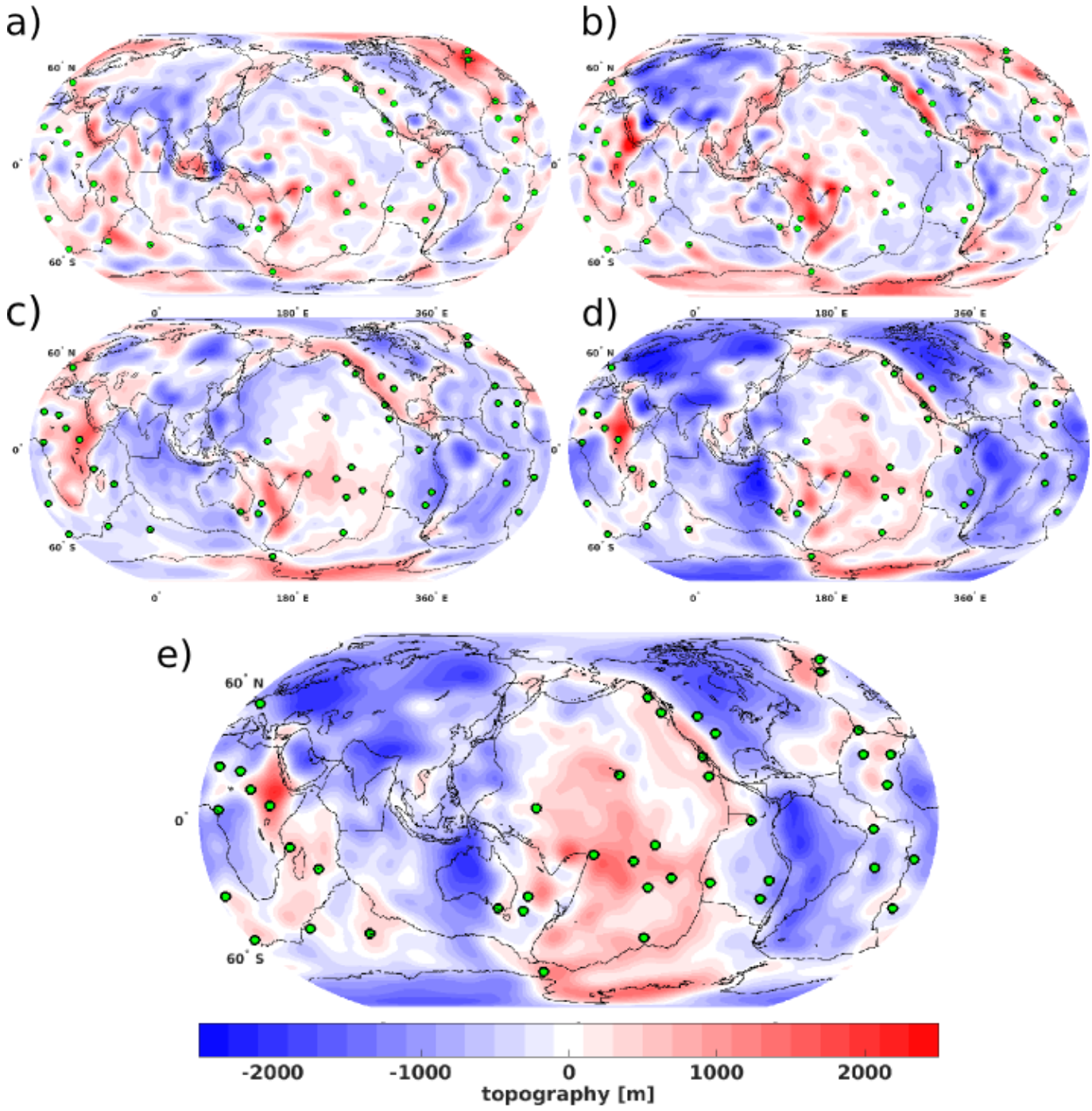

FIGURE 4.10: Comparing a) In-situ observed residual topography from Hoggard et al. (2016), and b) CRUST 1.0 -based residual topography from Steinberger (2016) with modelled dynamic topography using (c) TM1 and (d) TM2 upper mantle thermal density structures with the effect due to sea floor cooling with age removed. (e) Similar modelled dynamic topography using TM2 upper mantle thermal density structures with constant temperature (100 K) added in cratons. Green dots with black circle around shows locations of major hotspots

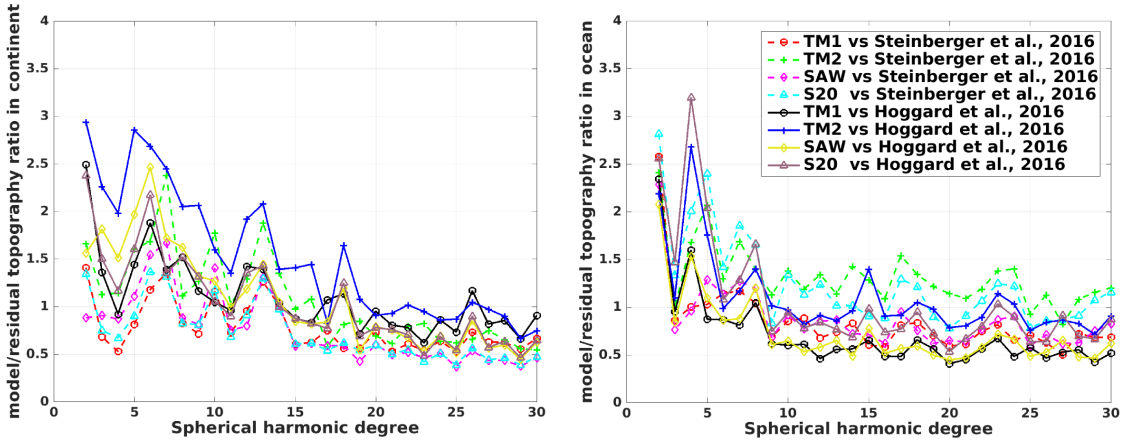

FIGURE 4.11: Ratio of residual (left-Steinberger (2016)) and (right - Hoggard et al. (2016)) with dynamic topography from TM1 and TM2 for ocean and continental regions.

hence when this contribution is removed, only the lower mantle contribution remains. In contrast, the TM2 model still gives small scale topography anomalies due to density anomalies other than from sea floor cooling at depths above (300 km) which are resolved in the seismic model used to derived TM2 giving relatively higher correlation of 0.348 and 0.284 to S2016 and H2016 respectively in oceans.

In continents, the TM1 model (Figure 4.10c) is quite similar to the residual models (Figure 4.10b) with correlation of 0.481 and ratio of 0.98 (Figure 4.11a) up to spherical harmonic degree 30. Over North America, Eurasia, and Australia it also fits the observed stress field better than TM2 (Figure 4.6). TM2 gives similar ratio and correlation, but at degrees lower than 15, the TM2 modelled topography is about twice the amplitude of TM1 (Figure 4.11a). Over the African continent with far less heat flow data used to derive TM1, the thermal density structure gives a large continent uplift to about 2 km, similar to part of Antarctica (Figure 4.10c). In Figure 4.10(d), this uplift is less extended, better showing negative topography at the Congo craton, but reaches a height above 2 km over the East African swell similar to S2016 (Figure 4.10b). Many of the remaining continental regions, however, show large negative topographic magnitudes of more than -2 km, resulting from the compositional effect in cratons in e.g. Eurasia, Australia and North America being unaccounted for. To assess the robustness of the studies I introduce two other upper mantle thermal density structures derived from SAW24B16 (Mégnin and Romanowicz, 2000) and S20RTS (Ritsema et al., 2011) seismic tomography models as a qualitative check for our TM2 model. For the seismic velocity anomalies from SAW24B16 (SAW) and S20RTS (S20) the method of Cammarano et al. (2011), is used to convert seismic tomography models to

TABLE 4.2: Correlation between modelled dynamic topography and observed residual topography models (Steinberger, 2016; Hoggard et al., 2016) for continents and oceans.

Modelled topography	Steinberger, 2016		Hoggard, 2016	
Upper mantle Thermal density	*Ocean*	*Continent*	*Ocean*	*Continent*
1. TM1	0.323	0.481	0.198	0.169
2. TM2	0.348	0.498	0.284	0.171
3. TM2 + 100 K $(in\,craton)$	0.370	0.512	0.284	0.180
4. S20RTS (S20)	0.442	0.653	0.221	0.232
5. SAW24B16 (SAW)	0.248	0.718	0.287	0.188

temperature structures taking into account chemical depletion in cratonic areas. In contrast, for TM2, I assumed additional 100 K converted to a negative density as compositional contribution in cratons as opposed to the more realistic treatment of compositional effects as done for SAW and S20. The modelled topography show improvements in cratonic regions but there is almost no change in the resulting lithospheric stress field (Figure 4.4). Correlation to S2016 increases 0.512 for TM2 (with assumed 100 K compositional effect) in continents. SAW and S20 gave much higher correlation 0.653 and 0.718 in continents (Table 4.2), which could be the results of realistic treatment of cratonic regions but also using different seismic tomography models. For example, Steinberger (2016) used a similarly simple procedure to convert a different combination of tomography models to density and still obtained a rather high correlation of 0.64 in continents.

The assumed compositional correction is not very large giving about 100 m reduction in the cratonic negative anomaly (Figure 4.10e) compared to the case without correction in continents(Figure 4.10d). This in part supports the proposed treatment of the upper mantle thermal density structure with a joint petrological and seismological constraint (Forte and Perry, 2000; Forte et al., 2010; Cammarano et al., 2011), which is outside the scope of our studies. The Hoggard et al. (2016) residual topography shows positive amplitude over the Eurasia craton due to the free-air gravity data used, while the other residual (Figure 4.10b) and all modelled dynamic topography models gave negative value, resulting in low correlation of H2016 on continents for all models. The correlations in oceans with H2016 found here is also lower. However, this result is model-dependent, as Steinberger et al. (2017) find an improved correlation with H2016 in oceans using a different density model.

4.6 Concluding Remarks

In this second part of the study, I have analyzed mantle contributions coming from shallow and deep dynamic processes to the stress field and topography. In this analysis the constraints on rheological parameters are used to predict plate velocity and dynamic geoid and test different thermal-density structures. The lithosphere stress field pattern is seen to originate more from deep sources compared to the corresponding dynamic topography. The fit of predicted dynamic topography to the observed field strongly depends on the choice of the upper mantle thermal-density structure, unlike the stress field. Compared to high crustal topography, large cratons seem to have little or no influence on predicted stress orientation. The integration of forces cause that the larger-scale contributions from the lower mantle overwhelm the smaller-scale contribution from close to the surface in stress predictions. These mantle tractions acting on the lithosphere are transmitted elastically over far distances through the lithosphere whereas the influence of regional scale small convection and isostatic effects are much more dominating in topography features. The disparity of the origin of topography and lithosphere stress field contributions shown here in this study gives a new window into understanding these geophysical observables. In Figure 4.1b and d), I show this phenomenon where modelled stress especially in continents does not fit observations well but topography from the combination continental crustal-lithosphere thicknesses and sea floor age variation seems to match the observed topography much better. The current debate on degree two topography (Steinberger et al., 2017) seems to complement this finding on the deep mantle contribution to the stress field. Hence, adjustment of compositional structures in the lower mantle and its apparent influence on the fit between modelled and observed stress field should be a research topic for a follow-up to this study.

Chapter 5

Summary and Conclusion

This research contributes to the state-of-the-art knowledge of the mantle and lithosphere dynamics and their interaction and quantifies their influence on surface processes. This interaction is assessed by constraining parameters that influence both the lithosphere and mantle dynamics. I have started by linking present-day global plate velocities to plastic yielding at plate boundaries and the presence of laterally varying viscosity (LVV) underlying the lithosphere plates due to the deep cratonic roots, strong subducting slabs, and cooling of oceanic plates. From the results presented here, it is evident that frictional deformation at plate boundaries influences both the magnitude and orientation of plate velocities. To match the observed plate motions in a no-net rotation reference frame, the required frictional coefficient for plate boundary yield stress should be less than 0.04 and asthenospheric viscosity $\sim 5 \cdot 10^{19}$ Pas, similar to frictional parameters used to initiate and sustain subduction zones in previous studies (Becker and Faccenna, 2009; Hall et al., 2003; Hassani et al., 1997; Sobolev and Babeyko, 2005; Tan et al., 2012). High values of frictional coefficient $\mu > 0.1$, as suggested by observations (Zhong and Watts, 2013) and experiments (Byerlee, 1978), lead to an almost stagnant lid instead of moving lithosphere plates, as was also found by Crameri and Tackley (2015). Numerical models that used high coefficient of friction with pore fluid pressure (Gerya and Meilick, 2011) arrive at effective coefficients of friction μ <0.1, suggested by previous mantle convection numerical studies to be required for the initiation of plate tectonics (Crameri and Tackley, 2015; Moresi and Solomatov, 1998; Richards et al., 2001; Tackley, 2000). The present study also shows a good match between the modeled and observed plate motions for both magnitude and orientation with low inter-plate coefficient of friction $\mu\sim < 0.05$.

This also applies for lithospheric plate net rotation (NR) but here the coefficient of friction has limited influence on the NR amplitude compared to the Euler

pole location. For different frictional values with the same asthenosphere viscosity cutoff, the drift or change in Euler pole location is significant even with viscosity contrast that gives lower NR amplitudes. This was also shown with layered viscosity structure and plastic yielding at plate boundaries, which excites little to no net rotation of the lithosphere. NR amplitude is significantly influenced by LVVs coming from cratons (Zhong, 2001), with minimal effect from the plate boundary strain localization (coefficient of friction). I am able to match observation-based NR amplitudes in the range 0.1°/Ma to 0.2°/Ma (Doubrovine et al., 2012; Gordon and Jurdy, 1986; Steinberger et al., 2004; Torsvik et al., 2010; Wang and Wang, 2001) with $\mu < 0.05$ and asthenosphere minimum viscosity cutoff 10^{19} Pas to $5{\cdot}10^{19}$ Pas. For low LVV cutoff and low coefficient of friction plates moves fast when a thinner lithosphere (60 and 80 km) is imposed as compared to the setup with a thicker lithosphere (100 and 150 km), but in a similar direction because in these cases slab pull can more effectively drive plate motion. With larger lithosphere-asthenosphere viscosity contrast of ~2 orders of magnitude and low friction coefficient $\mu < 0.04$ I am able to predict NR amplitude close to observations (SB04, HS3, GJ86)(Steinberger et al., 2004; Wang and Wang, 2001; Gordon and Jurdy, 1986) and some previous numerical studies (Alisic et al., 2012; Conrad and Behn, 2010; Gérault et al., 2012; Stadler et al., 2010), while with $\mu > 0.04$ I obtain too low NR amplitudes. The preferred NR magnitude 0.10°/Ma with Euler pole location 49.31° S and 74.88° E was obtained a with minimum viscosity cutoff of $5{\cdot}10^{19}$Pas and $\mu = 0.02$, which also give plate velocity prediction that fits the observed plate motion in No-Net-Rotation reference frame. Almost all the numerical models that were able to obtain a large value close to observations include plastic yielding (Alisic et al., 2012; Stadler et al., 2010) at plate boundaries instead of weak zone/viscosity drop with free surface. The driving forces causing lithospheric plates to move also contribute to topography and lithosphere stress field.

The second part of this study focuses on predicting the influence of density heterogenities on lithospheric stress field and topography. With this approach, I further refined the set of rheological parameters and density structure giving a better fit to the observed plate motions by matching the modeled lithospheric stress field and topography to observations. Here I have focused on distinguishing the dynamic contributions of density heterogeneities coming from the shallow (upper mantle - above 300 km depth) thermal-density anomalies with/without the crust on the present-day lithospheric stress state and dynamic topography in the presence of a lower mantle flow contribution (below 300 km). I

have considered different density structures above 300 km to estimate the associated uncertainty and its effect on dynamic topography and stress. The numerical method allows us to separate out the lithosphere-asthenosphere dynamic contributions to the lithospheric stress field from other contributions coming from the lower mantle flow and to distinguish the spatial pattern coming from either of these counterparts of the Earth interior, as well as their combined contribution. Thereby, I evaluate the dominant contributions to lithosphere stress field and dynamic topography. Here I use the same lower mantle flow model as has been used for predicting plate motion and dynamic geoid in Chapter 3. This model is either use alone or in combination with different thermal density structures of the upper mantle to calculate the lithosphere stress field and topography.

Although there are some significant regional variations in the modeled stress field orientation with thermal structure of the heat-flow based and the S-wave derived thermal structure (Figure 4.3c-d or Figure 4.3a-b), mostly in continental Eurasia, South America and parts of Africa, the corresponding modeled dynamic topography (Figure 4.3a and 4.3b) shows much more variation in both continental and oceanic regions. This delineates the signals contributing to each observable (i.e. topography and stress field), suggesting that a larger portion of the force contribution to the lithospheric stress field signal originates from lower mantle flow (Steinberger et al., 2001; Lithgow-Bertelloni and Guynn, 2004) similar to the plate motion contribution - no lower mantle contribution (No LM drive) Figure 3.8-, while the dynamic topography is much more influenced by the upper mantle density structure (Marquart and Schmeling, 1989; van Wijk et al., 2010; Becker et al., 2014; Faccenna et al., 2014). The upper mantle above 300 km accommodates numerous geological processes that influence both topography and stresses at short to medium wavelengths, while the lower mantle contributes the longer-wavelength signal (Braun, 2010). Crustal thickening, shallow lithospheric structures, subducting slabs, plume heads at the base of the lithosphere and small-scale mantle convection occurring in the upper mantle (Marquart and Schmeling, 1989; Lowry et al., 2000; Lithgow-Bertelloni and Guynn, 2004; Hoggard et al., 2016) all contribute to topography at different degrees but with limited influence on the modeled lithospheric stress field.

Furthermore, the negative topographic amplitudes in cratons are much larger in the Thermal structure of the S-wave-based (TM2) induced dynamic topography (Figure 4.3b and 4.10d) compared to that from the simulation using the Thermal structure of the heat-flow based (TM1) (Figure 4.3a and 4.10c) but the computed lithospheric stress field is similar for TM1 and TM2 both in cratons and

other continental regions, for example under the Tibetan-Himalaya plateau (Figure 4.2a-b and 4.3c-d). This again suggests that density anomalies closer to the surface give a relatively larger contributions to topography compared to stresses. The negative topographic anomaly under Tibet which is obtained with both the thermal structure of the heat-flow based model and the seismic S-wave tomography based model is believed to be due to either the isostatic effect related to the lithosphere thickening during the mountain building, or subduction of the Indian plate, or both. In the seismic tomography, vertical slices show high-velocity anomalies for the Indian plate subducting in the south-northern direction under Eurasia at depths 200-250 km. A similar structure can be observed for the Anatolian-Aegean subduction (Faccenna et al., 2014) at depths above 410 km.

Nonetheless, the upper mantle density and crustal structures produce a dominating regional second-order pattern in some high altitude regions e.g. the Andes. General first-order pattern computed with a uniform lithosphere thickness from the mantle flow only shows a stress pattern comparable to earlier studies of the origin of stress, which is either attributed to tectonic forces which are also used to predict plate motion, or to the mantle flow alone (Zoback, 1992; Richardson, 1992; Steinberger et al., 2001; Reynolds et al., 2002; Lithgow-Bertelloni and Guynn, 2004; Bird et al., 2008; Ghosh et al., 2008; Ghosh et al., 2013). Thermal structures, the heat-flow based model and the seismic tomography based model differ with regards to their data source, spatial resolution and the extent to which each captures upper mantle heterogeneities. This causes difference in the modeled dynamic topography, whereas the predicted lithospheric stress fields are more similar, because stress filed (regime) is influenced to a greater extent by the lower mantle flow. This finding is further supported by the fact that the use of other upper mantle thermal-density structures derived from S-wave models S20RTS (Ritsema et al., 2007)(S20) and SAW24B16 (Mégnin and Romanowicz, 2000) (SAW) gives similar results. Hence, fitting both observables would require a consistent treatment of relative contributions from both the upper and lower mantle. The thermal structure model based on heat-flow data and sea floor age has low spatial coverage in many continental regions, as opposed to a relatively high resolving skill of the global surface wave tomography, on which the TM2 is based. For example, such areas as Brazil, western Africa, Eastern Russia, and parts of Canada are characterized by a limited data coverage in thermal structure of the heat-flow based model (Pollack et al., 1993; Artemieva, 2006). Likewise, seismic tomography models have some inherent drawbacks with regards to resolving structures close to the surface with sufficient detail. It is therefore clear

why the the seismic tomography based model model derived from a better resolved seismic tomography of Schaeffer and Lebedev (2013) performs better in the upper mantle compared to other seismic models (S20 and SAW) with regard to predicting dynamic topography (Steinberger, 2016).

In conclusion, this study confirms some findings suggested by previous numerical studies and also gives new insights into the lithosphere and mantle coupling and its influence on surface observables. In summary I show that:

- Modeled plate velocities are influenced by frictional deformation occurring at plate boundaries and the required coefficient of friction is lower than what has been proposed in some mantle convection studies and by observational studies. I conclude that to attain the required driving force for plate motions due to slab pull and slab suction, the inter-plate frictional force has to be low, $\mu\sim$ 0.02 to 0.04.

- The effect of frictional deformation is also seen to influence both NR amplitude and position of the Euler pole, with model predictions being able to match the observation-based NR amplitudes in the range 0.1°/Ma to 0.2°/Ma (Doubrovine et al., 2012; Gordon and Jurdy, 1986; Steinberger et al., 2004; Torsvik et al., 2010; Wang and Wang, 2001) using $\mu < 0.05$ and asthenosphere minimum viscosity cutoff 10^{19} Pas to $5{\cdot}10^{19}$ Pas.

- The advantage of considering variable lithosphere thickness over uniform thickness in mantle convection studies is shown by the wide range of velocity magnitudes obtained when using different lithosphere thickness. Thinner lithosphere plates (60 and 80 km) are found to move faster compared to thicker lithosphere plates (100 and 150 km). Model predictions with a 100-km thick lithosphere are most comparable with observations and model prediction with variable lithosphere thickness.

- Rheological parameters obtained by varying olivine water content in the asthernosphere imply that increasing the water content results in decreasing viscosity in the asthenosphere, thereby causing the overlying lithosphere plates to move faster. A decrease in asthenosphere viscosity also results in larger NR amplitudes, because the asthenosphere is more easily sheared, but has limited impact on the Euler pole location.

- Lateral density heterogeneities close to the surface (within 300 km) have a greater influence on topography than on lithospheric stress field which is mainly controlled by deep mantle flow. This is evident from the comparison of simulations utilizing heat-flow data based model and the seismic

tomography based model thermal structures that reveal large dissimilarities in the predicted dynamic topography but nearly identical lithosphere stress fields.

- This suggests that attention should be paid to the model input depending on which surface observable is investigated. For example, in cratonic regions I see large variations in the modeled topographic amplitudes but similar patterns of the stress field orientation when different upper mantle structures are used. Similar findings are obtained along mid-Ocean ridges.

- The crustal dominance in high altitude regions gives insights into the importance of variable crustal thickness and realistic material properties for both regional and global studies as shown by the $\sim 90^{\circ}$ change in modeled stress orientation in the Andes and Himalaya.

Chapter 6

Outlook

This study provides insights into lithosphere and mantle coupling and its influence on surface observables. Here the implementation of a more realistic upper and lower mantle rheological structures, is accompanied by a calibration of flow parameters with the aim of fitting the modeled geoid, plate velocities, dynamic topography and lithospheric stress field to observations. The mechanical sharing of the viscous asthenosphere due to overlying lithospheric plates generates anisotropy which can serve as a further constraint on mantle rheology. The direction of asthenospheric fabric deformation has been shown to correlate very well with the orientation of lattice preferred orientation (LPO) of olivine aggregates in the upper mantle (Nicolas and Christensen, 2013). Both radial and azimuthal anisotropy modes of seismic tomography models have been employed to constrain mantle viscosity structure with great success (Becker, 2006; Conrad et al., 2007; Conrad and Behn, 2010). Hence, further investigation of the complex upper mantle rheology with prediction of anisotropy and lithosphere net rotation is warranted to constrain the olivine water content in the asthenosphere .

Furthermore, the influence of plate boundary friction on plate velocity and subduction (**This study**; Crameri and Tackley, 2015; Tan et al., 2012; Sobolev and Babeyko, 2005) has been well established. Deformation sustained at plate boundaries due to plate tectonics has been studied using GPS observations to estimate strain-rate at plate boundaries (Kreemer et al., 2000) and documented in the literature. From an observational point of view, the Global Strain-rate Map shows variable distribution of strain-rate along plate boundaries. Future studies should quantify the impacts of varying plate boundary friction on both plate velocities and strain rate at plate boundaries with a much higher resolution. This will further help to constrain the modeled lithospheric stress field. Here, I have used a relatively coarse resolution with a 0.5 degree element size. It is therefore clear

that models with increased spatial resolution should provide more accurate predictions of the strain rate at plate boundaries.

This current research is restricted to the present day, but it is imperative to use these results as a starting point in past reconstructions of the surface fields analyzed in this study. Applying this study's realistic upper mantle rheology to predict surface processes of the immediate geologic past (i.e. Cenozoic period) will improve our current knowledge and will be of great importance to many exploration geophysical studies.

Lastly, this work has only accounted for the effects of LVVs in the upper mantle. However, it has been shown that lower mantle LVVs may have a strong influence on the modeled geoid (Kaban et al., 2007). Hence there is a need to revisit this present study using the model that implements LVVs in the lower mantle in order to quantify their impacts on the model results. This type of comparison between observations and model predictions could be useful too for evaluating alternative models of the mantle flow, such as different styles of thermochemical convection (e.g. LLSVPs in the mantle convecting separately or the recent BEAMS model (Ballmer et al., 2017).

Bibliography

Alisic, L., M. Gurnis, G. Stadler, C. Burstedde, and O. Ghattas (2012). "Multi-scale dynamics and rheology of mantle flow with plates". In: *J. Geophys. Res.* 117.B10402. DOI: 10.1029/2012JB009234.

Artemieva, I. (2006). "Global $1^\circ \times 1^\circ$ thermal model TC1 for the continental lithosphere: implications for lithosphere secular evolution". In: *Tectonophys.* 416, pp. 245–277.

Artyushkov, E. V. (1973). "Stresses in the lithosphere caused by crustal thickness inhomogeneities". In: *J. Geophys. Res.* 78, pp. 7675–7708.

Ballmer, M. D., C. Houser, J. W. Hernlund, and R. M. Wentzcovitch (2017). "Persistence of strong silica-enriched domains in the Earth's lower mantle." In: *Nature Geoscience* 10. DOI: 10.1038/ngeo2898.

Barrell, J. (1914). "The Strength of the Earth's Crust". In: *The Journal of Geology* 22.6, pp. 537–555. ISSN: 00221376, 15375269. DOI: 10.2307/30067883.

Becker, T. W. (2006). "On the effect of temperature and strain-rate dependent viscosity on global mantle flow, net rotation, and plate-driving forces". In: *Geophys. J. Int.* 167, pp. 943–957.

Becker, T. W. and L. Boschi (2002). "A comparison of tomographic and geodynamic mantle models". In: *Geochem., Geophys., Geosys.* 3.1. DOI: 10.1029/2001GC000168.

Becker, T. W. and C. Faccenna (2009). "A review of the role of subduction dynamics for regional and global plate motions". In: *Subduction Zone Geodynamics*. Ed. by F. Funiciello and S. Lallemand. Int. J. Earth Sci. Springer, pp. 3–34.

Becker, T. W. and R. J. O'Connell (2001). "Predicting plate velocities with geodynamic models". In: *Geochem., Geophys., Geosys.* 2.12. DOI: 10.1029/2001GC000171.

Becker, T. W., C. Faccenna, E. D. Humphreys, A. R. Lowry, and M. S. Miller (2014). "Static and dynamic support of western (U.S.) topography". In: *Earth Planet. Sci. Lett.* 402, pp. 234–246.

Becker, T. W., A. J. Schaeffer, S. Lebedev, and S. P. Conrad (2015). "Toward a generalized plate motion reference frame". In: *Geophys. Res. Lett.* 42, pp. 3188–3196. DOI: 10.1002/2015GL063695.

Bercovici D. Ricard, Y. and M. A. Richards (2000). "The Relation Between Mantle Dynamics and Plate Tectonics: A Primer". In: *The History and Dynamics of Global Plate Motions (eds M. A. Richards, R. G. Gordon and R. D. Van Der Hilst)* 121, pp. 5–46. DOI: 10.1029/GM121p0005.

Bird, P. (2003). "An updated digital model of plate boundaries". In: *Geochem., Geophys., Geosys.* 4.3, p. 1027. DOI: 10.1029/2001GC000252.

Bird, P. and Y. Li (1996). "Interpolation of principal stress directions by nonparametric statistics: global maps with confidence limits". In: *J. Geophys. Res.* 101, pp. 5435–5443.

Bird, P., Z. Ben-Avraham, G. Schubert, M. Andreoli, and G. Viola (2006). "Patterns of stress and strain rate in southern Africa". In: *J. Geophys. Res.* 111, pp. –. DOI: 10.1029/2005JB003882.

Bird, P., Z. Liu, and W. K. Rucker (2008). "Stresses that drive the plates from below: Definitions, computational path, model optimization, and error analysis". In: *J. Geophys. Res.* 113.B11406. DOI: 10.1029/2007JB005460.

Braun, J. (2010). "The many surface expressions of mantle dynamics". In: *Nature Geosc.* 3, pp. 825–833.

Brune, S., A. A. Popov, and S. V. Sobolev (2012). "Modeling suggests that oblique extension facilitates rifting and continental break-up". In: *Journal of Geophysical Research: Solid Earth* 117, B08402. DOI: 10.1029/2011JB008860.

Brune, S., S. E. Williams, N. P. Butterworth, and R. D. Müller (2016). "Abrupt plate accelerations shape rifted continental margins". In: *Nature* 5, pp. 201–204. DOI: 10.1038/nature18319.

Brune, Sascha, Christian Heine, Marta Pérez-Gussinyé, and Stephan V. Sobolev (2014). "Rift migration explains continental margin asymmetry and crustal hyper-extension". In: *Nature Communications* 5, p. 4014. DOI: 10.1038/ncomms5014.

Burov, E. B. (2011). "Rheology and strength of the lithosphere". In: *Marine and Petroleum Geology* 28, pp. 1402–1443.

Byerlee, J.D. (1978). "Friction of rock". In: *Pure Appl. Geophys.* 116, pp. 615–626.

Čadek, O. and L. Fleitout (2003). "Effect of lateral viscosity variations in the top 300 km of the mantle on the geoid and dynamic topography". In: *Geophys. J. Int.* 152, pp. 566–580.

Cammarano, F., P. Tackley, and L. Boschi (2011). "Seismic, petrological and geodynamical constraints on thermal and compositional structure of the upper mantle: global thermo-chemical models". In: *Geophys. J. Int.* 187, pp. 1301–1318.

Carpenter, B M, C Marone, and D M Saffer (2011). "Weakness of the San Andreas Fault revealed by samples from the active fault zone". In: *Nature Geoscience* 4,

p. 251. URL: http://dx.doi.org/10.1038/ngeo1089http://10.0.4.14/ngeo1089https://www.nature.com/articles/ngeo1089{\#}supplementary-information.

Conrad, C. P. and M. Behn (2010). "Constraints on Lithosphere Net Rotation and Asthenospheric Viscosity from Global Mantle Flow Models and Seismic Anisotropy". In: *Geochem., Geophys., Geosys.* 11.Q05W05. DOI: 10.1029/2009GC002970.

Conrad, C. P. and C. Lithgow-Bertelloni (2002). "How mantle slabs drive plate tectonics". In: *Science* 298, pp. 207–209.

— (2004). "The temporal evolution of plate driving forces: Importance of "slab suction" versus "slab pull" during the Cenozoic". In: *J. Geophys. Res.* 109. DOI: 10.1029/2004JB002991.

— (2006). "Influence of continental roots and asthenosphere on plate-mantle coupling". In: *Geophys. Res. Lett.* 33. DOI: 10.1029/2005GL02562.

Conrad, Clinton P., Mark D. Behn, and Paul G. Silver (2007). "Global mantle flow and the development of seismic anisotropy: Differences between the oceanic and continental upper mantle". In: *Journal of Geophysical Research: Solid Earth* 112.B7. B07317, n/a–n/a. ISSN: 2156-2202. DOI: 10.1029/2006JB004608. URL: http://dx.doi.org/10.1029/2006JB004608.

Crameri, F. and P. J. Tackley (2014). "Spontaneous development of arcuate single-sided subduction in global 3-D mantle convection models with a free surface". In: *Journal of Geophysical Research: Solid Earth* 119.7, pp. 5921–5942. ISSN: 2169-9356. DOI: 10.1002/2014JB010939.

— (2015). "Parameters controlling dynamically self-consistent plate tectonics and single-sided subduction in global models of mantle convection". In: *Journal of Geophysical Research: Solid Earth* 120 (5), pp. 3680–3706. DOI: 10.1002/2014JB011664.

Crough, S. T. (1978). "Thermal origin of mid-plate hot-spot swells". In: *Geophysical Journal of the Royal Astronomical Society* 55, pp. 451–469. DOI: 10.1111/j.1365-246X.1978.tb04282.x.

Dannberg, Juliane and Stephan V. Sobolev (2015). "Low-buoyancy thermochemical plumes resolve controversy of classical mantle plume concept". In: *Nature Communications* 6, p. 6960. DOI: 10.1038/ncomms7960.

Danyushevsky, L. V., S. M. Eggins, T. J. Falloon, and D. M. Christie (2000). "H_2O Abundance in Depleted to Moderately Enriched Mid-ocean Ridge Magmas; Part I: Incompatible Behaviour, Implications for Mantle Storage, and Origin of Regional Variations". In: *Journal of Petrology* 41.8, p. 1329. DOI: 10.1093/petrology/41.8.1329.

Davies, G. F. (1978). "The roles of boundary friction, basal shear stress and deep mantle convection in plate tectonics". In: *Geophysical Research Letters* 5.3, pp. 161–164. ISSN: 1944–8007. DOI: 10.1029/GL005i003p00161.

Davies, Geoffrey F. (1977). "Viscous mantle flow under moving lithospheric plates and under subduction zones". In: *Geophysical Journal International* 49.3, p. 557. DOI: 10.1111/j.1365-246X.1977.tb01303.x.

Davis, D. M. and S. C. Solomon (1985). "True polar wander and plate-driving forces". In: *Journal of Geophysical Research: Solid Earth* 90.B2, pp. 1837–1841. ISSN: 2156–2202. DOI: 10.1029/JB090iB02p01837.

DeMets, C., R. G. Gordon, and D. F. Argus (2010). "Geologically current plate motions". In: *Geophys. J. Int.* 181, pp. 1–80.

Doubrovine, P. V., B. Steinberger, and T. H. Torsvik (2012). "Absolute plate motions in a reference frame defined by moving hot spots in the Pacific, Atlantic, and Indian oceans". In: *J. Geophys. Res.* 117.B09101. DOI: 10.1029/2011JB009072.

Ebinger, C. J. and N. H. Sleep (1998). "Cenozoic magmatism throughout east Africa resulting from impact of a single plume". In: *Nature* 395, pp. 788–791.

Faccenda, M., T. V. Gerya, and L. Burlini (2009). "Deep slab hydration induced by bending-related variations in tectonic pressure". In: *Nature Geoscience* 2, pp. 790–793. ISSN: 11. DOI: 10.1038/ngeo656.

Faccenna, C., A. Heuret, F. Funiciello, S. Lallemand, and T. W. Becker (2007). "Predicting trench and plate motion from the dynamics of a strong slab". In: *Earth Planet. Sci. Lett.* 257, pp. 29–36.

Faccenna, C. et al. (2014). "Mantle dynamics in the Mediterranean". In: *Rev. Geophys.* 52, pp. 283–332.

Fischer, K. M., D. L. Ford H. A. Abt, and C. A. Rychert (2010). "The Lithosphere-Asthenosphere Boundary". In: *Ann. Rev. Earth Planet. Sci.* 38, pp. 551–575.

Flament N. Gurnis, M. and R. D Müllera (2012). "A review of observations and models of dynamic topography". In: *Lithosphere* 38, pp. 189–210. DOI: 10.1130/L245.1.

Forsyth, D. W. and S. Uyeda (1975). "On the relative importance of the driving forces of plate motion". In: *Geophys. J. R. Astr. Soc.* 43, pp. 163–200.

Forte, A. M. and J. X. Mitrovica (2001). "Deep-mantle high-viscosity flow and thermochemical structure inferred from seismic and geodynamic data". In: *Nature* 410, pp. 1049–1056. DOI: 10.1038/35074000.

Forte, A. M. and H. K. C. Perry (2000). "Geodynamic Evidence for a Chemically Depleted Continental Tectosphere". In: *Science* 290, pp. 1940–1944.

Forte, A. M., S. Quere, R. Moucha, N. A. Simmons, Stephen P., J. X. Grand S. P. Mitrovica, and David B. Rowley (2010). "Joint seismic–geodynamic-mineral physical modelling of African geodynamics: A reconciliation of deep-mantle convection with surface geophysical constraints". In: *EPSL* 295, pp. 329–341.

Froidevaux, C. and G. Schubert (1975). "Plate motion and structure of the continental asthenosphere: A realistic model of the upper mantle". In: *Journal of Geophysical Research* 80.17, pp. 2553–2564. ISSN: 2156–2202. DOI: 10.1029/JB080i017p02553.

Gaina, Carmen, Douwe J. J. van Hinsbergen, and Wim Spakman (2015). "Tectonic interactions between India and Arabia since the Jurassic reconstructed from marine geophysics, ophiolite geology, and seismic tomography". In: *Tectonics* 34.5, pp. 875–906. DOI: 10.1002/2014TC003780.

Garcia-Castellanos, D. and S. Cloetingh (2011). "Modeling the Interaction between Lithospheric and Surface Processes in Foreland Basins". In: *Tectonics of Sedimentary Basins*. John Wiley and Sons, Ltd, pp. 152–181. DOI: 10.1002/9781444347166.ch8.

Gérault, M., T. W. Becker, B. J. P. Kaus, C. Faccenna, L. N. Moresi, and L. Husson (2012). "The role of slabs and oceanic plate geometry for the net rotation of the lithosphere, trench motions, and slab return flow". In: *Geochem., Geophys., Geosys.* 13.Q04001. DOI: 10.1029/2011GC003934.

Gerya, T. V. and F. I. Meilick (2011). "Geodynamic regimes of subduction under an active margin: effects of rheological weakening by fluids and melts". In: *Journal of Metamorphic Geology* 29.1, pp. 7–31. ISSN: 1525-1314. DOI: 10.1111/j.1525-1314.2010.00904.x.

Ghosh, A. and W. E. Holt (2012). "Plate motions and stresses from global dynamic models". In: *Science* 335, pp. 839–843.

Ghosh, A., W. E. Holt, L. Wen, L. M. Flesch, and A. J. Haines (2008). "Joint modeling of lithosphere and mantle dynamics elucidating lithosphere-mantle coupling". In: *Geophys. Res. Lett.* 35.L16309. DOI: 10.1029/2008GL034365.

Ghosh, A., T. W. Becker, and E. D. Humphreys (2013). "Dynamics of the North American continent". In: *Geophys. J. Int.* 194, pp. 651–669.

Gólke, M. Coblentz D. (1996). "Origins of the European regional stress field". In: *Tectonophysics* 266, pp. 11–24. DOI: 10.1029/2011GC003934.

Gordon, R. G. and D. M. Jurdy (1986). "Cenozoic global plate motions". In: *J. Geophys. Res.* 91, pp. 12389–12406.

Green, D. H., W. O. Hibberson, I. Kovacs, and A. Rosenthal (2010). "Water and its influence on the lithosphere-asthenosphere boundary". In: *Nature* 467, pp. 448–451. DOI: 10.1038/nature09369.

Gripp, A. E. and R. G. Gordon (2002). "Young tracks of hotspots and current plate velocities". In: *Geophys. J. Int.* 150, pp. 321–361.

Gurnis, M., C. Hall, and L. Lavier (2004). "Evolving force balance during incipient subduction". In: *Geochem., Geophys., Geosys.* 5.7, Q07001. ISSN: 1525-2027. DOI: 10.1029/2003GC000681.

Gurnis, Michael, Jerry X. Mitrovica, Jeroen Ritsema, and Hendrik-Jan van Heijst (2000). "Constraining mantle density structure using geological evidence of surface uplift rates: The case of the African Superplume". In: *G3* 1. DOI: 10.1029/1999GC000035.

Hager, B. H. and R. J. O'Connell (1979). "Kinematic models of large-scale flow in the Earth's mantle". In: *J. Geophys. Res.* 84, pp. 1031–1048.

— (1981). "A simple global model of plate dynamics and mantle convection". In: *J. Geophys. Res.* 86, pp. 4843–4867.

Hager, B. H., R. W. Clayton, M. A. Richards, R. P. Comer, and A. M. Dziewoński (1985). "Lower mantle heterogeneity, dynamic topography and the geoid". In: *Nature* 313, pp. 541–545.

Hall, C. E., M. Gurnis, M. Sdrolias, L. L. Lavier, and R. D. Muller (2003). "Catastrophic initiation of subduction following forced convergence at transform boundaries". In: *Earth Planet. Sci. Lett.* 212, pp. 15–30.

Harper, J. F. (1975). "On the driving forces of plate tectonics". In: *Geophys. J. R. Astr. Soc.* 40, pp. 465–474.

Hassani, R., D. Jongmans, and J. Chéry (1997). "Study of plate deformation and stress in subduction processes using two-dimensional numerical models". In: *J. Geophys. Res.* 102, pp. 17951–17965.

Heidbach, O. and J. Höhne (2007). "CASMI—A visualization tool for the World Stress Map database". In: *Computers and Geosciences* 34, pp. 783–791.

Heidbach, O., M. Tingay, A. Barth, J. Reinecker, D. Kurfeß, and B. Müller (2008). *The World Stress Map database release 2008*. DOI: 10.1594/GFZ.WSM.Rel2008.

Heidbach, O., M. Rajabi, M. Ziegler, K. Reiter, and Wsm Team (2016). *The World Stress Map Database Release 2016 -Global Crustal Stress Pattern vs. Absolute Plate Motion*.

Heidbach, O. Drewes H. (2003). "3-D Finite Element model of major tectonic processes in the Eastern Mediterranean". In: *Geol. Soc. Lond. Spec.* 212, pp. 259–272.

Heine C. Müller, R. D. Steinberger B. Torsvik T. H. (2008). "Subsidence in intracontinental basins due to dynamic topography". In: *Physics of the Earth and Planetary Interiors* 171, pp. 252–264.

Hirth, G. and D. L. Kohlstedt (2004). "Rheology of the Upper Mantle and the Mantle Wedge: A View From the Experimentalists". In: *Inside the Subduction Factory*. Ed. by J. Eiler. Vol. 138. Geophys. Monograph. Washington DC: American Geophysical Union, pp. 83–105.

Hoggard, M. J., N. White, and D. Al-Attar (2016). "Global dynamic topography observations reveal limited influence of large-scale mantle flow". In: *Nat. Geosci.* 9, pp. 456–463. DOI: 10.1038/ngeo2709.

Huene, R. von and C. R. Ranero (2003). "Subduction erosion and basal friction along the sediment-starved convergent margin off Antofagasta, Chile". In: *Journal of Geophysical Research: Solid Earth* 108.B2. 2079, n/a–n/a. ISSN: 2156-2202. DOI: 10.1029/2001JB001569. URL: http://dx.doi.org/10.1029/2001JB001569.

Humphreys, E. D. and D. D. Coblentz (2007). "North American dynamics and western U.S. tectonics". In: *Reviews of Geophysics* 45.3, 2005RG000181. DOI: 10.1029/2005RG000181.

Jordan, T. H. (1975). "The continental tectosphere". In: *Reviews of Geophysics* 13.3, pp. 1–12. ISSN: 1944-9208. DOI: 10.1029/RG013i003p00001.

Kaban, Mikhail K., Irina Rogozhina, and Valeriy Trubitsyn (2007). "Importance of lateral viscosity variations in the whole mantle for modelling of the dynamic geoid and surface velocities". In: *Journal of Geodynamics* 43.2. Potential Fields in Geostatics and Geodynamics, pp. 262 –273. ISSN: 0264-3707. DOI: 10.1016/j.jog.2006.09.020.

Kameyama, M., D. A. Yuen, and S. Karato (1999). "Thermal-mechanical effects of low-temperature plasticity (the Peierls mechanism) on the deformation of a viscoelastic shear zone". In: *Earth Planet. Sci. Lett.* Pp. 159–172.

Karato, S. (2010). "Rheology of the deep upper mantle and its implications for the preservation of the continental roots: A review". In: *Tectonophysics* 481, pp. 82–98.

Karato, S. and P. Wu (1993). "Rheology of the upper mantle : a synthesis". In: *Science* 260, pp. 771–778.

Kaus, B. J. P., C. Steedman, and T. W. Becker (2008). "From passive continental margin to mountain belt: insights from analytical and numerical models and application to Taiwan". In: *Phys. Earth Planet. Inter.* 171, pp. 235–251.

Kawakatsu, H., P. Kumar, Y. Takei, M. Shinohara, T. Kanazawa, E. Araki, and K. Suyehiro (2009). "Seismic Evidence for Sharp Lithosphere-Asthenosphere Boundaries of Oceanic Plates". In: *Science* 324, pp. 499–502.

King, S. D. (2005). "Archean cratons and mantle dynamics". In: *Earth Planet. Sci. Lett.* 234, pp. 1–14. DOI: 10.1016/j.epsl.2005.03.007.

King, S. D. and J. Ritsema (2000). "African Hot Spot Volcanism: Small-Scale Convection in the Upper Mantle Beneath Cratons". In: *Science* 209, pp. 1137–1140. DOI: 10.1126/science.290.5494.1137.

Kreemer, C., J. Haines, W. E. Holt, G. Blewitt, and D. Lavallee (2000). "On the determination of a global strain rate model". In: *Earth, Planets and Space* 52.10, pp. 765–770. ISSN: 1880-5981. DOI: 10.1186/BF03352279.

Kreemer, C., W. E. Holt, and A. J. Haines (2003). "An integrated global model of present-day plate motions and plate boundary deformation". In: *Geophys. J. Int.* 154, pp. 5–34.

Lamb, Simon and Paul Davis (2003). "Cenozoic climate change as a possible cause for the rise of the Andes". In: *Nature* 425, pp. 792–797. DOI: 10.1038/nature02049.

Laske, G., G. Masters., Z. Ma, and M. Pasyanos (2013). "Update on CRUST1.0 - A 1-degree Global Model of Earth's Crust". In: *Geophys. Res. Abstr.* 15. Abstract EGU2013-2658.

Lithgow-Bertelloni, C. and J. H. Guynn (2004). "Origin of the lithospheric stress field". In: *J. Geophys. Res.* 109. DOI: 10.1029/2003JB002467.

Lithgow-Bertelloni, C. and M. A. Richards (1995). "Cenozoic plate driving forces". In: *Geophys. Res. Lett.* 22, pp. 1317–1320.

— (1998). "The dynamics of Cenozoic and Mesozoic plate motions". In: *Rev. Geophys.* 36, pp. 27–78.

Lithgow-Bertelloni, C. and P. G. Silver (1998a). "Dynamic topography, plate driving forces and the African superswell". In: *Nature* 395, pp. 269–272.

— (1998b). "Dynamic topography, plate driving forces and the African superswell". In: *Nature* 395, pp. 269–272. DOI: 10.1038/26212.

Lowry, A. R., N. M. Ribe, and R. B. Smith (2000). "Dynamic elevation of the Cordillera, western United States". In: *J. Geophys. Res.* 105, pp. 23371–23390.

Marquart, G. and H. Schmeling (1989). "Topography and Geoid Undulations Caused By Small-Scale Convection Beneath Continental Lithosphere of Variable Elastic Thickness". In: *Geophysical Journal International* 97.3, pp. 511–527. DOI: 10.1111/j.1365-246X.1989.tb00520.x.

McKenzie, D. P. (1972). "Plate tectonics, in The nature of the solid earth". In: McGraw-Hill, New York. ed. E. C. Robertson, pp. 323–360.

Mégnin, C. and B. Romanowicz (2000). "The three-dimensional shear velocity structure of the mantle from the inversion of body, surface, and higher-mode waveforms". In: *Geophys. J. Int.* 143, pp. 709–728.

Michael, P. (1995). "Regionally distinctive sources of depleted MORB: Evidence from trace elements and H_2O". In: *Earth and Planetary Science Letters* 131.3,

pp. 301–320. ISSN: 0012-821X. DOI: http://dx.doi.org/10.1016/0012-821X(95)00023-6.

Minster, J. B., T. H. Jordan, P. Molnar, and E. Haines (1974). "Numerical Modelling of Instantaneous Plate Tectonics". In: *Geophys. J. R. Astr. Soc.* 36.3, pp. 541–576. ISSN: 1365-246X. DOI: 10.1111/j.1365-246X.1974.tb00613.x. URL: http://dx.doi.org/10.1111/j.1365-246X.1974.tb00613.x.

Mitrovica, Jerry X. (1996). "Haskell [1935] revisited". In: *Journal of Geophysical Research: Solid Earth* 101.B1, pp. 555–569. ISSN: 2156-2202. DOI: 10.1029/95JB03208.

Mitrovica, Jerry X. and Alessandro M. Forte (1997). "Radial profile of mantle viscosity: Results from the joint inversion of convection and postglacial rebound observables". In: *Journal of Geophysical Research: Solid Earth* 102.B2, pp. 2751–2769. ISSN: 2156-2202. DOI: 10.1029/96JB03175.

Moresi, L., M. Gurnis, and S. Zhong (2000). "Plate tectonics and convection in the Earth's mantle: toward a numerical simulation". In: *Computing in Science and Engineering* 2 (3), pp. 22–33. DOI: 10.1109/5992.841793.

Moresi, L. N. and V. Solomatov (1998). "Mantle convection with a brittle lithosphere: thoughts on the global tectonic styles of the Earth and Venus". In: *Geophys. J. Int.* 133, pp. 669–682.

Müller, B., M. L. Zoback, K. Fuchs, L. Mastin, S. Gregersen, N. Pavoni, O. Stephansson, and C. Ljunggren (1992). "Regional patterns of tectonic stress in Europe". In: *Journal of Geophysical Research: Solid Earth* 97, pp. 11783–11803. DOI: 10.1029/91JB01096.

Müller, B., V. Wehrle, S. Hettel, B. Sperner, and K. Fuchs (2003). "A new method for smoothing orientated data and its application to stress data". In: *Geological Society, London, Special Publications* 209.Q04006, pp. 107–126. DOI: 10.1144/GSL.SP.2003.209.01.11.

Müller, R. D., M. Sdrolias, C. Gaina, and W. R. Roest (2008). "Age, spreading rates and spreading asymmetry of the world's ocean crust". In: *Geochem., Geophys., Geosys.* 9.Q04006. DOI: 10.1029/2007GC001743.

Naliboff, J.B., C. Lithgow-Bertelloni, L.J. Ruff, and N. de Koker (2012). "The effects of lithospheric thickness and density structure on Earth's stress field". In: *Geophysical Journal International* 188.1, pp. 1–17. DOI: 10.1111/j.1365-246X.2011.05248.x.

Nesbitt, H. W. and G. M. Young (1982). "Early Proterozoic climates and plate motions inferred from major element chemistry of lutites". In: *Nature* 299, pp. 715–717. DOI: 10.1038/299715a0.

Nicolas, Adolphe and N. I. Christensen (2013). "Formation of Anisotropy in Upper Mantle Peridotites - A Review". In: *Composition, Structure and Dynamics of the Lithosphere-Asthenosphere System*. American Geophysical Union, pp. 111–123. ISBN: 9781118670415. DOI: 10.1029/GD016p0111. URL: http://dx.doi.org/10.1029/GD016p0111.

O'Connell, R. J., C. W. Gable, and B. H. Hager (1991). "Toroidal-poloidal partitioning of lithospheric plate motions". In: *Glacial Isostasy, Sea-Level and Mantle Rheology*. Ed. by R. Sabadini and K. Lambeck. Norwell MA: Kluwer Academic Publishers, pp. 535–551.

Oleskevich, D. A., R. D. Hyndman, and K. Wang (1999). "The updip and downdip limits to great subduction earthquakes: Thermal and structural models of Cascadia, south Alaska, SW Japan, and Chile". In: *Journal of Geophysical Research: Solid Earth* 104.B7, pp. 14965–14991. ISSN: 2156–2202. DOI: 10.1029/1999JB900060.

Pekeris, C. L. (1935). "THERMAL CONVECTION IN THE INTERIOR OF THE EARTH". In: *Geophysical Journal International* 3, pp. 343–367. DOI: 10.1111/j.1365-246X.1935.tb01742.x.

Pollack, H. N., S. J. Hurter, and J. R. Johnson (1993). "Heat flow from the Earth's interior: Analysis of the global data set". In: *Reviews of Geophysics* 31.3, pp. 267–280. DOI: 10.1029/93RG01249.

Popov, A. and S. V. Sobolev (2008). "SLIM3D: A tool for three-dimensional thermomechanical modeling of lithospheric deformation with elasto-visco-plastic rheology". In: *Phys. Earth Planet. Inter.* 171, pp. 55–75. DOI: 10.1016/j.pepi.2008.03.007.

Quinteros, J. and S. V. Sobolev (2013). "Why has the Nazca plate slowed since the Neogene?" In: *Geology* 41, pp. 32–34.

Raymo, M. E. and W. F. Ruddiman (1992). "Tectonic forcing of late Cenozoic climate". In: *Nature* 359, pp. 117–122. DOI: 10.1038/299715a0.

Reynolds, Scott D., David D. Coblentz, and Richard R. Hillis (2002). "Tectonic forces controlling the regional intraplate stress field in continental Australia: Results from new finite element modeling". In: *Journal of Geophysical Research: Solid Earth* 107, pp. 2156–2202. DOI: 10.1029/2001JB000408.

Ricard, Y., C. Doglioni, and R. Sabadini (1991). "Differential Rotation Between Lithosphere and Mantle: A Consequence of Lateral Mantle Viscosity Variations". In: *J. Geophys. Res.* 96, pp. 8407–8415.

Richards, M. and B. H. Hager (1984). "Geoid anomalies in a dynamic Earth". In: *J. Geophys. Res.* 89, pp. 5987–6002.

Richards, M., W.-S. Yang, J. Baumgardner, and H.-P Bunge (2001). "Role of a low-viscosity zone in stabilizing plate tectonics: Implications for comparative terrestrial planetology". In: *Geochem., Geophys., Geosys.* 2, p. 1026. DOI: 10.1029/2000GC000115.

Richardson, R. M. (1992). "Ridge forces, absolute plate motions, and the intraplate stress field". In: *J. Geophys. Res.* 97, pp. 11739–11748.

Ritsema, J., A. Deuss, H. J. van Heijst, and J. H. Woodhouse (2011). "S40RTS: a degree-40 shear velocity model for the mantle from new Rayleigh wave dispersion, teleseismic traveltimes, and normal-mode splitting function measurements". In: *Geophys. J. Int.* 184, pp. 1223–1236.

Ritsema, Jeroen, Allen K. McNamara, and Abigail L. Bull (2007). "Tomographic filtering of geodynamic models: Implications for model interpretation and large-scale mantle structure". In: *Journal of Geophysical Research: Solid Earth* 112.B1. B01303, n/a–n/a. ISSN: 2156-2202. DOI: 10.1029/2006JB004566. URL: http://dx.doi.org/10.1029/2006JB004566.

Rogozhina, I. et al. (2016). "Melting at the base of the Greenland Ice Sheet explained by Iceland hotspot history". In: *Nature Geoscience* 9, pp. 366–369. DOI: 10.1038/ngeo2689.

Rychert, K. A., K. M. Fischer, and S. Rondenay (2005). "A sharp lithosphere-asthenosphere boundary imaged beneath eastern North America". In: *Nature* 436, pp. 542–545.

Schaeffer, A. and S. Lebedev (2013). "Global shear speed structure of the upper mantle and transition zone". In: *Geophys. J. Int.* 194, pp. 417–449.

Schellart, W. P. (2004). "Kinematics of subduction and subduction-induced flow in the upper mantle". In: *J. Geophys. Res.* 109. DOI: 10.1029/2004JB002970.

Schiffer, C. and S.B. Nielsen (2016). "Implications for anomalous mantle pressure and dynamic topography from lithospheric stress patterns in the North Atlantic Realm". In: *Journal of Geodynamics* 98, pp. 53–69. DOI: 10.1016/j.jog.2016.03.014.

Schwartz, S. Y. and J. M. Rokosky (2007). "Slow slip events and seismic tremor at circum-Pacific subduction zones". In: *Reviews of Geophysics* 45.3, RG3004. ISSN: 1944–9208. DOI: 10.1029/2006RG000208.

Sobolev, A. V. and M. Chaussidon (1996). "H_2O concentrations in primary melts from supra-subduction zones and mid-ocean ridges: Implications for H_2O storage and recycling in the mantle". In: *Earth and Planetary Science Letters* 137.1, pp. 45–55. ISSN: 0012-821X. DOI: 10.1016/0012-821X(95)00203-O.

Sobolev, S. V. and A. Y. Babeyko (2005). "What drives orogeny in the Andes?" In: *Geology* 33, pp. 617–620.

Sobolev, S. V., A. Popov, and B. Steinberger (2009). "Constraining rheology and water content in the upper mantle by modeling plate tectonics". In: *Geochimica et Cosmochimica Acta* 73.

Solomon, Sean C., Randall M. Richardson, and Eric A. Bergman (1980). "Tectonic stress: Models and magnitudes". In: *Journal of Geophysical Research: Solid Earth* 85.B11, pp. 6086–6092. DOI: 10.1029/JB085iB11p06086.

Stadler, G., M. Gurnis, C. Burstedde, L. C. Wilcox, L. Alisic, and O. Ghattas (2010). "The Dynamics of Plate Tectonics and Mantle Flow: From Local to Global Scales". In: *Science* 329, pp. 1033–1038.

Steinberger, B. (2000). "Slabs in the lower mantle – results of dynamic modelling compared with tomographic images and the geoid". In: *Phys. Earth Planet. Inter.* 118, pp. 241–257.

— (2016). "Topography caused by mantle density variations: observation-based estimates and models derived from tomography and lithosphere thickness". In: *GJI* 205, pp. 604–621.

Steinberger, B. and A. Calderwood (2006). "Models of large-scale viscous flow in the Earth's mantle with constraints from mineral physics and surface observations". In: *Geophys. J. Int.* 167, pp. 1461–1481.

Steinberger, B., H. Schmeling, and G. Marquart (2001). "Large-scale lithospheric stress field and topography induced by global mantle circulation". In: *Earth Planet. Sci. Lett.* 186, pp. 75–91.

Steinberger, B., R. Sutherland, and R. J. O'Connell (2004). "Prediction of Emperor-Hawaii seamount locations from a revised model of global plate motion and mantle flow". In: *Nature* 430, pp. 167–173.

Steinberger, Bernhard, Clinton P. Conrad, Anthony Osei Tutu, and Mark J. Hoggard (2017). "On the amplitude of dynamic topography at spherical harmonic degree two". In: *Tectonophysics*. ISSN: 0040-1951. DOI: https://doi.org/10.1016/j.tecto.2017.11.032. URL: http://www.sciencedirect.com/science/article/pii/S0040195117304948.

Stoddard, P. R. and D. Abbott (1996). "Influence of the tectosphere upon plate motion". In: *JGR* 101, pp. 5425–5433. DOI: 10.1029/95JB03540.

Tackley, P. J. (2000). "Self-consistent generation of tectonic plates in time-dependent, three-dimensional mantle convection simulations 1. Pseudoplastic yielding". In: *Geochem., Geophys., Geosys.* 1.2000GC000036.

Tan, Eh, Luc L. Lavier, Harm J. A. Van Avendonk, and Arnauld Heuret (2012). "The role of frictional strength on plate coupling at the subduction interface".

In: *Geochemistry, Geophysics, Geosystems* 13.10. Q10006, n/a–n/a. ISSN: 1525-2027. DOI: 10.1029/2012GC004214. URL: http://dx.doi.org/10.1029/2012GC004214.

Tesauro, M., M. K. Kaban, and S. A. P. L. Cloetingh (2012). "Global strength and elastic thickness of the lithosphere". In: *Global and Planetary Change* 91, pp. 51–57.

Thoraval, C. and M. A. Richards (1997). "The geoid constraint in global geodynamics: viscosity structure, mantle heterogeneity models and boundary conditions". In: *Geophys. J. Int.* 131, pp. 1–8. DOI: 10.1111/j.1365-246X.1997.tb00591.x.

Thoraval, C., A. Tommasi, and M. Doin (2006). "Plume-lithosphere interaction beneath a fast moving plate". In: *Geophysical Research Letters* 33.1, n/a–n/a. DOI: 10.1029/2005GL024047.

Torsvik, T. H., B. Steinberger, M. Gurnis, and C. Gaina (2010). "Plate tectonics and net lithosphere rotation over the past 150 My". In: *Earth Planet. Sci. Lett.* 291, pp. 106–112. DOI: 10.1016/j.epsl.2009.12.055.

Turcotte, D. L. and E. R. Oxburgh (1967). "Finite amplitude convective cells and continental drift". In: *J. Fluid Mech.* 28, pp. 29–42.

van Hinsbergen, D. J. J., P. Kapp, G. Dupont-Nivet, P Lippert, P. DeCelles, and T. Torsvik (2011). "Restoration of Cenozoic deformation in Asia, and the size of Greater India". In: *Tectonics* 30.TC5003. DOI: 10.1029/2011TC002908.

van Summeren, J., C. P. Conrad, and C. Lithgow-Bertelloni (2012). "The Importance of Slab Pull and a Global Asthenosphere to Plate Motions". In: *Geochem., Geophys., Geosys.* 13.Q0AK03. DOI: 10.1029/2011GC003873.

van Wijk, J. W., W. S. Baldridge, J. van Hunen, S. Goes, R. Aster, D.D. Coblentz, S. P. Grand, and J. Ni (2010). "Small-scale convection at the edge of the Colorado Plateau: Implications for topography, magmatism, and evolution of Proterozoic lithosphere". In: *Geology* 38, pp. 611–614.

Veevers, J. J. (1990). "Tectonic-climatic supercycle in the billion-year plate-tectonic eon: Permian Pangean icehouse alternates with Cretaceous dispersed-continents greenhouse". In: *Sedimentary Geology* 68, pp. 1–16.

Wang, S. and R. Wang (2001). "Current plate velocities relative to hotspots: implications for hotspot motion, mantle viscosity and global reference frame". In: *Earth Planet. Sci. Lett.* 189, pp. 133–140.

Wang, Xinguo, William E. Holt, and Attreyee Ghosh (2015). "Joint modeling of lithosphere and mantle dynamics: Evaluation of constraints from global tomography models". In: *Journal of Geophysical Research: Solid Earth* 120.12, pp. 8633–8655. DOI: 10.1002/2015JB012188.

Wen, L. and D. L. Anderson (1997). "Present-day plate motion constraint on mantle rheology and convection". In: *J. Geophys. Res.* 102, pp. 24639–24653.

Wheeler, P. and N. White (2000). "Present-day plate motion constraint on mantle rheology and convection". In: *J. Geophys. Res.* 28, pp. 963–966. DOI: 10.1130/0091-7613(2000)âĂŃ.

Wilks K. R. Carter, N. L. (1990). "Rheology of some continental lower crustal rocks". In: *Tectonophysics* 182, pp. 57–77.

Wu, B., C. P. Conrad, A. Heuret, C. Lithgow-Bertelloni, and S. Lallemand (2008). "Reconciling strong slab pull and weak plate bending: The plate motion constraint on the strength of mantle slabs". In: *Earth Planet. Sci. Lett.* 272, pp. 412–421.

Zhang, S. and U. Christensen (1993). "Some effects of lateral viscosity variations on geoid and surface velocities induced by density anomalies in the mantle". In: *Geophys. J. Int.* 114, pp. 531–547.

Zhong, S. (2001). "Role of ocean-continent contrast and continental keels on plate motion, net rotation of lithosphere, and the geoid". In: *J. Geophys. Res.* 106, pp. 703–712.

Zhong, S. and G. F. Davies (1999). "Effects of plate and slab viscosities on geoid". In: *Earth Planet. Sci. Lett.* 170, pp. 487–496.

Zhong, S. and M. Gurnis (1995). "Towards a realistic simulation of plate margins in mantle convection". In: *Geophys. Res. Lett.* 22, pp. 981–984.

— (1996). "Interaction of weak faults and non-Newtonian rheology produces plate tectonics in a 3D model of mantle flow". In: *Nature* 383, pp. 245–247.

Zhong, S. and A. B. Watts (2013). "Lithospheric deformation induced by loading of the Hawaiian Islands and its implications for mantle rheology". In: *Journal of Geophysical Research: Solid Earth* 118.11, pp. 6025–6048. ISSN: 2169-9356. DOI: 10.1002/2013JB010408.

Zhong, S., M. Gurnis, and L. Moresi (1998). "Role of faults, nonlinear rheology, and viscosity structure in generating plates from instantaneous mantle flow models". In: *J. Geophys. Res.* 103, pp. 15255–15268.

Zhong, S., M. T. Zuber, L. Moresi, and M. Gurnis (2000). "Role of temperature-dependent viscosity and surface plates in spherical shell models of mantle convection". In: *J. Geophys. Res.* 105, pp. 11063–11082.

Zoback, M. and W. Mooney (2003). "Lithospheric Buoyancy and Continental Intraplate Stresses". In: *International Geology Review* 45.2, pp. 95–118. DOI: 10.2747/0020-6814.45.2.95.

Zoback, M. L. (1992). "First- and second-order patterns of stress in the lithosphere: The World Stress Map project". In: *J. Geophys. Res.* 97, pp. 11703–11728.

Zoback, M. L.et, al, (1989). “Global patterns of tectonic stress”. In: *Nature* 341, pp. 291–298. DOI: 10.1038/341291a0.

Zoback, Mark D. et al. (1987). “New Evidence on the State of Stress of the San Andreas Fault System”. In: *Science* 238.4830, pp. 1105–1111. ISSN: 0036-8075. DOI: 10.1126/science.238.4830.1105. eprint: http://science.sciencemag.org/content/238/4830/1105.full.pdf.